Finite size scaling et force de Casimir critique : aimants d'Ising et fluides binaires

David Lopes Cardozo

N° National de Thèse : 2015ENSL1025

THÈSE

en vue de l'obtention du grade de

Docteur de l'Université de Lyon,
délivré par l'École Normale Supérieure de Lyon

Discipline : **Physique**

Laboratoire de Physique de l'ENS de Lyon

École Doctorale de Physique et d'Astrophysique de Lyon

Présentée et soutenue publiquement le 22 octobre 2015
par **M. David LOPES CARDOZO**

Finite size scaling and the critical Casimir force: Ising magnets and binary fluids

---

Directeur de Thèse: M. Peter HOLDSWORTH

Devant la commission d'examen formée de :

Monsieur	Denis BARTOLO	*ENS de Lyon*	Membre
Monsieur	Sergio CILIBERTO	*CNRS*	Membre
Monsieur	David DEAN	*Université de Bordeaux*	Rapporteur
Monsieur	Andrea GAMBASSI	*SISSA*	Rapporteur
Monsieur	Björgvin HJÖRVARSSON	*Uppsala Universitet*	Membre
Monsieur	Peter HOLDSWORTH	*ENS de Lyon*	Directeur

Laboratoire de Physique
École Normale Supérieure de Lyon
46, allée d'Italie
69007 Lyon

École doctorale de Physique et
Astrophysique de Lyon
4, Rue Enrico Fermi
69622 Villeurbanne Cedex

Remerciements

I would like to thank the members of the jury. It has truly been an honor to have such highly distinguished scientists focusing on my work for a time and to defend my thesis in front of them.

C'est un exercice assez étrange que celui des remerciements. Après trois années de travail, de recherche, d'enseignement, de rencontres, de collaborations et d'amitiés, ce qui restera est un long document scientifique, dans lequel une page a été insérée pour parler de toutes les relations humaines qui ont pourtant joué un rôle fondamental dans le succès de cette thèse.

Mes premières pensées vont à ma conjointe, Loren, et à ma famille, qui ont été là pour moi dans les moments difficiles et, surtout, avec qui j'ai pu partager des moments de joie et de réussite. Leur présence a énormément compté pour moi.

Mes amis, proches ou plus lointains, ne sont vraiment pas très loin derrière dans mes pensées tant il me semble parfois qu'ils constituent une seconde famille. Ensemble nous formons un grand système d'oscillateurs couplés dans lequel chaque moment de vie peut se propager, être amplifié, ou au contraire atténué. Au risque d'en décevoir certains, je ne chercherai pas à faire une liste exhaustive, mais c'est très simple : si vous vous dites que je pense à vous en écrivant ces lignes, alors c'est le cas.

Je remercie mon directeur de thèse, Peter Holdsworth, pour avoir su prendre toute la mesure de l'expérience humaine que représente une thèse, par l'optimisme dans les inévitables moments difficiles, par l'écoute et l'ouverture d'esprit qui ont immédiatement installé une relation de confiance et de franchise et par un sens de l'humour partagé, l'humour qui peut faire tant de choses.

Le Laboratoire de physique de l'ENS de Lyon ainsi que le Département de physique, où j'ai étudié et j'enseigne, sont des lieux où les relations humaines sont à juste titre valorisées. Je remercie donc (en vrac) les membres du Laboratoire de physique, chercheurs, ingénieurs, techniciens, secrétaires, les membres du projet ERC dirigé par Sergio Ciliberto, les chercheurs en post-doc, les doctorants, mes co-bureau et tous les membres du Département de physique, enseignants, techniciens, secrétaires, ainsi que les étudiants, qui font beaucoup pour la vie de l'ENS. Merci à tous ceux qui m'ont aidé, en espérant avoir aidé aussi, et à tous ceux qui ont essayé de faire de l'ENS de Lyon non seulement un lieu de savoir à part mais aussi un lieu humain.

Contents

Résumé - Abstract

Résumé dans la langue de Molière

À l'approche d'un point critique, la divergence de la longueur de corrélation des fluctuations peut être tronquée par le confinement du système. Cette troncature engendre des effets de taille finie présentant des caractères universels au sein d'un classe de transitions de phases.

Nous nous sommes intéressés particulièrement à la classe d'universalité du modèle d'Ising, regroupant notamment les transitions de phase ferro/paramagnétique pour les systèmes magnétiques uniaxiaux, la transition liquide/gaz et encore la démixtion de mélanges binaires. Nous présentons tout d'abord une introduction aux phénomènes critiques, à l'universalité, au "finite-size scaling" et aux simulations Monte Carlo du modèle d'Ising, sur lesquelles se fondent la majeur partie de ce travail.

Un effet de taille finie ayant attiré une grande attention durant les dernières dizaines d'années est la force de Casimir critique. Les travaux théoriques et numériques concernant cette force ont, dans leur quasi totalité, été menés dans des systèmes magnétiques modèles, tel que les modèles d'Ising ou XY. Par contre, les approches expérimentales ont toutes été réalisées dans des systèmes fluides, tels que des mélanges binaires ou de l'hélium IV proche de la transition superfluide.

Une motivation de ce travail a été de chercher a résoudre cette situation paradoxale en proposant, d'une part, un protocole expérimental pour la mesure de la force de Casimir dans une couche mince magnétique et, d'autre part, une approche numérique dans un mélange binaire de type Lennard-Jones. Cette dernière approche présente l'avantage d'ouvrir la porte à des études des fluctuations de la force de Casimir ou encore hors-équilibre.

Abstract in the language of Shakespeare

Approaching a critical point, the divergence of the correlation length of fluctuations can be cut-off by a confinement of the system. This truncation fosters finite size effects with universal features in a class of continuous phase transitions.

We are particularly interested in the Ising universality class, regrouping transitions such as the ferromagnetic/paramagnetic transition for uniaxial magnetic systems, the liquid/gas transition and the demixing of binary mixtures. We will first present an introduction to critical phenomena, universality, finite-size scaling and Monte Carlo simulations of the Ising model, on which a major part of this work relies.

A finite size effect that has particularly drawn attention in the past decades is the critical Casimir force. On the one hand, theoretical and numerical works on the subject have almost systematically been performed in magnetic model systems, such as the Ising or XY models. On the other hand, experimental approaches were all realized in fluid systems, such as binary mixtures or helium IV close to the superfluid transition.

A motivation of this work was to bridge this gap by proposing, firstly, an experimental protocol for measuring the critical Casimir force in a magnetic layer and, secondly, a numerical approach in a Lennard-Jones binary mixture. The latter is of particular interest as it could lead the way to studying fluctuations of the Casimir force or out-of-equilibrium phenomena.

Introduction and Outline

A phase transition is characterized by a singular behavior. The most commonly known singularities are discontinuities in extensive first derivatives of the free energy. In the case of a first order liquid/gas transition, the volume or the number of particles, thus the density, is discontinuous. In a binary fluid the composition changes discontinuously and in a ferromagnet under a magnetic field, the magnetic moment displays hysteresis due to a discontinuity in its equilibrium values. At continuous phase transitions, the singularity lies in second derivatives of the free energy. For example, the specific heat diverges at the critical point of the liquid/gas phase transition, demixing of binary mixtures or uniaxial ferromagnets. Moreover, the correlation length of fluctuations diverges at criticality, one spectacular and famous consequence of this divergence being the phenomenon of critical opalescence in a fluid. The critical singularities are characterized by scaling behavior: the evolution of thermodynamic quantities are dominated by power laws which can be summed up in scaling forms in which an n variable thermodynamic function condenses into an $n-1$ dimensional function of scaled variables. A fascinating feature stemming from scaling behavior is universality: a universality class is an ensemble of systems, experimental or model, sharing the exact same universal quantities at criticality, such as critical exponents. A universality class is characterized by the spatial dimension of the system, the short or long range character of the interaction and the symmetry of the order parameter. The three above examples, liquid/gas, uniaxial ferromagnets and demixing of binary mixtures, belong to the universality class of the Ising model. **In the first chapter** of this work, we will introduce some basic knowledge on phase transitions and the very special case of continuous phase transitions. The most prominent result being that it is possible to extract quantities that are relevant for critical phenomena in a wide range of experimental systems, from uniaxial magnets to polymer mixtures, from calculations in the rather simple Ising model.

In the absence of an exact solution of the Ising model in three dimensions, numerical simulations have been a major, ubiquitous and flexible tool for studying the Ising phase transition. **The second chapter**, is therefore dedicated to presenting Monte Carlo numerical simulations of the Ising model, that formed the basis of most of the present work. At the same time, this will give us the opportunity to introduce finite size scaling, a theoretical approach fundamental to the present work, both for numerical and experimental considerations. The scaling behavior we

describe in chapter 1 are observed in thermodynamically large systems. We have stated that a phase transition is characterized by a singular behavior, but in a finite system no phase transition can occur as only an infinite number of degrees of freedom can foster a singularity. For example, in a finite system, the divergence of the correlation length when approaching a critical point will eventually be cut off as it cannot outgrow the system size. This was first considered as a limitation for numerical simulations as the limitations of computer capacities and algorithms force one to perform simulations in systems with rather small number of degrees of freedom compared to experimental setups. At criticality, quantities computed in a finite system will depend on the size and boundary conditions of the simulation, with values far from their thermodynamic ones. Finite size scaling is an extension of the scaling hypothesis explicitly taking into account the new relevant thermodynamic parameter which is the confining size of the system. It is a powerful tool for the interpretation and exploitation of the thermodynamics of confined critical systems [1]. It takes advantage out of this size dependency and enables one to extract thermodynamic quantities, such as critical exponents [2] and universal scaling functions [3] from finite-size simulations.

Today, the interest in finite size scaling has moved beyond numerical simulations. Confined phase transitions have been experimentally explored in a great variety of systems [4]: polymer mixtures [5], superfluid helium [6–9], ferromagnets [10–12], etc. A fascinating finite size effect, which has been the topic of an abundant literature in past decades [13] is the critical Casimir force. The first "Casimir" force was predicted by Hendrik Casimir in 1948 [14] as a consequence of the confinement of quantum fluctuations of the electromagnetic field between two conducting and uncharged metallic plates in vacuum. Its critical counterpart has been predicted by Fisher and de Gennes in 1978 [15]. The confinement of critical fluctuations, similarly to the electrodynamic case, results in the critical Casimir force. The force can be defined in a finite size scaling universal form and thus will have the same form in a wide variety of phase transitions, inside a universality class. As this force is a consequence of the confinement of critical fluctuations, we have found it insightful to study how fluctuations develop in a confined system. We have computed the probability distribution of the magnetization at the critical point of the Ising model and used finite size scaling to study the influence of geometry and boundary fields on the form of this distributions. This will be the topic of the **third chapter**. The reader eager to know more about the critical Casimir force itself could pass this chapter and go directly to the following ones which tackle the most prominent part of this work: reinforcing the bonds between studies of the Casimir effect, both numeric and experimental, in magnetic and fluid systems.

The universality of the critical Casimir force allows one to compute its universal scaling function in model systems such as the Ising and XY models, numerical results in these model proving in very good agreement with experimental measurement in fluid systems [3]. **In the fourth chapter**, we will give an introduction to the critical Casimir force, its scaling form and experimental and numerical approaches. In particular, we will describe a very successful method for computing the critical Casimir force in the Ising model [3], which inspired many

elements of the numerical approaches we developed. We will try to emphasis one very important state of affairs which motived our work on the critical Casimir force: numerical and theoretical calculations of the critical Casimir force are systematically performed in magnetic model systems whereas measurements have all been done in fluid systems [5, 6, 13]. We have tried to close this gap by proposing new approaches to the computation of this force, which are the topics of **chapters five to seven**.

On the one hand, we have proposed the first experimental protocol for measuring the scaling function for the critical Casimir force in a magnetic thin film (*D. Lopes Cardozo, H. Jacquin and P. C. W. Holdsworth*, Phys. Rev. B, november 2014 [16]). We have tested this protocol through simulations of the Ising model, and this will be the topic of **the fifth chapter**. We believe this proposal could open the way to very rich experimental studies. Magnetic systems have long been the paradigm for studying critical phenomena (see for example ref. [17]) and the nano-engineering of magnetic thin films is particularly well-advanced [18]. Experimental systems [19] potentially cover a wide range of universality classes, including quantum phase transitions, and various surface conditions, opening the possibility for a rich variation in universal behavior.

On the other hand, we present preliminary results, obtained in collaboration with Francesco Puosi (post-doctoral researcher at ENS de Lyon) and Sergio Ciliberto (CNRS, ENS de Lyon), for the first direct measurement of the critical Casimir force through the simulation of a fluid system, using a symmetrical binary mixture of Lennard-Jones particles in the Semi-Grand Canonical ensemble. This will be the topic of **the seventh and final chapter**. We have made contact with previous results obtained in the Ising model through measurements of the universal scaling functions of the excess internal energy but also the excess generalized pressure $\tilde{P} = P - n\mu$, which we show to be the suitable quantity for a direct measurement of the critical Casimir force, P being the pressure, μ the total chemical potential and n the total density. We also obtained results that were not accessible directly to Ising model simulations. We have been able to distinguish the influence in the critical Casimir force of both the excess pressure and the excess chemical potential, and related the excess chemical potential to the excess internal energy. In particular, we predicted and confirmed numerically that the excess pressure is anisotropic in slab geometry, in which a confining length $L_\perp$ is clearly identified compared to the transverse size $L_\parallel \gg L_\perp$. We believe these preliminary results in Lennard-Jones simulations of binary mixtures open the way to a great variety of studies, closely related to experimental approaches, such as measurements of the fluctuations of the critical Casimir force [20, 21], dynamic effects when performing temperature quenches and out-of-equilibrium effects.

To compare results obtained both in the Ising and Lennard-Jones systems, which belong to the same universality class, we have estimated the scaling functions of the excess free energy and excess internal energy in the Ising model, which have attracted far less interest than the scaling function of the critical Casimir force. This is the topic of **chapter six**, in which we show that the relation between excess free energy and the critical Casimir force, can be used to our advantage to extract the first from the latter. This is of particular interest theoretically as the

knowledge of the scaling function of the excess free energy gives access to any scaling function for quantities stemming from it, but also experimentally as the scaling function of the pressure anisotropy in slab geometry is the sum of the scaling functions of the critical Casimir force and the excess free energy.

All our numerical efforts benefited from the numerical resources of the PSMN at the ENS de Lyon [22] and this work was financed by the ERC grant OUTEFLUCOP with principal investigator Sergio Ciliberto (CNRS, ENS de Lyon). This work was performed during three years at the *Laboratoire de Physique* of the ENS de Lyon, under the direction of Peter Holdsworth.

Chapter 1

Phase Transitions and Critical Phenomena

The most commonly known phases of matter are the the gas, the liquid and the solid. They quite obviously differ by their macroscopic behavior: a gas tends to occupy all the volume offered, a liquid flows and a solid keeps its shape. Within these phases, others can be defined: we can distinguish different kinds of crystalline solids, fluids can be mixtures with complex interactions, atomic or molecular constituents can bear internal degrees of freedom such as magnetic or electric moments which can themselves organize in various phases. Some other phases are more subtle to define, such as the superfluid or superconducting states of matter. In the end, the number of phases of matter increases with the number of degrees of freedom and seems innumerable.

However, when it comes to continuous phase transitions, the number of different transitions is greatly reduced thanks to the concept of universality classes. A system undergoing a continuous phase transition will display singular behavior that has been showed to have universal features such as critical exponents, which are exactly identical in subsets of transitions, called universality classes [17]. We focus on the universality class of the Ising model in 3 dimensions, which bears the name of the simplest model belonging to this class and contains continuous transitions as various as the liquid-gas, demixing of binary mixtures and, of course, uniaxial magnetic systems. We will try to justify the predominance of the Ising model in the present work, which is our paradigm, by introducing theoretical notions on critical phenomena and the concept of universality classes.

1.1 Continuous and first-order transitions

1.1.1 The liquid-gas phase transition

In figure 1.1 we present a sketch of the most common phase diagram separating the solid, liquid and gas states of matter. We focus on the evolution from a liquid to a gas and present

three isothermal paths through the phase diagram. The first (blue) one crosses the boundary separating the liquid domain from the gas domain in the Pressure-Temperature (P-T) diagram (Fig. 1.1**a**). This boundary has been represented as a continuous line because if one considers the corresponding path in the Pressure-Density diagram ($P - n$, where n=N/V is the number of particles N per volume V), the transition will manifest itself by a discontinuous jump from a liquid of high density n_{liq} to a gas of low density n_{gas} (Fig. 1.1**b**) at constant pressure P_0, fixed by the temperature T_0. If, at pressure and temperature (P_0, T_0), an external operator imposes that the overall density of the system takes a value n_{inter} intermediate to n_{liq} and n_{gas}, the system will separate in two coexisting liquid and gas phases, so that no uniform phase of density n_{inter} can exist under these conditions.

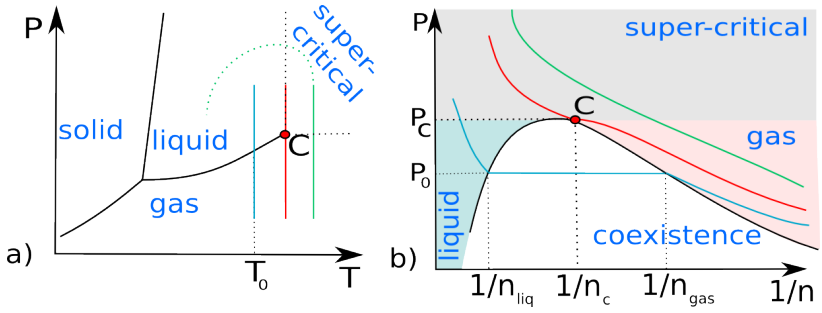

Figure 1.1: Three isothermal path (colored continuous lines) in a sketch of a liquid-gas phase diagram with respect to pressure and temperature **(a)** and pressure and molar volume **(b)** (the solid phase is not represented on the latter, and can be considered at the far left). The blue path represents a first order phase transition, the red one a continuous phase transition and the green one does not present any phase transition.

The two other isothermal paths (red and green) do not cross the separation line and no discontinuity in density occurs. This is made possible by the termination of the liquid-gas separation line at a critical point. The difference in density of the liquid and gas phases vanishes as the temperature is increased toward its critical value T_c. The "super-critical" region here is arbitrarily defined as the one in which $P > P_c$ and $T > T_c$. Starting from the gas phase and passing through the super-critical region along the green isotherm, one can bypass the critical point and continue the path towards the liquid phase by changing the temperature (dotted green line in Fig. 1.1a). It is thus possible to pass from a gas to a liquid phase without discontinuity in the density. This is made possible by the fact that both phases have the same microscopic symmetries, whereas a solid will always be separated by a phase boundary from a fluid. The discontinuity of a phase transition is associated with a change in symmetry, either in configuration, or in geometrical space. The liquid/gas phase transition divides configuration space in two, between high and low density configurations, while maintaining full translational symmetry in each sub space. A crystalline solid, however, has reduced translational symmetry compared with

the two fluid phases, which imposes that the crystalline solid will always be separated from the two fluid phases by a phase boundary [23].

Though they can seem equivalent in the present representation, the red ($T = T_c$) and green ($T > T_c$) isotherms differ most significantly. The red one is the critical isotherm at $T = T_c$, passing through the critical point. At this particular point, the system shows very surprising behavior. The first of them to be observed was the phenomena of critical opalescence, the fluid becoming turbid, scattering light of all wave lengths due to massive density fluctuations on all scales. This was later discovered to be accompanied by a divergence of the specific heat and isothermal compressibility. None of these singular features can occur along the green isotherm $T > T_c$, the particularity of the "super-critical" region being that no value of the thermodynamic variables (P, T, n) used in the diagrams of figure 1.1 give rise to any singularity.

These considerations lead to the classification of phase transitions, or more precisely of boundaries between phases, in two classes [23]:

- First-order phase transitions for which one or several extensive first derivatives of the free energy are discontinuous across the phase boundary. In our example, that is the case of the volume (or the number of particles, depending on the choice of variables kept fixed) which leads to a discontinuous density along the blue ($T < T_c$) isotherm of figure 1.1.
- Continuous phase transitions, for which a second derivative of the free energy is discontinuous or diverges. That is the case along the red path of figure 1.1.

In our formalism, a phase transition is not the passing from a phase to the other but the crossing of a phase boundary, that is to say of a point of non-analytic behavior for the free energy. Even if we allowed the temperature to drop so that the green path of figure 1.1 rejoined the liquid phase, no "phase transition" would be considered to occur as we need either to cross the line of first-order transitions or pass through the critical point to observe a non-analytic behavior.

The critical point gives a natural scale of pressure P_c, temperature T_c and density n_c. Using reduced units $(P/P_c, T/T_c, n/n_c)$, we see that all phase diagrams for the liquid/gas phase transitions of different fluid systems fall on one master curve, Fig. 1.2. This is referred to as the law of corresponding states and constitutes our first step in the concept of universality, showing the special importance of critical points. Here, universality is only a consequence of dimensional analysis, but later, we will develop a more subtle concept of universality, appearing at criticality: scaling behavior and universality classes.

1.1.2 Line of continuous phase transitions

In addition to the solid, liquid and gas phases, if the constituents of a system bear magnetic moments they can undergo magnetic phase transitions. For example, in figure 1.3, we sketch the phase diagram of a system which, in the solid phase, can either present a paramagnetic

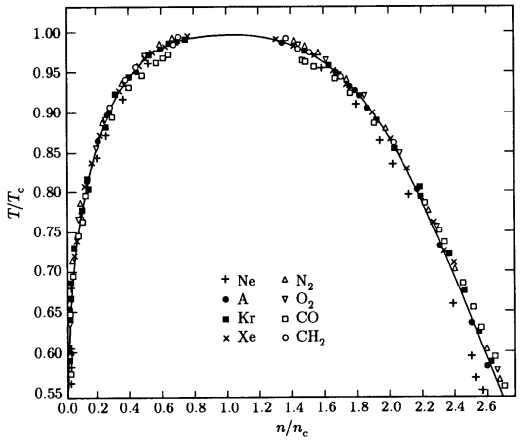

Figure 1.2: Experimental phase diagrams in reduced variables $(T/T_c, n/n_c)$ for several fluid systems: all fall on one master curve. Figure from ref. [24], proceeding from the work of ref [25].

or ferromagnetic behavior, the latter being characterized by a non zero macroscopic magnetic moment in the absence of magnetic field. The phase boundary of figure 1.3 is represented as a dashed line as it is a line of continuous phase transitions, to be distinguished from the solid lines, phase boundaries at which first order transitions occur.

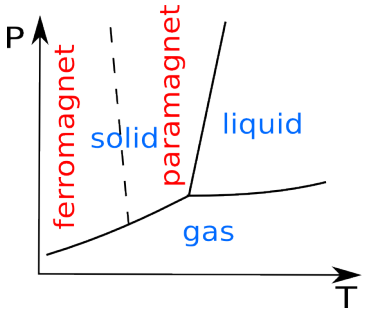

Figure 1.3: Phase diagram of a magnetic material in the absence of a magnetic field: in the solid phase two magnetic phases, ferro- and paramagnetic, are separated by a critical line.

We will not go any further into the classification of the great variety of possible phase diagrams [23, 24, 26] but from now on the ferromagnetic-paramagnetic phase transition will be our paradigm for describing phase transitions and for this purpose we will rely on the Ising model.

1.2 The Ising model

1.2.1 Definition of the model

The Ising model is at the heart of this work. It has first been introduced by Ising during his phD thesis, almost a century ago, to describe the ferromagnetic-paramagnetic transition. A magnetic system is described here as an ensemble of microscopic spins S_i organized on a lattice. In the present work, only the very simple, but already rich, case of classical spins $S_i = \pm 1$ on 2-dimensional square or 3-dimensional cubic lattice will be considered. The spins interact through a nearest neighbor exchange coupling characterized by a coupling constant J and are submitted to a magnetic field h. The Hamiltonian of the system reads

$$\mathscr{H} = -J \sum_{\langle i,j \rangle} S_i S_j - h \sum_i S_i \ , \tag{1.1}$$

where the sum $\sum_{\langle i,j \rangle}$ runs over all pairs of nearest neighbors and $\sum_i$ over all spins. Thermal agitation will tend to give random values to the spin and foster a paramagnetic phase with no magnetization at $h = 0$, whereas the nearest neighbor interactions favors alignment of spins and fosters a low temperature ferromagnetic phase with a non zero magnetization for all value of the magnetic field, including $h = 0$.

Despite its great simplicity, the Ising model accurately describes the magnetic phase transition of many uniaxial magnetic materials [19, 27, 28]. From a theoretical point of view, its importance goes way beyond the description of those ferromagnetic materials as it is the generic model for a system with a scalar order parameter. It is the simplest model of the universality class that bears its name, which also contains the liquid/gas and demixing of binary mixtures transitions, as we will develop in the following. The Ising model has been solved in 1-dimension by Ising himself, showing that there is no phase transition at a non-zero temperature in this case. The solution in 2-dimensions was found by Onsager in 1944 [29], proving the existence of a phase transition at a finite temperature $T_c = 2J/(k_B \log(1+\sqrt{2}))$. Mean-field approaches [24] already give insights on the nature of the phase transition and its critical behavior and give a quantitative description for dimension 4 and above, $d = 4$ being known as the upper critical dimension. Mean field approaches are still widely used today but an exact solution in 3-dimensions is still lacking. However, extensive theoretical and numerical works [30] have lead to a rather precise understanding of the critical behavior of the Ising model [4], which is still today at the heart of many works on critical phenomena.

In the same spirit as Fig.1.2, we present a sketch of the phase diagram of an Ising ferromagnet in figure 1.4. The thermodynamic variables considered are the temperature T, the external magnetic field h and the average magnetization per spin $\langle m \rangle$

$$\langle m \rangle = \frac{\langle M \rangle}{N} = \frac{1}{N} \langle \sum_i S_i \rangle \ , \tag{1.2}$$

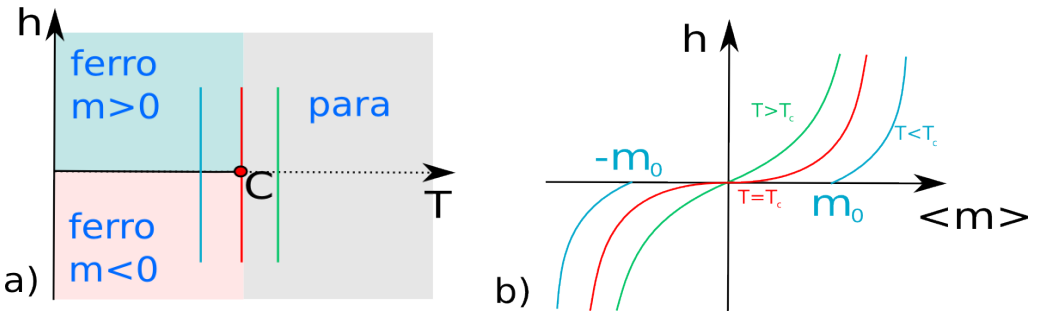

Figure 1.4: Sketch of phase diagrams in the (h, T) **(a)** and $(h, \langle m \rangle)$ **(b)** planes for a ferromagnetic system. Three isotherms are sketched, displaying a first order phase transition (blue, $T < T_c$), a continuous phase transition (red, $T = T_c$) and not transition at all (green, $T > T_c$). At temperatures above the critical value T_c the system is paramagnetic and has a zero average magnetization in the absence of a magnetic field. At low temperature $T < T_c$, the system is ferromagnetic and displays a non zero magnetization $\pm m_0$ at zero magnetic field.

with N the number of spins in the system and $\langle . \rangle$ stands for a statistical average. Three isotherms are sketched: one (blue) crossing the line of first order transitions (Fig.1.2a) across which the magnetization discontinuously changes from positive to negative values (Fig.1.2b), the critical isotherm (red) along which, at the critical point, the specific heat and magnetic susceptibility diverge, and a super-critical (green) isotherm which displays no phase transition, though the magnetization goes from negative to positive value, as for the other isotherms. As in the liquid-gas case, the critical point defines an energy scale $k_B T_c$, with k_B the Boltzmann constant, allowing one to define reduced units $(\tilde{h} = h/(k_B T_c), T/T_c)$ to obtain a unique description of all Ising magnets, regardless of the internal parameter J.

1.2.2 Ising model and lattice fluids

Let us make the following change of variables for the Ising model [23]:

$$n_i = \frac{S_i + 1}{2} \ , \tag{1.3}$$

so that $n_i(S_i = 1) = 1$ and $n_i(S_i = -1) = 0$. The Hamiltonian of the Ising model becomes

$$\mathscr{H} = -4J \sum_{\langle i,j \rangle} n_i n_j - (\mu - \mu_c) \sum_i n_i + (Jz - h)N \ , \tag{1.4}$$

where the constant term $(Jz - h)N$ is only an energy shift which will not change the equilibrium properties of the system, so we define

$$\mathscr{H}_{LG} = -4J \sum_{\langle i,j \rangle} n_i n_j - (\mu - \mu_c) \sum_i n_i \ , \tag{1.5}$$

where $\mu = 2h$ and $\mu_c = 4Jz$, describing a lattice gas with short range interactions. The transition from a positively magnetized Ising model to a negatively magnetized one is thus equivalent to going from a high density lattice fluid $\langle n_i \rangle > 1/2$ to a low density one $\langle n_i \rangle < 1/2$.

We can also convince ourselves that the Ising model could represent a mixture of two species A ($S_i = 1$) and B ($S_i = -1$). Like particles attract each other ($-JS_iS_j < 0$ if $S_i = S_j$) and unlike particles repel each other ($-JS_iS_j > 0$ if $S_i \neq S_j$). The field h is then a mismatch in chemical potentials $h \sim \mu_A - \mu_B$ favoring either A or B particles. A non zero magnetization corresponds to a rich in A or B phase and a zero magnetization to a mixed phase. Temperature then drives a demixing phase transition for a symmetrical (as the roles of A and B are equivalent) binary fluid. Thus, the Ising model is not only a model for uniaxial magnetic systems but is also a lattice model for fluid systems.

We will often refer to the magnetization as the order parameter. An order parameter is a characteristic feature of a phase transition, for a continuous phase transition it reflects the spontaneous breaking of a symmetry in the system between phases above and below the critical temperature. In the magnetic system the spin reversal symmetry is broken in the equilibrium phases below T_c, for the lattice gas it is the particle-hole symmetry that is broken, and the $A-B$ exchange symmetry in the binary mixture. In the absence of conjugate field (magnetic field $h = 0$, deviation to the critical value of the chemical potential $\mu - \mu_c = 0$ or chemical mismatch $\mu_A = \mu_B$) this is reflected by the change from zero to non zero value of the order parameter, which in our examples is the magnetization $\langle m \rangle$, equivalently the deviation to the critical density $n - n_c$ or the fraction in A (equivalently B) particles $x_A - x_c$ compared to the mixed $x_c = 1/2$ case. For other phase transitions, the order parameter can be difficult to measure, for example in the case of the liquid-solid transition or the normal fluid/superfluid transition. Depending on the phase transition, the order parameter can have different symmetries, being a scalar in the cases of the present section, a vector as in the case of non-uniaxial magnetic systems or the superfluid transition, or even a tensorial order parameter as in the case of liquid crystals. As we will see further, this symmetry of the order parameter is an important feature in differentiating universality classes.

Even though there is an exact mapping between a lattice gas, a lattice binary mixture and the Ising model, the equivalence between a real gas, a real binary mixture and a real Ising magnet is not exact. The similarities between the three systems are still quite striking if one considers the general form of the phase diagrams as presented in figure 1.5. In the case of the demixing of binary mixtures we present here the case of a high temperature consolute (critical) point, which compares most easily with the ferromagnetic case. We mention that the mixed phase can also be a low temperature phase and the demixed region a high temperature one, so that low temperature consolute points are also possible, and even phase diagrams with two consolute points, both high and low temperature, are observed. Comparing these three different phase transitions seems to be only qualitative, the exact mapping being confined to lattice models of fluids, which clearly can only be sketches of real fluids. We will see that close to the critical

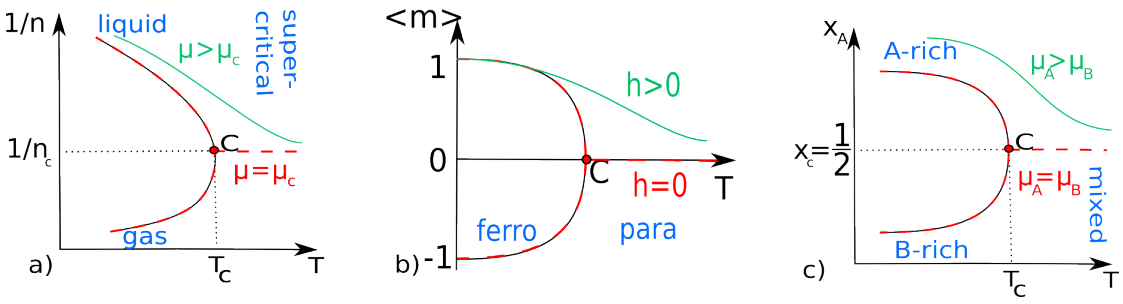

Figure 1.5: Sketches of three phase diagrams for the liquid-gas **(a)**, ferro-paramagnetic **(b)** and demixing of a symmetrical binary mixture **(c)** phase transitions, displayed together in order to emphasize their similarity. The reader can see ref. [26] for related discussions.

point, this analogy takes a very deep meaning with quantitative consequences: some quantities are universal for all these systems, allowing one to extract relevant quantities for all of them from the sole study of the Ising model. To this purpose, we need to introduce some quantitative aspects on the theory of continuous phase transitions and scaling at criticality.

1.3 Continuous phase transitions and scaling laws

1.3.1 Free energy and observables

We will first recall some fundamental notions of statistical mechanics. Taking a general approach, we consider a physical system whose macroscopic behavior is controlled by a set of microscopic degrees of freedom φ_i, for example, spins for a magnetic system or positions of particles in a fluid one. The probability of observing a particular realization for the ensemble of the N degrees of freedom $\varphi = (\varphi_1, \ldots, \varphi_N)$, or microstate, is given by the Boltzmann weight

$$P[\varphi] \equiv \frac{1}{Z} e^{-\varkappa \mathscr{H}[\varphi]} \ , \tag{1.6}$$

where $\varkappa$ is the inverse thermal energy $\varkappa = 1/(k_B T)$, $\mathscr{H}$ the Hamiltonian of the system and Z a normalization factor, the partition function

$$Z \equiv \sum_{\{\varphi\}} e^{-\varkappa \mathscr{H}[\varphi]} \ , \tag{1.7}$$

where $\{\varphi\}$ denotes the ensemble of all possible microstates (for a classical system of particles, it is the integral over all positions and speeds of all particles). In principle, the partition function allows for the calculation of the thermodynamic properties of all phases of the considered body. The statistical average of an observable $\mathcal{O}$, of value $\mathcal{O}[\varphi]$ in a micro state φ, is given by

$$\langle \mathcal{O} \rangle \equiv \sum_{\{\varphi\}} \mathcal{O}[\varphi] \ P[\varphi] \ . \tag{1.8}$$

We define the free energy as:

$$\Omega = -k_B T \ln Z \ . \tag{1.9}$$

In this work, we focus on the Ising model universality class and thus we will use the formalism of magnetic systems. The free energy then depends on temperature T, magnetic field h and volume V of the system. We define magnetic observables such as the magnetic moment

$$\langle M \rangle = \langle \sum_i S_i \rangle = \left. \frac{\partial \Omega}{\partial h} \right|_T \ , \tag{1.10}$$

the order parameter

$$\langle m \rangle = \frac{\langle M \rangle}{N} \ , \tag{1.11}$$

and the associated susceptibility per spin

$$\chi_N \equiv \frac{\chi}{N} \equiv \frac{1}{N} \left. \frac{\partial \langle M \rangle}{\partial h} \right|_T = \frac{1}{N} \left. \frac{\partial^2 \Omega}{\partial h^2} \right|_T = \frac{\varkappa}{N} \left(\langle M^2 \rangle - \langle M \rangle^2 \right) \ . \tag{1.12}$$

Nevertheless, we stress on the fact that these are very general quantities with equivalent counterparts in fluids, as we have already mentionned in the previous section. For example, the order parameter for a liquid-gas phase transition is built from the density, which we define in the Grand-Canonical ensemble (T, V, μ) in a similar way to the magnetization per spin

$$n = \frac{\langle N \rangle}{V} = -\frac{1}{V} \left. \frac{\partial \Omega}{\partial \mu} \right|_{T,V} \ , \tag{1.13}$$

and the corresponding "susceptibility" being [23]

$$n^2 \kappa_T = \frac{1}{V} \left. \frac{\partial \langle N \rangle}{\partial \mu} \right|_{T,V} = \frac{\varkappa}{V} \left(\langle N^2 \rangle - \langle N \rangle^2 \right) \ , \tag{1.14}$$

with κ_T the isothermal compressibility, more naturally defined in the isothermal-isobar (N, P, T) ensemble

$$\kappa_T = -\frac{1}{V} \left. \frac{\partial V}{\partial P} \right|_{N,T} \ . \tag{1.15}$$

To conclude these very general notions of statistical mechanics, we stress on the fact that if one divides a system of very large volume in two subsystems, when the volume is sent to infinity, the surface contribution between the two subsystems will become negligible with respect to the overall free energy, as well as contributions coming from the outer limits of the system. In this case, the free energy becomes extensive and is thus proportional to the volume of the system:

$$\Omega(T, h, V) \underset{V \to \infty}{\sim} V k_B T \omega_{bulk}(T, h) \ , \tag{1.16}$$

where ω_{bulk} is the free energy per unit volume expressed in units of $k_B T$, that we will refer to as the thermodynamic limit or bulk free energy.

1.3.2 Critical exponents and scaling relations

We have seen that the order parameter vanishes at a continuous phase transition. Experimentally, it is observed that this behavior is controlled by a power law

$$\langle m(T, h = 0)\rangle \underset{T\to T_c^-}{=} m_0|t|^\beta \ , \tag{1.17}$$

at zero magnetic field, defining the order-parameter exponent β and a dimensionless reduced temperature

$$t \equiv \frac{T - T_c}{T_c} \ . \tag{1.18}$$

Scaling behavior for observables are characteristic of the singular behavior of systems undergoing continuous phase transitions. The susceptibility per spin diverges at the transition:

$$\chi_N(T) \underset{T\to T_c}{=} \chi_0^\pm |t|^{-\gamma} \ , \tag{1.19}$$

as well as the specific heat at constant volume and constant magnetic field

$$C_v(T) = \left.\frac{\partial \langle \mathscr{H}\rangle}{\partial T}\right|_{V,h} = -T \left.\frac{\partial^2 \Omega}{\partial T^2}\right|_{V,h} \underset{T\to T_c}{=} C_0^\pm |t|^{-\alpha} \ , \tag{1.20}$$

defining the exponents γ, α and the scaling amplitude $C_0^\pm, \chi_0^\pm$, taking $+$ value when approaching the critical point from above and $-$ from below.

At criticality, the fluctuations of the order parameter become macroscopic (we mentioned the phenomenon of critical opalescence as a consequence of the fluctuations of density in a critical fluid). The fluctuations are correlated on a typical length ξ which can be defined using the order parameter correlation function [24, 30]

$$G(i, j, T, h) = \langle (S_i - \langle m\rangle)\,(S_j - \langle m\rangle)\rangle \ , \tag{1.21}$$

which, for temperatures far above the critical value, takes the Ornstein-Zernike form [31, 32]

$$G(r) \underset{r\to\infty}{\propto} r^{-(d-1)/2} e^{-r/\xi} \ . \tag{1.22}$$

At the critical point, ξ diverges as

$$\xi(T, h = 0) \underset{T\to T_c}{=} \xi_0^\pm |t|^{-\nu} \ , \tag{1.23}$$

which defines the correlation length exponent ν and it is observed at the critical temperature that [31, 32]

$$G(r; T_c, h = 0) \underset{r\to\infty}{\sim} r^{-(d-2+\eta)} \ , \tag{1.24}$$

where d is the dimension of the space and η a new critical exponent. Instead of working at $h = 0$, one can work precisely at $T = T_c$ with a non-zero homogeneous magnetic field h. In that case, scaling behavior occur with respect to the field, such as

$$\langle m(T_c, h)\rangle \underset{h\to 0}{=} m_{0,h}^\pm |h|^{1/\delta} \ . \tag{1.25}$$

Two of the scaling exponents are independent, as many as the two relevant thermodynamic variables t and h. All other exponents can then be deduced using scaling relations which relate all exponents one to each other. We list scaling relations here, along with their usual names

$$\begin{aligned} \text{Fisher} \quad & \gamma = \nu(2-\eta) \ , \\ \text{Rushbrooke} \quad & \alpha + 2\beta + \gamma = 2 \ , \\ \text{Josephson} \quad & \nu d = 2 - \alpha \ , \\ \text{Widom} \quad & \gamma = \beta(\delta - 1) \ . \end{aligned} \tag{1.26}$$

The Josephson hyperscaling relation, which introduces the spatial dimension into the relations, is not always valid and breaks down above the upper critical dimension d_c at which mean-field becomes relevant ($d_c = 4$ for the Ising model).

1.3.3 Scaling hypothesis

We separate the free energy by unit volume in an analytic ω_a and a leading non analytic part ω_s^0

$$\omega_{bulk} = \omega_a(T,h) + \omega_s^0(t,\tilde{h}) \ , \tag{1.27}$$

The magnetization, susceptibility and specific heat stem from the free energy and thus their singular behavior should be contained in its singular part. The scaling hypothesis, first proposed by Widom on a phenomenological basis, is to consider that all scaling behaviors and scaling relations can be summed up by defining scaling functions, such as $\mathscr{F}_\pm, \mathscr{G}$ for the singular part of the free energy and for the correlation function [23, 24]

$$\begin{aligned} \omega_s^0(t,h) &= |t|^{2-\alpha} \mathscr{F}_\pm \left(\frac{h}{t^\Delta} \right) \ , \\ G(r;T,h) &= r^{-(d-2+\eta)} \mathscr{G} \left(\frac{r}{\xi}, \frac{h}{t^\Delta} \right) \ , \end{aligned} \tag{1.28}$$

defining the gap exponent Δ. The scaling hypothesis thus predicts that an n variable thermodynamic function condenses into an $n-1$ dimensional function of scaled variables. The dominant singular contribution to the observable, giving their scaling behavior, can be derived from Eq.1.28, for example

$$\begin{aligned} \langle m(T,h=0) \rangle &\sim \left. \frac{\partial \omega_s^0}{\partial h} \right|_T (T,h=0) = |t|^{2-\alpha-\Delta} \mathscr{F}'_\pm(0) \propto |t|^\beta \ , \\ \chi(T,h=0) &\sim \left. \frac{\partial^2 \omega_s^0}{\partial^2 h} \right|_T (T,h=0) = |t|^{2-\alpha-2\Delta} \mathscr{F}''_\pm(0) \propto |t|^{-\gamma} \ , \end{aligned} \tag{1.29}$$

relating Δ with the exponents we defined perviously $\beta = 2-\alpha-\Delta$ and $-\gamma = 2-\alpha-2\Delta$, leading to the Rushbrooke equality $\alpha + 2\beta + \gamma = 2$. In the same way, the power law behavior and scaling relations we have defined in the previous section can be deduced from Eq.1.28 (see ref. [24]),

except for the Josephson relation. The derivation of the Josephson (or hyperscaling) relation is more controversial. The simplest way to see it is to say that, at very large scales and finite correlation length, the free energy is expected to be the sum of the free energy of all sub-volumes of size V/ξ^d, extensivity, lost due to the macroscopic correlation length, being recovered for scales above the correlation length. Thus we would expect with this argument that:

$$\Omega(T, h = 0) \underset{t\to 0}{\sim} \frac{V}{\xi^d} \propto V|t|^{\nu d} , \tag{1.30}$$

which, combined with Eq.1.28 gives the Josephson relation of Eq.1.26.

The scaling hypothesis can be experimentally tested. For example, the magnetization scaling form $\langle m(T, h)\rangle = |t|^{\beta}\mathscr{F}'_{\pm}(h/t^{\Delta})$ shows that an experimental test of the scaling hypothesis is to verify that $\frac{m}{t^{\beta}}$ is indeed a function of $\frac{h}{t^{\Delta}}$, whatever the couple (T, h) at which the magnetization is measured. This has been verified in many systems and we present in figure 1.6 an example of experimental realization in EuO [33].

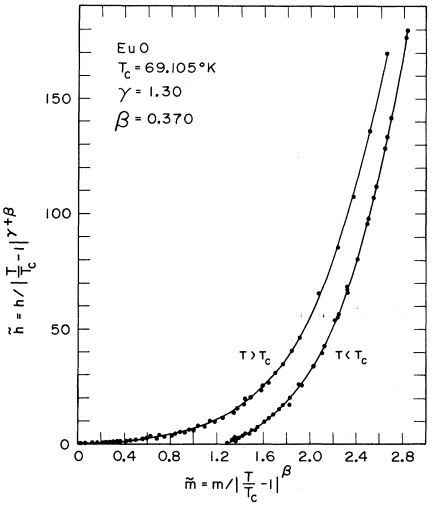

Figure 1.6: Magnetic equation of state in EuO, a classical Heisenberg ferromagnet. This is an experimental verification of the scaling hypothesis in a magnetic system: whatever the couple (t, h) at which the magnetization was measured, all points fall on a master curve if one plots $\frac{m}{t^{\beta}}$ as a function of $\frac{h}{t^{\Delta}}$. Figure from ref [33] (see also ref. [24]).

1.3.4 Origin of the scaling hypothesis

The divergence of the correlation length at the critical point means that fluctuations can exist on all length scales, from the microscopic to the macroscopic. Consequently, the fluctuations will be the same on all length scales and the organization of the order parameter will be self similar (except of course, if we look at length scales of the order of the microscopic distance separating

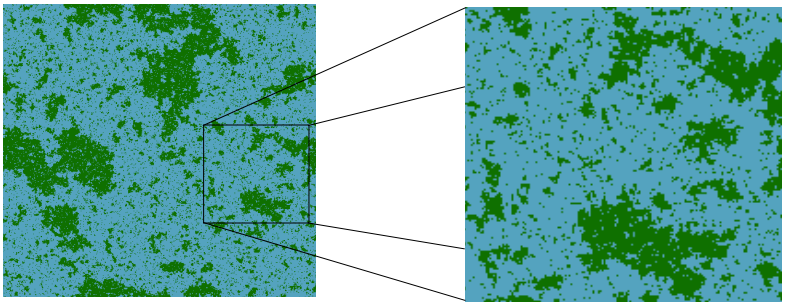

Figure 1.7: Snapshot of an Ising 2D system close to its critical point obtained by Monte-Carlo simulation. Blue and green points represent spins pointing up and down. Zooming on a random region of the configuration, we emphasize its self similarity.

the components of the system). This self similarity can be seen by zooming in or out of snapshots of our system: in figure 1.7, we display a snapshot of the Ising model in 2 dimensions close to its critical point, obtained by Monte Carlo simulations, and show that a zoom on a random region of the system looks very much like the total system itself. A consequence of this self similarity, first proposed by Kadanoff, whose ideas led to the formalism of the renormalization group introduced by Wilson, is that, approaching the critical point, any thermodynamic function obeys a homogeneity relation in which t and h are rescaled [24]. In the case of the singular part of the free energy this reads

$$\omega_s^0(t,h) = \ell^{-d} f^{\pm}(\ell^{y_t} t, \ell^{y_h} h) \ , \tag{1.31}$$

with a different function f above $(+)$ and below T_c $(-)$. This leads to the scaling hypothesis function when choosing $\ell = t^{-1/y_t}$ and $y_t = 1/\nu, y_h = \Delta/\nu$

$$\omega_s^0(T,h) = |t|^{\nu d} f^{\pm}\left(1, t^{-\Delta} h\right) = |t|^{2-\alpha} \mathscr{F}_{\pm}\left(\frac{h}{t^{\Delta}}\right) \ . \tag{1.32}$$

The same arguments, in a more general framework allowing for non uniform magnetic fields, leads to the scaling form of the correlation function [23].

1.3.5 Universality classes

Critical exponents and certain amplitude combinations such as the ratio ξ_0^+/ξ_0^- are universal. They take the same value in a variety of systems which form a universality class (for a review on critical phenomena, see ref. [4]). Actually, scaling functions such as $\mathscr{F}_{\pm}$, and thus $\mathscr{F}'_{\pm}$, are themselves universal, to within non universal amplitudes affecting the amplitude of the function and the scaling variable [34], so that

$$\mathscr{F}_{\pm}(\frac{h}{t^{\Delta}}) = A_1 W_{\pm}(A_2 \frac{h}{t^{\Delta}}) \ , \tag{1.33}$$

defines a fully universal function $W_{\pm}$, A_1 and A_2 being non universal factors.

A universality class is characterized by the spatial dimension of the system, the short or long range character of the interaction and the symmetry of the order parameter. By short range of interactions concerning critical phenomena, which is the case we are interested in, one means that the typical interaction potential in a system decays faster than $r^{-(d+2)}$ for $r \to \infty$, with r the separation between components of the system [26]. This is a stronger assumption than requiring the existence of a stable equilibrium which imposes the potential to decay at least as fast as $r^{-(d+1)}$. The origin of universality can be formalized in the framework of renormalization group theory [23], which gives a theoretical background to scaling behavior and allows for the calculation of critical exponents and amplitudes. The universality class of the Ising model, bearing the name of its simplest member, regroups uniaxial ferromagnets, the liquid/gas phase transition and demixing of binary mixtures, involving the breaking of a $\mathbb{Z}_2$ symmetry. As we announced at the beginning of this chapter, the analogies we presented between these three systems take a quantitative meaning at criticality. No formal equivalence exist between systems undergoing a continuous liquid/gas transition, demixing of binary mixtures and the Ising model, yet they belong to the same universality class and their singular critical behaviors are described by the same universal quantities. We could add other experimental systems to the list of members of the Ising universality class, as reviewed in ref. [4], but we will mainly be interested in the present work by uniaxial magnetic systems and liquid binary mixtures.

	mean field	2D Ising	3D Ising	3D XY
α	0	0	0.110(1)	-0.0146(8)
β	1/2	1/8	0.3265(3)	0.3485(2)
γ	1	7/4	1.2372(5)	1.3177(5)
δ	3	15	4.789(2)	4.780(2)
ν	1/2	1	0.6301(4)	0.67155(27)
η	0	1/4	0.0364(5)	0.0380(4)
$\frac{2-\alpha}{\nu d}$	4/d	1	1	1
ξ_0^+; ξ_0^-		$1/\sqrt{2}$; $1/\sqrt{8}$	0.501(2); 0.243(1)	0.498(2) ; undefined
$\varkappa_c$		$\frac{1}{2}\log(1+\sqrt{2})$	0.2216544(3)	0.45420(2)

Table 1.1: Critical exponents of different bulk universality classes. Estimates for critical exponents in the Ising 3D universality class were taken from ref. [4] and for the 3D XY from ref. [35]. Correlation length amplitudes and critical temperatures were taken from ref. [3, 36, 37]. Zero exponents, such as $\alpha = 0$ in mean field and 2D Ising, signifies a logarithmic divergence.

Scaling is observed in mean-field solutions, such as the van der Waals model of fluids or the Bragg-Williams mean-field theory of ferromagnetism [24] and mean-field solutions form a universality class. Of course, as we know, mean-field is expected to break down if we get too close to a critical point and fluctuations become the predominant feature of the transition, but it is possible to observe a crossover between mean-field scaling behaviors and non-mean field behavior when approaching the critical point and some systems prove to be experimentally well described by mean-field behavior [38].

A universality class that we do not study in detail in this work but that we will mention often is the XY model universality class. The XY model is a model for magnetic systems of Hamiltonian

$$\mathscr{H}_{XY} = -J \sum_{\langle i,j \rangle} \vec{S_i}.\vec{S_j} - \sum_i \vec{h}.\vec{S_i} \ , \tag{1.34}$$

with two components spins $\vec{S_i} = (S_i^x, S_i^y)$ of unit-length $\|\vec{S_i}\| = 1$. The importance of this universality class to us is that it contains the normal fluid/superfluid continuous phase transition which led to spectacular agreement between theoretical and experimental works on the critical Casimir effect (see chapter 4).

In table 1.1, estimates of critical exponents and amplitudes of the correlation length for mean-field, 2D Ising, 3D Ising and 3D XY universality classes are reviewed. All scaling behavior is defined with positive exponents, so that specific heat, magnetic susceptibility and correlation length diverge at the critical point, except for the specific heat in the 3D XY universality class which displays a cusp form with $\alpha = -0.0146(8)$.

1.3.6 Corrections to scaling

The scaling hypothesis is only true asymptotically close to the critical point. Corrections to scaling are thus observed when approaching the critical behavior, which goes to zero when approaching close enough to $(T = T_c, h = 0)$. For example, the scaling function for the susceptibility [23]

$$\chi(T,h) = |t|^{-\gamma} \mathscr{F}''_{\pm}(\frac{h}{t^{\Delta}}, \tilde{K_3} t^{-\nu y_3}) \ , \tag{1.35}$$

can encompass an irrelevant scaling field $\tilde{K_3}$. The notion of scaling field comes from renormalization group theory and describes interaction in the system which are taken into account during renormalization. $\tilde{K_3}$ is called irrelevant as it is associated with an exponent $y_3 < 0$, so that $\tilde{K_3} t^{-\nu y_3} \underset{t \to 0}{\to} 0$, and we approach the scaling hypothesis of the form of Eq.1.28 close enough to T_c. For small value of t and at $h = 0$, Eq.1.35 can be developed with respect to the irrelevant field

$$\chi(T, h = 0) = |t|^{-\gamma}(A_{\pm} + B_{\pm} \tilde{K_3} t^{-\nu y_3} + \dots) \ , \tag{1.36}$$

with $A_{\pm}, B_{\pm}$ non-universal amplitudes, so that the power law $|t|^{-\gamma}$ is indeed the dominant behavior close to T_c but it might be necessary to take $t^{-\nu y_3}$ into account if one wants to extract critical exponents from measurements.

1.4 Conclusion

We have presented some standard aspects of the theory of critical phenomena and the concept of universality classes. Universality classes are of great importance for the theoretical and numerical study of critical phenomena: one can use the rather simple Ising model to compute universal quantities relevant not only to uniaxial ferromagnets but to fluid systems at the liquid/gas continuous transition and to the demixing of binary mixtures.

As we mentioned, an exact solution of the Ising model in 3-dimensions is still lacking but numerical simulations provide an ubiquitous and powerful approach for studying this system and has been for decades at the heart of many works on critical phenomena. However, numerical simulations require the study of rather small systems compared to experimental set-ups. In the present chapter we have developed critical phenomena at the thermodynamic limit, but we will see that scaling behavior can be studied in finite size systems and actually leads to new, experimentally relevant, phenomena.

Chapter 2

Simulation of Critical Phenomena and Finite Size Scaling

Numerical simulations provide an ubiquitous and powerful approach for studying the Ising model and haves been for decades at the heart of many works on critical phenomena. The limitations of computer capacities and algorithms force one to perform simulations in systems with, rapidly growing, but still rather small number of degrees of freedom compared to experimental setups. At criticality, quantities computed in a finite system will depend on the size and boundary conditions of the simulation, with values potentially very different from those in the thermodynamic limit. Finite-size scaling is a powerful tool for the interpretation and exploitation of the thermodynamics of confined critical systems [1] as it takes advantage of this size dependency and enables one to extract thermodynamic quantities, such as critical exponents [2] or universal scaling functions [3, 34]. In this chapter, we will present basic concepts of Monte Carlo simulation of the Ising model and show how the simulation of finite-size critical systems leads to the extension of the scaling hypothesis developed previously into the concept of finite-size scaling.

2.1 Monte Carlo simulations of the Ising model

2.1.1 The Metropolis and Wolff algorithms

The principle of Monte Carlo simulations is to numerically estimate observables by exploring the phase space of a system, that is to say, in the case of the Ising model, exploring spin configurations. Of course, exploring exactly the entire phase space, and thus exactly computing the partition function of a system

$$Z(T,h) = \sum_{\{S_i\}} e^{-\varkappa \mathscr{H}(\{S_i\})} \ , \tag{2.1}$$

where $\varkappa = 1/(k_B T)$ and $\sum_{\{S_i\}}$ means a sum over all configurations of spins, would provide an exact solution to our problem but can only be performed in very small systems in a reasonable amount of time. Thus, one must estimate the average values of observables on a subset of randomly generated configurations, this being the basis of Monte Carlo simulations (the name "Monte Carlo" being a reference to the games of chance of Monaco's Casinos). As it is clear from the form of the partition function, a configuration has an impact on the thermodynamics of the systems associated with the Boltzmann weight $e^{-\varkappa \mathscr{H}(\{S_i\})}$ and some configurations will have a much greater importance than others. To efficiently explore the phase space, on must take this weight into account when sampling configurations, this being referred to as the concept of importance sampling. We will not enter into technical demonstrations but a simple, yet efficient, importance sampling method is the Metropolis algorithm, which is widely used in a great variety of numerical simulations [2, 39]. In the Ising model, the basic rule for the algorithm is simple: a configuration of the spin system is updated by choosing at random a spin S_i, which will be flipped with a probability related to the change in energy associated with the flipping

$$\Delta E(S_i \to -S_i) = 2S_i \left(J \sum_{j \in nn(i)} S_j + h \right) , \tag{2.2}$$

where $nn(i)$ represents the list of nearest neighbors of the i^{th} spin. This probability reads

$$p_{metro}(S_i) = \min \left(1, e^{-\varkappa \Delta E(S_i \to -S_i)} \right) , \tag{2.3}$$

being 1 if flipping the spin is energetically favorable ($\Delta E(S_i \to -S_i) < 0$) and $e^{-\varkappa \Delta E(S_i \to -S_i)}$ which ranges from 0 to 1 otherwise. A Monte Carlo step is defined, in a system composed of N spins, by selecting N times a random spin and flipping it with probability p_{metro}. This ensures that, in principle, the system can be updated from any possible configuration to any other in one step. The algorithm generates an ergodic random walk through configuration space. This random walk satisfies detailed balance, that is to say the constraint that the probability $P(\mu \to \nu)$ for going from a state μ to a state ν is related to the probability of taking the reverse path by

$$\frac{P(\mu \to \nu)}{P(\nu \to \mu)} = e^{-\varkappa (E_\nu - E_\mu)} , \tag{2.4}$$

with $E_\nu - E_\mu$ the difference in energy between states μ and ν. This condition ensures that in the limit of large times configurations are generated according to their Boltzmann weight.

As we are interested in critical phenomena, we are concerned by reducing the impact of an effect called critical slowing down. Close to the critical point, the auto-correlation time τ, that is to say the typical number of Monte Carlo steps required to generate a configuration of spins decorrelated from an original configuration, diverges as [2]

$$\tau \sim \xi^z , \tag{2.5}$$

with $z > 0$ a critical exponent and ξ the correlation length which we have already shown to diverge at the critical point. Equivalently, this means that the quantity of new information brought by updating a spin configuration using one Monte Carlo step becomes decreasingly low as we approach the critical point. Thankfully, the exponent z depends on the algorithm and their exist algorithms which prove much more efficient than Metropolis at criticality, displaying smaller values of z.

We have used the Wolff algorithm [40] which considerably reduces the effect of critical slowing down in the critical region. The Wolff algorithm is a cluster algorithm, it is based on building clusters of spins and flipping them collectively instead of flipping each spin individually. At zero magnetic field, the algorithm can be summed up as [2]:

- pick a seed spin at random: it is the first element of the cluster. Only spins of same sign will be allowed to be included in the cluster,
- include in the cluster nearest neighbors of the seed spin with probability $P_{add} = 1 - e^{-2\varkappa J}$, if they have the same sign than the seed spin,
- for each spin newly added to the cluster, include in the cluster its nearest neighbors with probability P_{add}, if they are not already in the cluster and if they have the same sign than the seed spin,
- iterate until all possible new inclusions are rejected,
- flip the cluster.

Like the Metropolis algorithm, the Wolff algorithm is both ergodic and satisfies detailed balance. Figure 2.1a) shows a typical cluster of the Wolff algorithm, generated in a 2D Ising system close to the critical temperature. The average size of the clusters generated by the Wolff algorithm $\langle C \rangle$ depends on temperature, Fig 2.1b). At very high temperature, $P_{add} \approx 0$, so clusters are only composed of the seed spin, and the update is made just by flipping at random a spin in the system, resulting in the expected completely disordered high temperature state. For $T > T_c$, the number of spins in a cluster of the Wolff algorithm is actually directly related to the fluctuations of the magnetization as $\left\langle m^2 \right\rangle = \varkappa \langle C \rangle / N$. At very low temperature, $P_{add} \sim 1$, so that $\langle C \rangle / N \to 1$ and clusters are spread over the entire system. As expected, the very low temperature region sees uniformly ordered systems $\langle m \rangle \to \pm 1$. The Wolff algorithm does not break the magnetization reversal symmetry, a single update at very low temperature will flip the entire system at once, so that the algorithm is fully ergodic. This is a rather consuming strategy in terms of computation time and in this region the Metropolis algorithm, though equivalent in principle, tends to outperform the Wolff algorithm by way of its implementation simplicity. Hybrid algorithm using both Wolff and Metropolis updates can thus prove very efficient. In principle, for the Metropolis algorithm, flipping the entire system at very low temperature is possible, but as flipping a single spin in the almost completely ordered phase has a very low

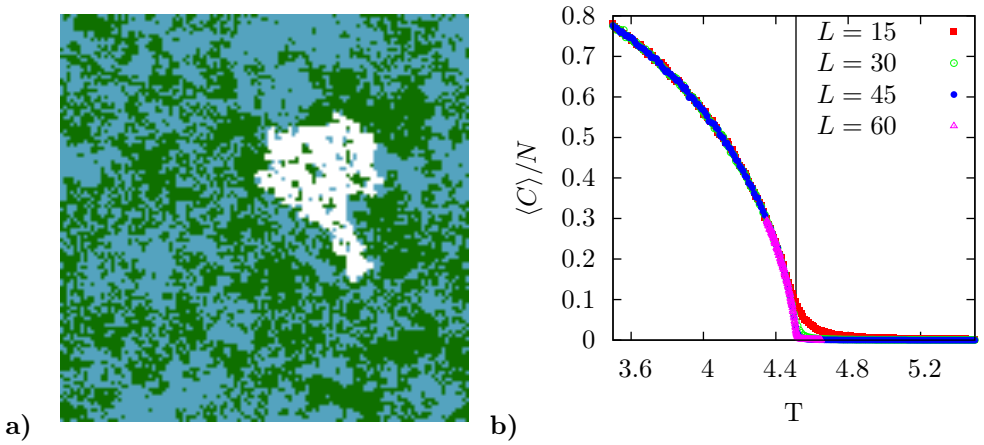

Figure 2.1: **a)** Snap shot of a 2D Ising model close to the critical temperature, at zero magnetic field. Blue and green dots indicate spins pointing up and down, and white dots the cluster flipped by the Wolff algorithm. **b)** Mean size $\langle C \rangle$ of the clusters generated by the Wolff algorithm, at zero magnetic field for a 3D Ising model of volume L^3 with $L \in [15, 30, 45, 60]$. Vertical line gives the location of the bulk critical temperature.

probability, the number of updates required for flipping the entire system diverges, and ergodicity is broken, as is the case for an experimental system.

We have said that a Monte Carlo "step" using the Metropolis algorithm must be defined by N updates using the algorithm, so that the entire system can in principle be modified each step. In the case of the Wolff algorithm, a Monte-Carlo step was defined by first computing the mean size of clusters generated by the Wolff algorithm $\langle C \rangle$ at each temperature and $h = 0$. One Monte-Carlo step is then composed of $N/\langle C \rangle$ calls to the Wolff algorithm, so that, on average, N spin flips are performed each step.

To include a magnetic field, uniform or not, using the Metropolis algorithm is quite straightforward (Eq.2.2 and 2.3) but the Wolff cluster algorithm has been explicitly build in the absence of magnetic field. To include one, spin clusters are created in the same way as for the cluster algorithm at zero magnetic field but the clusters are no longer systematically flipped [41–43]. A first method is to add a "heat bath" step after constructing the cluster, choosing to flip it or not with a probability related to the change in energy $\Delta E = 2h \sum_{i \in C} S_i$ associated with flipping the C spins of the cluster in the magnetic field. This can become a very time consuming strategy as cluster are entirely built prior to choosing to flip them, while they might end up updating no spin at all. We chose to use the "ghost spin" method [41, 42] in which each spin of a cluster can be linked to a ghost spin of fixed value $S_{ghost} = +1$ representing the magnetic field h. The probability of coupling a spin S belonging to the cluster to the ghost spin is $1 - e^{-2\beta Sh}$ if $Sh > 0$ and 0 otherwise: any cluster linked at least once to the ghost spin is left unflipped. Each time a

spin is added to a cluster it is possible to test whether this spin couples to the ghost spin or not. In the case that it does, the growth of the cluster is stopped to save computational time.

2.1.2 Observables and scaling

The configurations generated using the Wolff algorithm do not break the spin reversal symmetry in the absence of a magnetic field. Thus, the average magnetization per spin $\langle m \rangle$ is zero for all temperatures at zero magnetic field (this is also true in principle for sufficiently long runs using solely the Metropolis algorithm), unlike experimental magnets in which the symmetry is spontaneously broken. Consequently, the observable $\langle |m| \rangle$ (which is equivalent to $\langle m \rangle$ in the thermodynamic limit) better represents the symmetry breaking order parameter in this case, as it does signal the phase transition with the limit cases $\langle |m| \rangle \underset{T\to\infty}{\to} 0$ and $\langle |m| \rangle \underset{T\to 0}{\to} 1$. We use fluctuation relations to compute the specific heat

$$C_v(T) = Nc(T) = \left.\frac{\partial \langle \mathscr{H} \rangle}{\partial T}\right|_h = k_B \varkappa^2 \left(\langle \mathscr{H}^2 \rangle - \langle \mathscr{H} \rangle^2 \right) , \tag{2.6}$$

with $c(T)$ the specific heat per spin, and the magnetic susceptibility

$$\chi_N(T) = \frac{\chi}{N} = \frac{1}{N} \left.\frac{\partial \langle M \rangle}{\partial h}\right|_T = \frac{\varkappa}{N} \left(\langle M^2 \rangle - \langle M \rangle^2 \right) , \tag{2.7}$$

As for the order parameter, instead of the above definition of χ we use

$$\tilde{\chi}(T) = \frac{\varkappa}{N} \left(\langle M^2 \rangle - \langle |M| \rangle^2 \right) , \tag{2.8}$$

to ensure that $\tilde{\chi} \underset{T\to 0}{\to} 0$, whereas $\chi_N(T) \propto \langle M^2 \rangle \underset{T\to 0}{\to} 1$ will not be peaked around T_c [30].

Figure 2.2 displays some results for observables in a 3D Ising model on a cubic lattice of volume L^3 with $L \in [15, 30, 45, 60]$. We display the magnetization both at $h = 0$ as a function of T and at $T = T_c$ as a function of h, the susceptibility at $h = 0$ and the specific heat at $h = 0$. It is clear that the finite size of the system has a tremendous influence on the results and that we are far from obtaining the behavior of the observables expected in the thermodynamic limit. Typically, the magnetization $\langle |m| \rangle$ does not go to zero at T_c and the specific heat and susceptibility do not diverge. A genuine phase transition, that is to say displaying a singular behavior, can only occur in a thermodynamically large system. In a finite system, the number of degrees of freedom is finite and the mean value of observables results from an average over a finite number of analytic quantities and can thus only have an analytic behavior. When taking the thermodynamic limit, the number of degrees of freedom goes to infinity and singular behavior is thus possible.

Nevertheless, the scaling behavior expected at the thermodynamic limit can still be observed in finite systems, for which we provide evidence using a logarithmic scale in figure 2.3. We display (black dashed lines) the power law behaviors described in chapter 1 for the magnetization, the susceptibility and the specific heat, using estimates from the literature (see table 1.1) for the

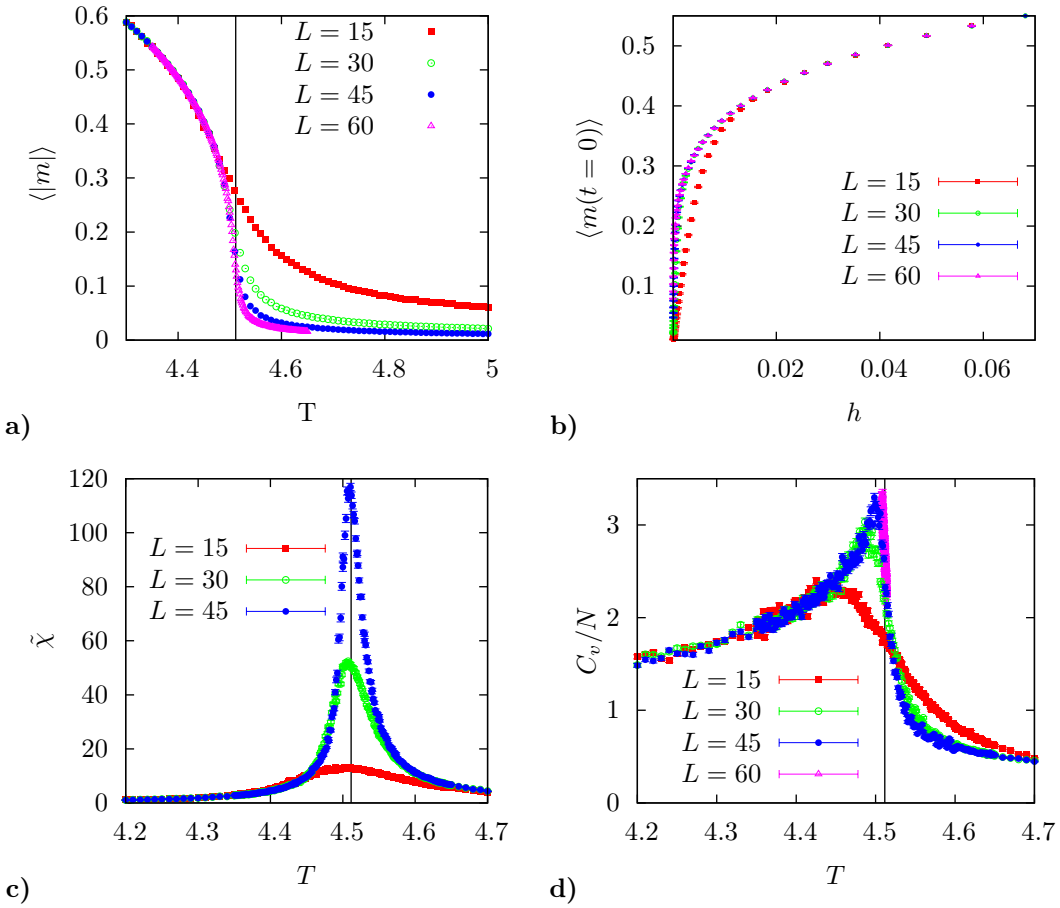

Figure 2.2: Magnetization at zero magnetic field **(a)** and at $T = T_c$ as a function of h **(b)** for a 3D Ising model of volume L^3 with $L \in [15, 30, 45, 60]$. Specific heat per spin **(c)** and susceptibility **(d)** at zero magnetic field for the same systems. Vertical line gives the location of the bulk critical temperature, using an estimate from literature (see table 1.1 and ref. [36]).

exponents and a fit for the amplitudes. For the magnetization and the susceptibility, the data are clearly coherent with the bulk (thermodynamic) scaling behaviors, but only for intermediate values of t or h. Too close to $(t = 0, h = 0)$, the divergence of the correlation length is cut-off by the finite size of the system and observables deviate from the thermodynamic power law behavior. Of course, as observed in figure 2.3, the region, centered on $(t = 0, h = 0)$, on which finite-size effects are dominant decreases with increasing system size.

In the case of the specific heat, the small value of the exponent $\alpha = 0.110(1)$ makes its divergence rather weak. Consequently, finite-size effects are more dramatic and the present system sizes do not allow one to identify clearly the power law behavior (Fig. 2.3d). This illustrates the limitations due to the finite size of lattice simulations. Of course, the failure of

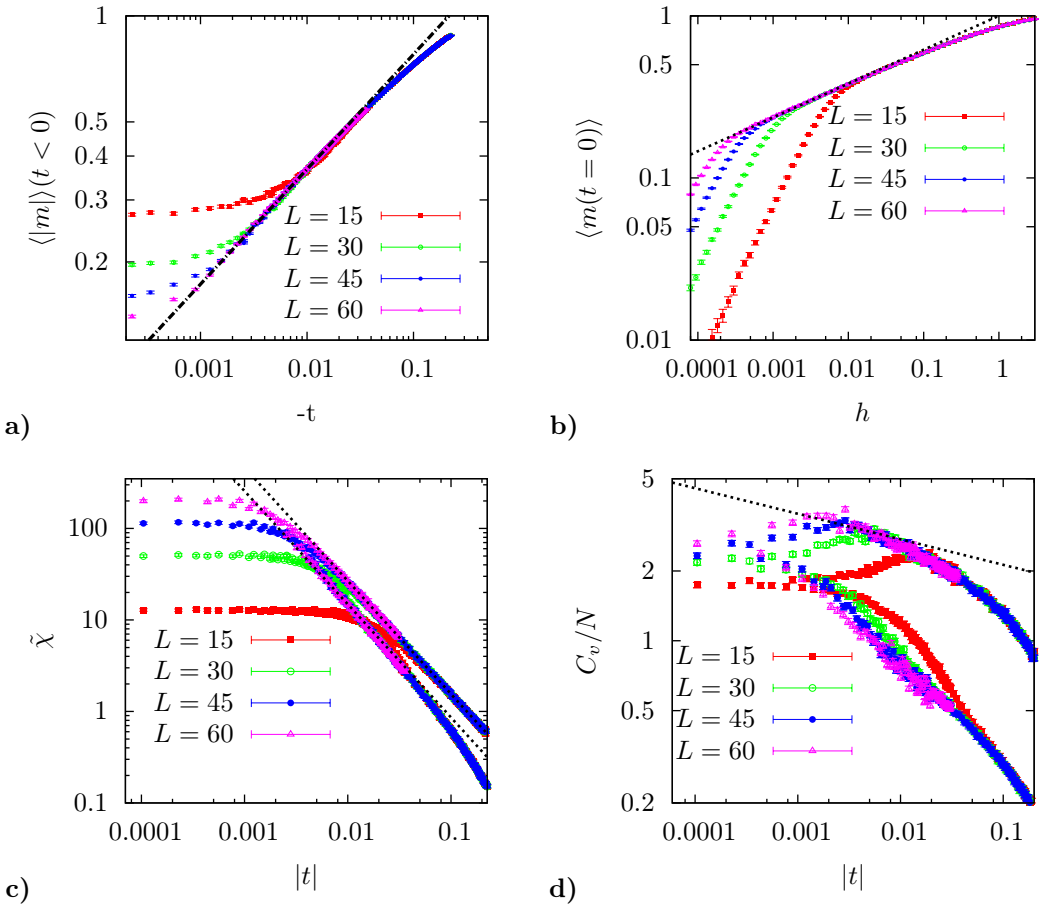

Figure 2.3: Magnetization at zero magnetic field and $t < 0$ **(a)** and at $t = 0$ and positive magnetic field **(b)**, susceptibility **(c)** and specific heat per spin **(d)** of a 3D Ising model of volume L^3 with $L \in [15, 30, 45, 60]$, logarithmic scale. For the susceptibility, the behaviors for $t > 0$ and $t < 0$ are both displayed. Typically, the scaling amplitudes $C_0^{\pm}, \chi_0^{\pm}$ are expected to be different regarding the sign of t. The black dashed lines show power law behaviors using estimates from the literatures (see table 1.1) for the exponents and a fit for the amplitude. In the absence of a magnetic field: $\chi \propto |t|^{-\gamma}$, $C_v/N \propto |t|^{-\alpha}$, $\langle |m| \rangle \propto |t|^{\beta}$. At the critical temperature: $\langle |m| \rangle \propto |h|^{1/\delta}$.

this approach is related to the rather small system size used and we could have pursued our quest for the scaling exponent α by increasing the system size. Moreover, the way we have highlighted scaling behavior in figure 2.3 is only illustrative. If we had not used our prior knowledge on power law behaviors in the Ising model, the rather complex behavior of the observables considered here close to the critical point would have made the identification of a scaling behavior much more difficult. Thermodynamic limit scaling will only be valid over a small interval before finite-

size effects dominates (on the displayed data, we roughly get more than a decade on which the thermodynamic limit scaling holds, in the best case). Identifying this interval and fitting a power law through both amplitude and exponent is thus very complicated.

Thankfully, we will see that the size dependency of the observables can be used to our advantage. As the thermodynamic limit, $L^{-1} \to 0$ is approached, the singularity at the critical point is restored. The inverse of the size L^{-1} can thus be seen as an extra variable to t and h, with the critical point located at $(t, h, L^{-1}) = (0, 0, 0)$, this statement leading to the concept of finite size scaling, which can be seen as a generalization of the scaling hypothesis to finite systems.

2.2 Finite-size scaling

2.2.1 Finite-size scaling of the free energy

In chapter 1, we only considered systems in the thermodynamic limit $L^{-1} \to 0$, where L is the linear size of the system, that we implicitly supposed cubic. As we have illustrated in the previous section, in a finite system the singular part of the free energy has a dependency on the system size, other than the trivial volumic factor that appeared when defining the bulk free energy

$$\omega_{bulk}(T, h) = \lim_{L^{-1} \to 0} \frac{\Omega(T, h, L)}{V k_B T} \ , \tag{2.9}$$

which by definition is an extensive quantity. We have seen in section 1.3.4 that the scaling behavior originated in the divergence of the correlation length at criticality. As long as $\xi \ll L$, the finite size of a system should not change its behavior compared to the thermodynamic limit and bulk behavior is still expected. However, the correlation length cannot outgrow the system size and if $L \sim \xi$, the finite size will cut-off the correlation length, so that L/ξ, with ξ the bulk critical correlation length, becomes a relevant parameter. We have seen in chapter 1 that at zero field, $\xi = \xi_0^{\pm} t^{-\nu}$ so that $L/\xi \propto L t^{\nu}$. At T_c, the bulk correlation length $\xi = \xi_0^h h^{-\nu/(\gamma+\beta)}$, so that $L/\xi \propto L h^{\nu/(\gamma+\beta)}$. We will see that indeed, $(Lt^{\nu}, Lh^{\nu/(\gamma+\beta)})$ are the relevant finite-size scaling variables.

A way of looking at the extension of the scaling hypothesis to finite-size scaling is that a finite number of degrees of freedom cannot give you singular behaviour. Thus, a non-zero parameter L^{-1} suppresses the critical singular behavior, just as a non-zero reduced temperature t or a bulk field h would. The finite-size scaling hypothesis can thus be considered as an extension of the scaling hypothesis, with an extra variable L^{-1} to t and h. In chapter 1, we stated that the scaling hypothesis originated in a homogeneity relation for the singular part of the free energy ω_s^0 (Eq.1.31). An equivalent form can be derived taking the new parameter L^{-1} into account [23, 24, 26]

$$\omega_s(t, h, L) = \ell^{-d} f(\ell^{y_t} t, \ell^{y_h} h, \ell L^{-1}) \ , \tag{2.10}$$

with $y_t = 1/\nu, y_h = (\gamma+\beta)/\nu$ and a third scaling exponent which rather trivially is $y_L = 1$. Choosing $\ell = L$, we get the finite-size scaling form of the singular part of the free energy

$$\omega_s(T,h,L) = L^{-d} f(tL^{1/\nu}, hL^{(\gamma+\beta)/\nu}, 1) \ , \tag{2.11}$$

which, as for the ω_s^0 scaling form, is asymptotically true close enough to the critical point $(t,h,L^{-1}) = (0,0,0)$ and is universal to within non universal amplitudes on the scaling variables [34]. Of course, we expect that, taking the thermodynamic limit, we recover results of chapter 1, so that

$$\omega_s(T,h,L) \underset{L^{-1}\to 0}{\to} \omega_s^0(T,h) \ . \tag{2.12}$$

where one should be careful in taking the limit $L^{-1} \to 0$ before $(T,h) \to (T_c, 0)$. We can define the excess part of the free energy per unit volume in units of $k_B T$, which contains the finite size contribution to the free energy and here amounts to

$$\omega_{ex}(T,h,L) \equiv \frac{\Omega(T,h,L)}{V k_B T} - \omega_{bulk} = \omega_s(T,h,L) - \omega_s^0(T,h) \ . \tag{2.13}$$

which by definition vanishes in the thermodynamic limit $\omega_{ex} \underset{L^{-1}\to 0}{\to} 0$. Here we confine ourselves to the case of periodic boundary conditions. Further, we will see that with non-periodic boundary conditions, a surface contribution $\omega_{surf}(T,h)$ has to be taken into account in addition to the bulk, giving a contribution to the excess free energy. As a consequence, the form of the finite size scaling function of the excess free energy is modified by the type of boundary conditions imposed.

2.2.2 Finite-size scaling of observables

Just as we have deduced scaling behavior of observables from the scaling form of the free energy ω_s^0 in chapter 1, we can deduce finite-size scaling forms for observables from the finite-size scaling of the free energy (Eq.2.20)

$$\begin{aligned} c &= L^{\alpha/\nu} c_s \left(tL^{1/\nu}, hL^{(\gamma+\beta)/\nu} \right) \ , \\ N\tilde{\chi} &= L^{\gamma/\nu} \chi_s \left(tL^{1/\nu}, hL^{(\gamma+\beta)/\nu} \right) \ , \\ \langle m \rangle &= L^{-\beta/\nu} m_s \left(tL^{1/\nu}, hL^{(\gamma+\beta)/\nu} \right) \ , \end{aligned} \tag{2.14}$$

which clearly describe the cut-off of diverging quantities and rounding of singular behavior in general. We can also define a finite-size scaling function for the correlation length

$$\xi = L\xi_s \left(tL^{1/\nu}, hL^{(\gamma+\beta)/\nu} \right) \ , \tag{2.15}$$

which clearly describes the cut-off of its divergence by the finite size of the system, so that $\xi \propto L$ at $(t,h) = (0,0)$, and for $\langle |m| \rangle$ [44]

$$\langle |m| \rangle = L^{-\beta/\nu} \bar{m}_s (tL^{1/\nu}, hL^{(\gamma+\beta)/\nu}) \ , \tag{2.16}$$

even though they do not directly stem from Eq.2.11. We can test these scaling forms, using predictions from literature for the critical exponents and the critical temperature (see table 1.1), by showing that using the reduced form

$$\begin{aligned} cL^{-\alpha/\nu} &= c_s(tL^{1/\nu}, 0) \ , \\ N\tilde{\chi}L^{-\gamma/\nu} &= \chi_s(tL^{1/\nu}, hL^{(\gamma+\beta)/\nu}) \ , \\ \langle|m|\rangle L^{\beta/\nu} &= \bar{m_s}(tL^{1/\nu}, 0) \ , \\ \langle m\rangle L^{\beta/\nu} &= m_s(0, hL^{(\gamma+\beta)/\nu}) \ . \end{aligned} \tag{2.17}$$

we get a collapse on a single master curve of data obtained in systems of different sizes. Figures 2.4a,b,c) display results obtained in cubic 3D Ising models of volume L^3 with $L \in [15, 30, 45, 60]$ for the magnetization and susceptibility, showing a very convincing collapse on a wide range of temperature and magnetic field. Finite-size scaling is thus a powerful tool for interpreting data obtained in a finite size system. Rather than trying to identify narrow regions of t and h in which the bulk behavior is valid (Fig. 2.3), one can take advantage of finite-size scaling forms, for example to extract critical exponents and the critical temperature, using them as a fitting parameters to reach the best data collapse.

The collapse of the specific heat c (Fig. 2.4d) appears less convincing, though quite good close to $tL^{1/\nu} = 0$. To build the finite-size scaling forms of Eq.2.17, we have implicitly assumed that the singular contribution to the free energy was clearly dominant. This is too strong an assumption in the case of the slowly diverging specific heat. In general [45, 46]

$$c(T, h, L) = L^{\alpha/\nu} c_s\left(tL^{1/\nu}, hL^{(\gamma+\beta)/\nu}\right) + c_a(T, h) \ , \tag{2.18}$$

where c_a is an analytic background. To estimate the effect of this analytic background, we estimated the value of $c_a(T_c, h = 0)$ and $c_s(0, 0)$ by a fit to $c(T_c, 0, L)$ as a function of $L^{\alpha/\nu}$, finding $c_a(T_c, h = 0) = 1.3(3)$, which compares well with results of ref. [45]. We thus use the corrected scaling form

$$(c(T, h, L) - c_a(T_c, 0))L^{-\alpha/\nu} = c_s\left(tL^{1/\nu}, hL^{(\gamma+\beta)/\nu}\right) \ , \tag{2.19}$$

in figure 2.4e), greatly improving the data collapse. To improve the collapse even further, one would need to take into account the dependency of the analytic term on T. Here we will not develop further this point, which is only meant to be illustrative.

2.2.3 Corrections to finite-size scaling

We have mentionned that finite-size scaling is only exact asymptotically close to the critical point $(t, h, L^{-1}) = (0, 0, 0)$. Getting away from this point, corrections to finite-size scaling might become relevant, just as corrections to scaling were for the thermodynamic scaling behavior (see section 1.3.6). As in the thermodynamic limit, irrelevant fields can enter the homogeneity

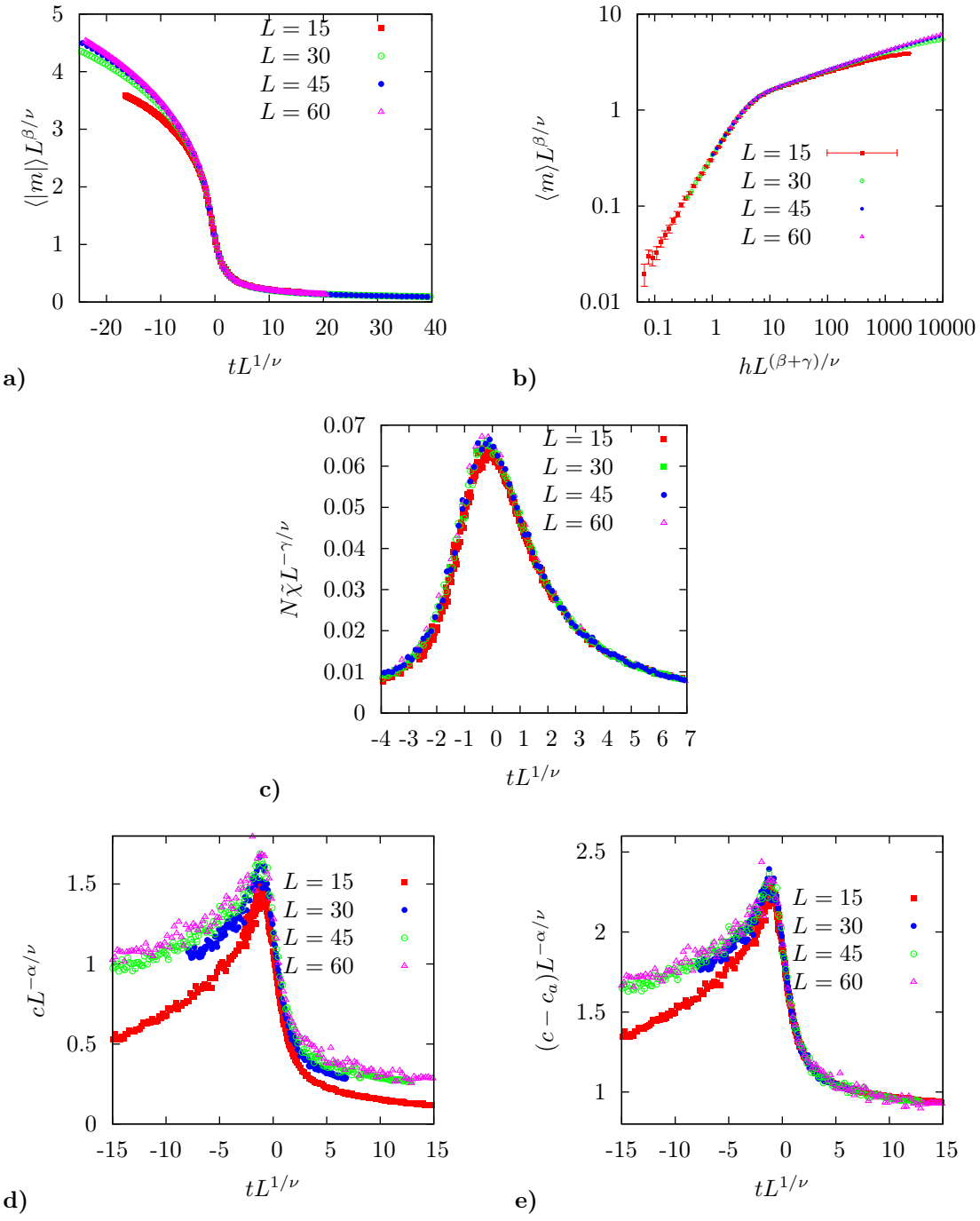

Figure 2.4: Finite-size scaling applied to data obtained in cubic 3D Ising models of volume L^3 with $L \in [15, 30, 45, 60]$: magnetization at zero magnetic field **(a)** and at $t = 0$ with non zero magnetic field **(b)**, susceptibility **(c)** and specific heat per spin **(d,e)**. Data collapse is poor at the maximum of $cL^{-\alpha/\nu}$, though rather good at $t = 0$. An analytic background c_a to c can be suppressed **(e)**, improving the collapse. We used estimates from the literatures for the exponents and critical temperature (see table 1.1).

relation for the singular part of the free energy density [4]

$$\omega_s(t,h,L) = \ell^{-d} f(\ell^{y_t} t, \ell^{y_h} h, \ell L^{-1}, \ell^{y_3} \tilde{K}_3, \dots) \ , \tag{2.20}$$

which give rise to corrections to the finite-size scaling behavior of Eq. 2.11. For example, a high precision measurement of the critical exponent η using finite size scaling of the susceptibility at $(t,h) = (0,0)$ might require one to take corrections into account and use the form [46].

$$\chi = L^{2-\eta} \chi_s(0,0)(1 + b_1 L^{-\omega} + \dots) + \chi_a \ , \tag{2.21}$$

with χ_a an analytic background and b_1 a non universal amplitude for the leading correction to scaling $L^{-\omega}$ ($\omega = 0.84(4)$ in the Ising model [4]).

2.2.4 Apparent critical temperature and Binder cumulant

We have mentioned that the value of the critical temperature T_c could be estimated by using it as a fitting parameter to obtain the best data collapse of an observable. The critical temperature being the temperature at which the specific heat (and susceptibility) diverges, one can use the temperature at which the specific heat (or the susceptibility) is maximum to define an effective critical temperature $T_c(L)$, clearly depending on L as can been seen in figure 2.2. This apparent temperature approaches the thermodynamic value of T_c with increasing size as [30]

$$T_c(L) = T_c + \lambda_T L^{-1/\nu}(1 + b_T L^{-\omega}) \ , \tag{2.22}$$

where λ_T, b_T are model dependent constants, taking into account a correction term $L^{-\omega}$. Using this form, T_c can be deduced from a fit of $T_c(L)$ as a function of L.

It is also possible to define, using finite-size scaling, a quantity which is independent of L at T_c such as the fourth order cumulant, or Binder cumulant [30]

$$U_4 = 1 - \frac{\langle m^4 \rangle}{3\langle m^2 \rangle^2} \ , \tag{2.23}$$

as both $\langle m^4 \rangle$ and $\langle m^2 \rangle^2$ are proportional to $L^{-4\beta/\nu}$ at T_c in the scaling limit. Thus, the crossing point of U_4 computed in systems of different size L gives an estimate of T_c, see figure 2.5. We see that the crossing point is very close to a high precision estimate of $T_c = 4.511528$ found in the literature (see table 1.1), our best estimate being $T_c^{Binder} = 4.5114 \pm 6.10^{-4}$. We notice that the crossing point changes slightly when increasing the size L: the Binder cumulant too undergoes corrections to scaling [30, 46], which have to be taken into account to increase the accuracy on the estimation of T_c.

2.2.5 Experimental finite-size scaling

Finite-size scaling is not only a tool for numerical studies. It is experimentally relevant in magnetic thin films but also in fluid systems. For example, the finite size dependency of $T_c(L)$

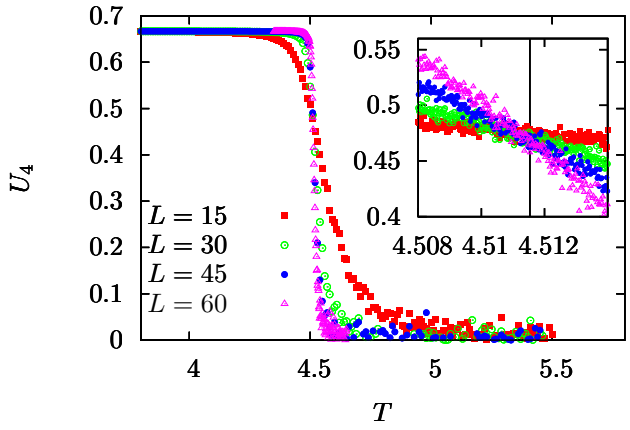

Figure 2.5: Binder cumulant U_4 at zero magnetic field for a 3D Ising model of volume L^3 with $L \in [15, 30, 45, 60]$. **Inset:** blow up of the crossing region, the vertical line localizes an estimate of the bulk critical temperature from literature (see table 1.1).

discussed in the previous section has been observed in magnetic thin films and nano-particles [10–12]. Measurements of finite size effects require that one stabilizes the system sufficiently close to its critical point for the correlation length to develop up to the system size. For example, in ^4He close to a superfluid transition (belonging to the XY model universality class), the critical end point at which the lambda line of normal/superfluid transitions meet the liquid/gas line of phase transitions is located at $T_\lambda = T_c = 2.1786K$ [6] and the correlation length amplitude is $\xi_0 = 0.1422(5)\,\mathrm{nm}$ [9]. Thus, if one achieves a relative precision on temperature $t \sim 10^{-4}$, the correlation length can develop up to $\xi = \xi_0 t^{-\nu} = (10^{-4})^{-0.67115} \times 0.1422\,\mathrm{nm} \sim 70\,\mathrm{nm}$. This small order of magnitude gives an idea of the difficulty of measuring finite size effects. Nevertheless, this particular example has lead to very high precision measurement: for example, successful finite size scaling analysis of specific heat measurements in confined geometries [7–9].

We will discuss again experimental finite-size scaling in chapter 4, in which we present the critical Casimir force. The critical Casimir force is fostered by the confinement of critical fluctuations of a medium undergoing a continuous phase transition. It can be seen as a consequence of finite-size scaling: the free energy density depends on the system size in confined critical systems (Eq. 2.11), consequently leading to a critical contribution to the pressure. This effect, first predicted by Fisher and de Gennes in 1978 [15], has been at the heart of many theoretical, numerical and experimental works for decades (see ref. [47] for a review on the subject). One of its fascinating features is universality: we can define a scaling function θ for the critical Casimir pressure

$$f_c = k_B T L_\perp^{-d} \theta \left(t L_\perp^{1/\nu}, \tilde{h} L_\perp^{(\beta+\gamma)/\nu} \right) , \tag{2.24}$$

which, like the other scaling functions discussed in this chapter, is universal. In the present work,

we will be interested in computing this function in the Ising universality class.

2.3 Conclusion

We have seen that in a finite-size system, the divergence of the correlation length is cut-off by the finite size, resulting in the rounding of singular behavior. This is well captured by the theory of finite-size scaling, which can be seen as an extension of scaling as it is expressed in the thermodynamic limit (see chapter 1). Finite-size scaling provides powerful tools to study critical phenomena in simulations, in which system sizes are quite small due to the limitation of computational resources. However, it is no longer confined to this role as it is now proving experimentally relevant in confined critical systems.

In the present work, we are particularly interested in one of these phenomena: the critical Casimir force. It will be the subject of chapters 4 to 7. In the present chapter, we have solely studied cubic systems, but we will see in chapter 4 that a convenient and experimentally relevant geometry to study the Casimir force is the slab geometry, in which a confining dimension $L_\perp$ is clearly identified. We will show in detail how this force is related to finite-size scaling in this geometry.

Hence, before detailing our work on the critical Casimir force, we have found it relevant and insightful to study, in chapter 3, how fluctuations develop at the critical temperature in a confined system. We will make the transition between cubic and slab geometries by putting the emphasis on the influence of the aspect ratio of a system on the fluctuations of the order parameter. Moreover, the influence on the fluctuations of fixed boundary conditions in the confining direction, rather than periodic, will also be studied. We will then see in the following chapter that the strong influence of boundary conditions on fluctuations in confined geometries has also a major impact on the form of the critical Casimir force.

Chapter 3

Critical Fluctuations of the Order Parameter of the Ising Model

In chapter 2, we have seen that the limitations of computer capacities and algorithms makes simulations system sizes small compared to experimental setups. Finite-size scaling (FSS) is a powerful tool for the interpretation and exploitation of the thermodynamics of confined critical systems [1] and has proved to be of experimental relevance, particularly in the case of critical Casimir forces which are the main subject of this thesis. In the present chapter, we are interested in the form of fluctuations of the order parameter in confined critical two and three dimensional Ising models through the scaling behavior of the magnetization probability density. In chapter 2, we confined ourselves to systems with cubic geometry. However, we will see in chapter 4 that the slab geometry is more relevant to experimental approaches of finite-size scaling, particularly in studies of the critical Casimir force, which will be the topic of chapters 4 to 7. Thus, we will make the transition between cubic and slab geometries by putting the emphasis on the influence of the aspect ratio of a system on the fluctuations of the order parameter. We will study systems of dimensions $L_\perp \times L_\parallel^{d-1}$, Fig.3.1, with one confining dimension $L_\perp$ and $d-1$ non-confining ones $L_\parallel \geq L_\perp$. Moreover, in chapter 2, we only presented the case of fully periodic boundary conditions (BC). It is quite intuitive that the presence of boundary fields will deeply influence the fluctuations. We will study this influence by using fixed $(+,\pm)$ boundary conditions in the confining direction z and see that in the slab limit $L_\parallel \gg L_\perp$ the probability distribution of the magnetization tends to a Gaussian form whatever the boundary conditions.

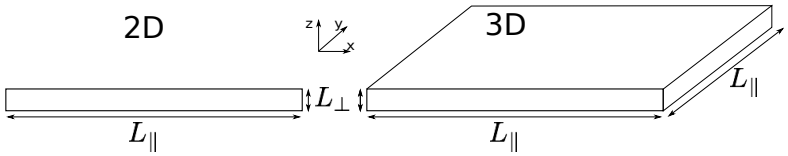

Figure 3.1: The slab geometry in 2 and 3 dimensions.

3.1 Form of the magnetization probability distribution and finite-size scaling

At zero magnetic field and far from the critical temperature T_c, that it to say when the correlation length ξ is small with respect to all system sizes, two regimes can be identified [1, 48]. At a temperature T much higher than the critical temperature, thermal fluctuations dominate and the central limit theorem applied to the uncorrelated spins leading to a Gaussian distribution

$$P(m,T,N) = \sqrt{\frac{N}{2\pi\chi(T)}} e^{-Nm^2/2\chi(T)} \tag{3.1}$$

for the probability density of the magnetization per spin m, with the magnetic susceptibility χ being independent of the total number of spins N [30]. At temperatures much lower than T_c, $P(m,T,N)$ is double peaked, symmetrically around 0, the positions of the peaks are N independent but their width evolves as $N^{-1/2}$ [48]. We are interested in the behavior close to T_c, in between these two limit cases.

The starting point of our finite size scaling hypothesis is the very general statement that for any distribution Π of a stochastic quantity x

$$\Pi(x) = (1/\sigma_x)\tilde{\Pi}(x/\sigma_x), \tag{3.2}$$

with $\sigma_x = \sqrt{\langle x^2\rangle - \langle x\rangle^2}$ the standard deviation, where $\langle . \rangle$ stands for a statistical average. For example, this statement is obviously verified if the distribution is a door function for which the width is $\sqrt{12}\sigma_x$ and amplitude $1/(\sqrt{12}\sigma_x)$ or a Gaussian $\Pi(x) = \frac{1}{\sqrt{2\pi\sigma_x^2}} \exp\left(-\frac{x^2}{2\sigma_x^2}\right)$.

In a thermodynamically large system, the correlation length diverges when the temperature approaches T_c as $\xi \propto |t|^{-\nu}$ with $t = \frac{T-T_c}{T_c}$ the reduced temperature. In a finite system this divergence is cut-off by the confining size L of the system and the ratio L/ξ becomes a relevant parameter, leading to finite-size scaling. It then follows from Eq.3.2 that the magnetization probability distribution function verifies [49] :

$$P(m,L,t) = (1/\sigma)\bar{P}(m/\sigma, L/\xi), \tag{3.3}$$

with $\sigma = \sqrt{\langle m^2\rangle - \langle m\rangle^2}$ the standard deviation of the reduced magnetization and the temperature dependency being governed by L/ξ, with $\xi = \xi_0^{\pm} t^{-\nu}$ the bulk correlation length. For a square 2D or cubic 3D system of side length L, and total number of spins $N = L^d$, with d the spatial dimension, the magnetization probability distribution takes a finite-size scaling form in the scaling limit [50, 51]

$$P(m,L,t) = L^{\beta/\nu}\tilde{P}(mL^{\beta/\nu}, tL^{1/\nu}), \tag{3.4}$$

with β and ν scaling exponents taking their usual meaning and $\tilde{P}$ a scaling function depending both on dimension and boundary conditions. The values of the scaling exponents β, ν depend

on the system dimension d. However, for the sake of simplicity, we do not explicitly express this dependence, but assume that we use the relevant values when considering either the 2D or 3D probability density (we used the values summed up in table 1.1). This form of the probability density is valid in both two and three dimensions where hyperscaling (Josephson relation) holds. The scaling forms of Eq.3.3 and Eq.3.4 are shown to be equivalent by using the hyperscaling relation and stating that the susceptibility is related to the standard deviation $\chi = N\sigma^2 \propto L^{\gamma/\nu}$ in the scaling limit, so that [49, 50, 52, 53]:

$$\sigma \propto L^{-\beta/\nu}. \tag{3.5}$$

Much richer behavior occurs in systems with non square, respectively non cubic, shapes. We are interested in systems in slab geometry of dimensions $L_\perp \times L_\parallel^{d-1}$ with one confining dimension $L_\perp$ and $d-1$ non-confining ones $L_\parallel \geq L_\perp$. To clearly identify $L_\perp$ as the confining size, that is to say the one that will compete with ξ and cut-off its divergence at the critical temperature, we shall keep in all cases $L_\parallel \geq L_\perp$. The aspect ratio $\rho = L_\perp/L_\parallel$ will govern the functional form of the distribution [54], leading to a straight forward generalization of Eq.3.3:

$$P(m, L_\perp, L_\parallel, t) = (1/\sigma)\hat{P}(m/\sigma, L_\perp/\xi, \rho), \tag{3.6}$$

with $\hat{P}(m/\sigma, \xi/L, 1) = \tilde{P}(m/\sigma, L/\xi)$. In the limit $L_\parallel \gg L_\perp$, the argument that led to Eq.3.5 can be extended to the slab geometry : as $L_\perp$ is clearly identified as the confining dimension that will cut-off the diverging correlation length, so that $\xi \propto L_\perp$ in the scaling limit at criticality, the magnetic susceptibility scales as $\chi \propto L_\perp^{\gamma/\nu}$. Using the fluctuation-dissipation relation $\chi = N\sigma^2$, with $N = L_\perp L_\parallel^{d-1}$ and the hyperscaling relation, we get:

$$\sigma = \hat{\sigma} L_\perp^{-\beta/\nu} \rho^{(d-1)/2}, \tag{3.7}$$

which has been shown to hold in $d = 2$ [55] and that we will show to work in $d = 3$ in the following. Then, Eq.3.6 and Eq.3.7 lead us to propose the following scaling form for the magnetization distribution at $t = 0$ when the limit $L_\parallel \gg L_\perp$ is approached :

$$P(m, L_\perp, L_\parallel, t = 0) = L_\perp^{\beta/\nu} \rho^{-(d-1)/2} \hat{P}\left(m L_\perp^{\beta/\nu} \rho^{-(d-1)/2}, 0, 0\right). \tag{3.8}$$

Moreover, the scaling function $\hat{P}(x, 0, 0)$ is expected to be Gaussian,

$$\hat{P}(x, 0, 0) = \frac{1}{\sqrt{2\pi\hat{\sigma}^2}} \exp\left(-\frac{x^2}{2\hat{\sigma}^2}\right). \tag{3.9}$$

The origin of the Gaussian form of the distribution at T_c can be understood by stating that in the scaling limit with $L_\parallel \gg L_\perp$ the cut-off of the correlation length will be solely determined by the confining length $L_\perp$ so that the system can be divided in a number $N_{\text{ind}} \propto N/L_\perp^d$ of uncorrelated regions of volume $\xi^d \sim L_\perp^d$. In a sub-volume $L_\perp^d$ the magnetization fluctuates with $\sigma_{sv} \propto L_\perp^{-\beta/\nu}$ as stated in Eq.3.4 [50]. The N_{ind} sub-volumes being uncorrelated, the central-limit theorem tells us that the total magnetization will tend to have Gaussian fluctuations of

standard deviation $\sigma = \sigma_{sn}/\sqrt{N_{\rm ind}}$, as N_{ind} is increased. The scaling standard deviation $\hat{\sigma}$ is a non-universal quantity, it relates to non-universal scaling amplitudes of χ and ξ, and depends on the boundary conditions, as we will see in the following.

3.2 Numerical method

We have tested numerically these predictions for the scaling form of the probability distribution through Monte-Carlo simulation. We recall the Ising model Hamiltonian :

$$\mathscr{H} = -J \sum_{<i,j>} S_i S_j, \tag{3.10}$$

where the sum runs over all pairs of nearest neighbors, J is the coupling constant set here to $J = 1$ for convenience and S_i are spins of value ± 1. The spins are set on a cubic lattice of dimensions $L_{\parallel}^{d-1} \times L_{\perp}$ and were updated through a hybrid Wolff/Metropolis algorithm [40, 56] to reduce critical slowing down. By counting the number of occurrence $\mathscr{N}(m)$ of each possible value m of the reduced magnetization

$$\hat{m} = \frac{1}{N} \sum_{i=1}^{N} S_i \ , \tag{3.11}$$

where $N = L_{\perp} L_{\parallel}^{d-1}$ is the total number of spins, we can estimate the probability for the system to exhibit a reduced magnetization m

$$P(m) = \frac{1}{Z} \sum_{\{S_i\}} e^{-\beta \mathscr{H}} \delta(m - \hat{m}), \tag{3.12}$$

where $Z = \sum_{\{S_j\}} e^{-\beta \mathscr{H}}$ is the partition function, and the sum runs over all possible spin configurations. The total number of spins N in the system fixes the discrete number of values the magnetization can take so that

$$P(m) = \frac{N}{2} \mathscr{N}(m) \ , \tag{3.13}$$

ensuring that the normalization $\int_{-1}^{1} P(m) \mathrm{d}m = 1$ is conserved whatever the system size.

In two dimensions, only the case of fully periodic BC was investigated. In three dimension, periodic BC were always set in the x, y directions (Fig. 3.1) while in the confining z direction either periodic, or fixed BC were used. Fixed boundary conditions were realized by considering that the system is confined in the z direction between two layers of spins with fixed values, either positive $(+)$ or negative $(-)$. We use the convention that $L_{\perp}$ refers to the number of layers of fluctuating spins, whatever the boundary conditions [57–59]. Both the symmetric $(++)$ and anti-symmetric $(+-)$ cases were investigated. For a magnetic system, this amounts to putting a magnetic field acting only on boundary spins, with the limit case of fixing the value of boundary

spins to either positive (+) or negative (−) value. In the case of a binary fluid, this is equivalent to having walls which preferentially adsorbs one of its two components (we will come back in chapter 4 to such comparisons and on the influence of the BCs on the critical Casimir force).

3.3 2D systems with fully periodic boundary conditions

In two dimensions, periodic boundary conditions were set in all directions. We computed the probability distribution $P(m)$ at the critical temperature T_c^{2D} for different confining dimensions $L_\perp \in [10:60]$ and aspect ratios, ranging from the square case $\rho = 1$ to $\rho = 1/100$. As can be seen in Figure 3.2a) the aspect ratio affects the functional form of the distribution which goes from a bimodal one for square systems to a monomodal form as we get closer to the limit $L_\parallel \gg L_\perp$.

Plotting $L_\perp^{-\beta/\nu} P$ as a function of $mL_\perp^{\beta/\nu}$, see figure 3.2b), gives a convincing collapse of distributions obtained for systems with similar aspect ratios, , as expected from [54] and from Eq.3.4 and Eq.3.6. In the square case the collapse is imperfect at the maxima of the distribution for the smallest system sizes studied $L_\perp = 10$ which makes us suspect corrections to the scaling limit.

Particularizing systems with aspect ratios $\rho \leq 1/27$ for which the distribution has reached a monomodal form, we can see in figure 3.2c) that the expected Gaussian behavior in the limit $L_\parallel \gg L_\perp$ [55] and the scaling form of Eq.3.8 are very well verified. We shall stress that in this limit, all the magnetization distributions collapse according to Eq.3.8, and not only those for systems with similar aspect ratios. A Gaussian fit (Eq.3.9) performed on the reduced distribution for the biggest system size available proved excellent, with a standard deviation $\hat{\sigma} = 1.6835(35)$. We recall that a Gaussian distribution is entirely characterized by its two first moments (the mean and the standard deviation). Here, with periodic boundary conditions, the third moment is null by symmetry, so that the lowest order moment of the distributions characterizing their difference from a Gaussian form is the fourth, or kurtosis:

$$\gamma_2 = \frac{\langle (m - \langle m \rangle)^4 \rangle}{\sigma^2} - 3, \tag{3.14}$$

shown in figure 3.2d). We mention that the excess kurtosis is proportional to the Binder Cumulant $U_4 = -3\gamma_2$ [50] which, in the scaling limit, is used to estimate the critical temperature as it is a universal constant with respect to the system size $L_\perp$ at T_c (see section 2.2.4). This this coherent with our observation that, Fig.(3.2d), the kurtosis does not depend on the confinement $L_\perp$ within our current precision. The kurtosis only depends on the aspect ratio ρ. As ρ is decreased the kurtosis goes to zero, making it a suitable quantity to characterize the Gaussian form of the distribution when reaching the limit of slab geometry.

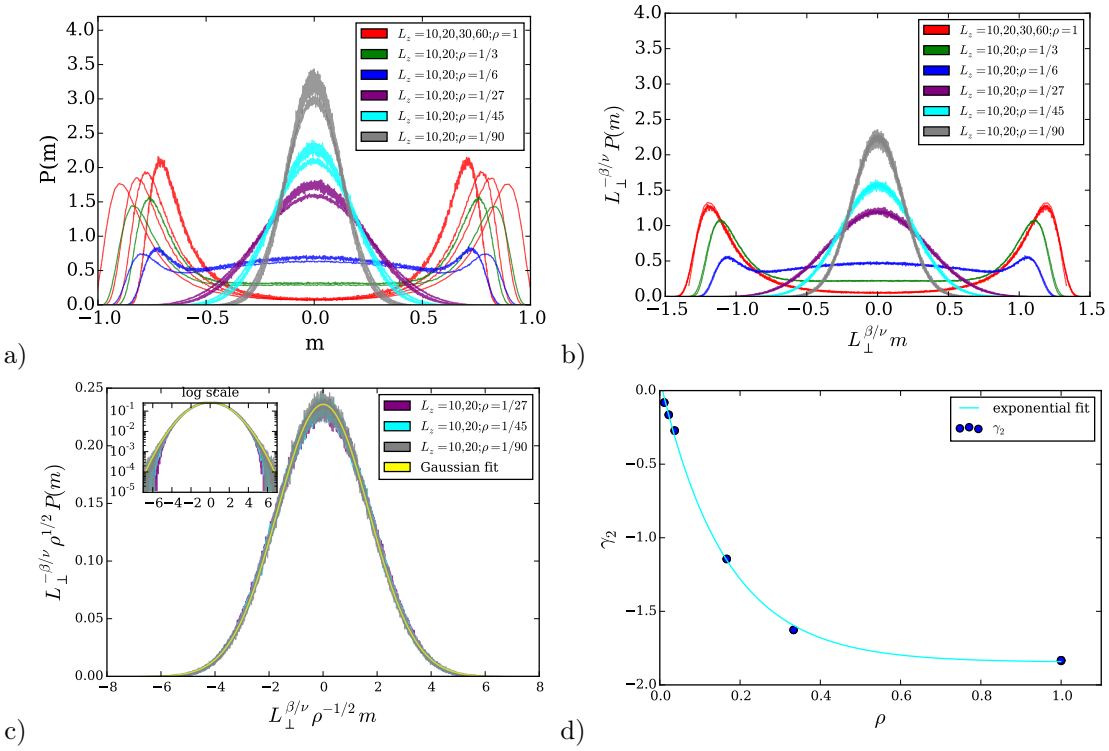

Figure 3.2: **a)** $P(m)$ obtained in a 2D Ising system with fully periodic boundary conditions at the critical temperature $T = T_c^{2D}$. Different total number of spins $N = L_\perp L_\parallel$, thicknesses $L_\perp$ and aspect ratio ρ were investigated. As the aspect ratio is changed from the square case $\rho = 1$ towards the limit $L_\parallel \gg L_\perp$, the functional form of the distribution goes from a bimodal to a monomodal one. **b)** $L_\perp^{-\beta/\nu} P$ vs $m L_\perp^{\beta/\nu}$ for the same system sizes. The curves for systems with the same aspect ratio ρ collapse [54]. **c)** $L_\perp^{-\beta/\nu} \rho^{1/2} P$ vs $m L_\perp^{\beta/\nu} \rho^{-1/2}$ displayed only for monomodal distributions. The expected scaling from Eq.3.8 in the limit $L_\parallel \gg L_\perp$ seems to be valid. The continuous line is a Gaussian fit which proves excellent [55]. **Inset :** same, with logarithmic scale. **d)** Kurtosis γ_2 of all the distributions as a function of ρ. The continuous line is an exponential fit intended as a guide to the eye. The kurtosis does not depend on the confinement $L_\perp$ but only on the aspect ratio ρ.

3.4 3D systems with fully periodic boundary conditions

In three dimensions, periodic boundary conditions were always set in the "parallel" x, y directions. In the confining z direction, different BC were used, but in order to extend the results of the previous section to the 3D case we start with the fully periodic BC case.

With fully periodic boundary conditions, the evolution of $P(m)$ with the aspect ratio at the critical temperature in three dimensions is qualitatively equivalent to the two dimensional case. As figure 3.3a) shows, as ρ is changed from 1 to 1/12 the distribution $P(m)$ evolves from a bimodal to a monomodal functional form [54]. Equivalently to the 2D case, Eq.3.6 is verified as plotting $L^{-\beta/\nu}P$ as a function of $mL^{\beta/\nu}$ gives a convincing collapse of distributions for systems with the same aspect ratio, the functional form of the collapse depending on the aspect ratio, see figure 3.3b).

In the case of cubic $\rho = 1$ systems, a high resolution study of the Ising and spin-1 Blume-Capel models [60] has shown the functional form:

$$P(m) \propto \exp\left(-\left(\frac{M^2}{M_0^2 L^{-2\beta/\nu}} - 1\right)^2 \left(a\frac{M^2}{M_0^2 L^{-2\beta/\nu}} + c\right)\right) \tag{3.15}$$

with $L = L_\perp = L_\parallel$ and a, c, M_0 non-universal factors which may contain corrections to scaling, to accurately fit the probability distribution. This result can be made consistent with the scaling form of Eq.3.4 by using the form

$$L^{-\beta/\nu}P = P_0 \exp\left(-\left(\frac{M^2}{M_0^2 L^{-2\beta/\nu}} - 1\right)^2 \left(a\frac{M^2}{M_0^2 L^{-2\beta/\nu}} + c\right)\right), \tag{3.16}$$

in which we fitted a, c, P_0, M_0 to an excellent agreement, see Fig. 3.3c).

Figure 3.3d) shows $L_\perp^{-\beta/\nu}\rho^{(d-1)/2}P$ as a function of $mL_\perp^{\beta/\nu}\rho^{-(d-1)/2}$ following the scaling form proposed in Eq.3.8 for monomodal distributions, that is to say for $\rho \leq 1/6$, which collapse whatever the aspect ratio. A Gaussian fit (Eq.3.9) of the reduced distribution for the biggest system available indicates that the Gaussian behavior predicted in 2D in the limit $L_\parallel \gg L_\perp$ by [55] holds in 3D, with $\hat{\sigma} \approx 2.54$. Thus, the scaling form proposed in Eq.3.8 appears verified in 3D as it was in 2D. Yet, the collapse is a little less convincing, probably because we could not as easily reach large values for $L_\parallel$. Nevertheless, the Gaussian behavior clearly is approached in the limit $\rho \to 0$. Following Eq.3.7, approaching this limit, $L_\perp^{-\beta/\nu}\rho\sigma = \hat{\sigma}$. This can be verified by looking at the dependency of $L_\perp^{-\beta/\nu}\rho\sigma$ on ρ, Fig. 3.3e), which indeed displays a saturation close to $\rho = 0$ at a value close to $\hat{\sigma} \approx 2.4$. Moreover, as in 2D, we used the kurtosis to characterize the evolution of the distribution towards a Gaussian when reaching the limit of slab geometry, Fig. 3.3f). The kurtosis only slightly depends on the confinement $L_\perp$ in the cubic $\rho = 1$ case but strongly on the aspect ratio, approaching zero as $\rho \to 0$, confirming that we approach Gaussian behavior.

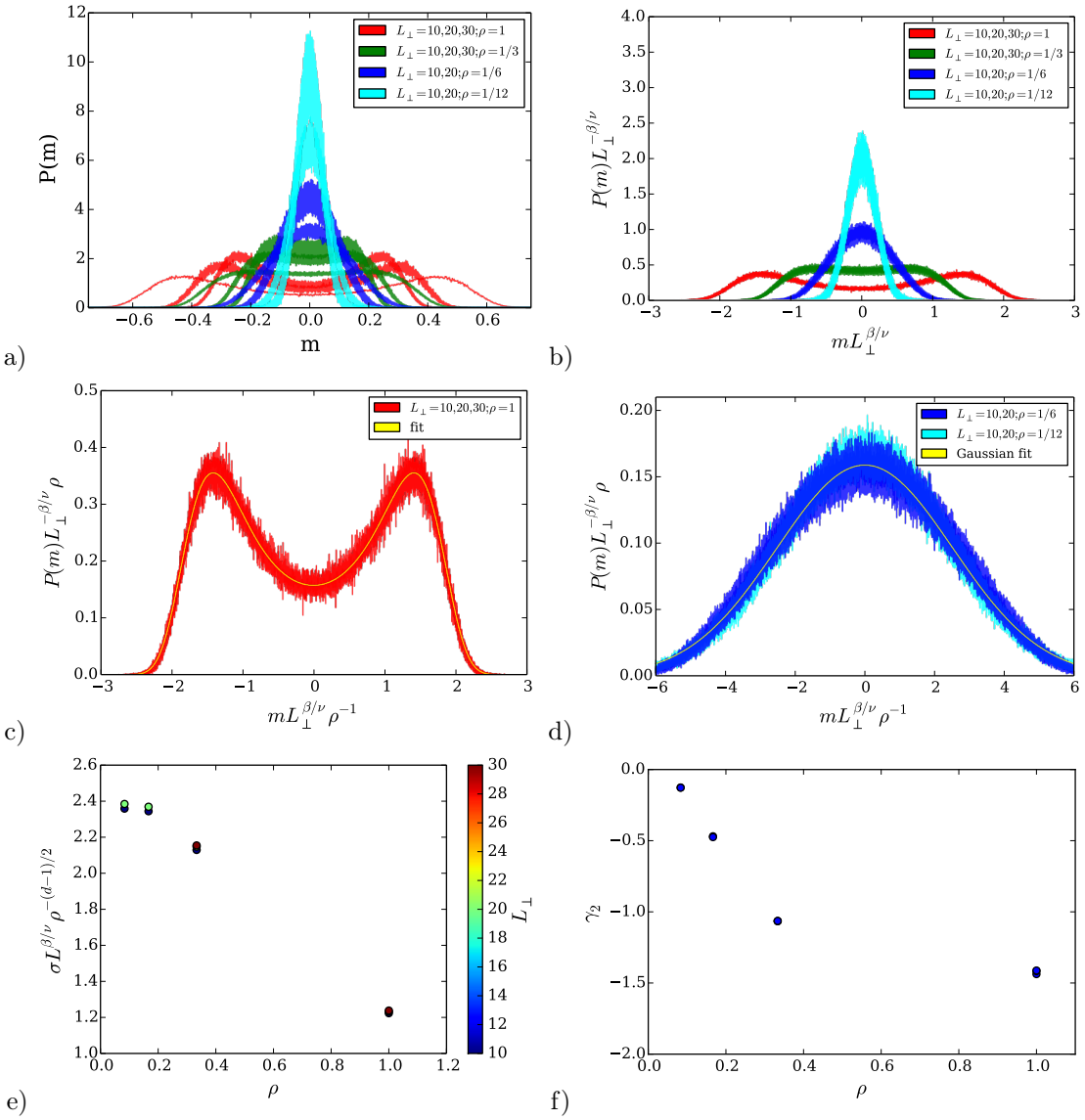

Figure 3.3: Results obtained by Monte-Carlo simulation of 3D Ising system with fully periodic boundary conditions, for various system thicknesses $L_\perp$ and aspect ratios ρ at the critical temperature $T = 4.5115 = T_c^{3D}$. **a)** Magnetization probability distribution $P(m)$ as a function of m. As the aspect ratio ρ is changed from 1 to 1/12 the distribution evolves from a bimodal to a monomodal functional form. **b)** $L_\perp^{-\beta/\nu}P$ as a function of $mL_\perp^{\beta/\nu}$. Distributions for system with similar aspect ratios collapse, but the functional form of the collapse depends on the aspect ratio. **c)** Particularizing distributions for the cubic case $\rho = 1$, we plot $L_\perp^{-\beta/\nu}P$ as a function of $mL_\perp^{\beta/\nu}$. We obtain an excellent collapse and the continuous line is a fit of an Ansätze proposed in ref. [60] (see main text). **d)** Particularizing monomodal distributions: $L^{-\beta/\nu}\rho^{(d-1)/2}P$ as a function of $mL_\perp^{\beta/\nu}\rho^{-(d-1)/2}$. The continuous line is Gaussian fit. **e)** $L_\perp^{-\beta/\nu}\rho\sigma$ tends to a saturation value $\hat{\sigma}$ as the slab limit $\rho \to 0$ is approached. **f)** Kurtosis γ_2 of all the distributions as a function of ρ.

3.5 Influence of fixed boundary conditions

3.5.1 Fixed $(+-)$ boundary conditions

The presence of fixed boundary conditions deeply affects the behavior of the system. Fixed anti-symmetric $(+-)$ BC in the confining direction act as local magnetic fields and put a topological constraint on the magnetization that induces a boundary between a positively and a negatively magnetized region. This is a different situation than a phase separation, induced by fixing the total magnetization, the fluctuations of the magnetization being less constrained by the $(+-)$ BC. From a universality class point of view, the situation with $(+-)$ BC is equivalent to the case of a critical binary polymer mixture of components A and B, confined between two plates, each preferentially adsorbing one of the components of the mixture. In that case, the plates would induce a phase boundary between a A rich phase and a B rich one. We therefore expect that the average magnetization of systems with $(+-)$ BC will fluctuate around 0 as a result of fluctuations of the phase interface. This is indeed the case as can be seen in figure 3.4a): the magnetization probability distribution remains monomodal at the critical temperature whatever the aspect ratio ρ, ranging from 1 to 1/9, and the system thickness $L_\perp$.

Plotting $L_\perp^{-\beta/\nu}\rho P$ as a function of $mL_\perp^{\beta/\nu}\rho^{-1}$, Fig. 3.4b), the scaling form of Eq.3.8 leads to a convincing collapse for systems with $L_\perp \geq 20$ and all the studied aspect ratios, the master curve being well fitted by a Gaussian of standard deviation $\hat{\sigma} = 0.43(4)$. The scaling functions obtained for thicknesses $L_\perp = 5, 10$ have a slightly bigger standard deviation, but as this discrepancy seems to be related to the small system thicknesses, we understand them as corrections to scaling, which are expected to be more prominent with $(+-)$ BC than periodic BC [3]. This assumption can be tested by looking at the evolution of $L_\perp^{\beta/\nu}\rho^{-1}\sigma$ with $L_\perp$, Fig. 3.4c). This reduced variance depends very little on ρ but strongly on $L_\perp$, so that, unlike the periodic boundary conditions case, the absence of collapse seems more likely to be related to corrections to the scaling limit rather than to the approach of the limit of slab geometry $\rho \to 0$. The evolution of the reduced standard deviation is well captured by a fit of the form

$$L_\perp^{\beta/\nu}\rho^{-1}\sigma = \hat{\sigma} + b_{eff}L_\perp^{-\omega_{eff}} \ , \tag{3.17}$$

where $b_{eff}, \omega_{eff}, \hat{\sigma}$ are fitting parameters for which we find $\omega_{eff} \approx 0.86$, $\hat{\sigma} \approx 0.35$ and $b_{eff} \approx 1.0$. This seems to be coherent with a correction to scaling, as ω_{eff} compares well with the exponent $\omega = 0.84(4)$ [4] controlling the leading correction to scaling in the Ising model (see Eq. 2.21 in the case of the susceptibility). A more thorough study of the impact of corrections to scaling on σ would be required to confirm this point.

The kurtosis, our test of normality in the case of symmetric distributions, is always rather small and goes to zero as $\rho \to 0$ (Fig.3.4d). Even for the smallest system $\rho = 1$ and $L_\perp = 5$, γ_2 is only ≈ 0.3, which is a kurtosis we would expect in a system of approximately $\rho \sim 1/10$ with periodic boundary conditions. Thus, we obtain much more easily a Gaussian form with

(+−) BC. Here, the physical origin of the monomodal distribution is different from the periodic boundary conditions case. The (+−) BC force the system to "demix" and the fluctuations of the order parameter come from the deformation of the interface between a + oriented region and a − oriented one. These boundary conditions can be seen as local magnetic fields of value $\pm J$ acting on boundary spins. If the value of this boundary field is lowered towards zero, below a certain value of the field we crossover towards another class of boundaries, the free boundaries (Dirichlet (O, O)). We expect the free boundaries case to be qualitatively similar to the fully periodic case at a temperature above T_c [50]. The limit case $L_\perp \to 1$ here is a 2D system without boundary field (the two + and − boundaries canceling each other) at high temperature as $T_c^{3D} > T_c^{2D}$, therefore conserving a monomodal distribution.

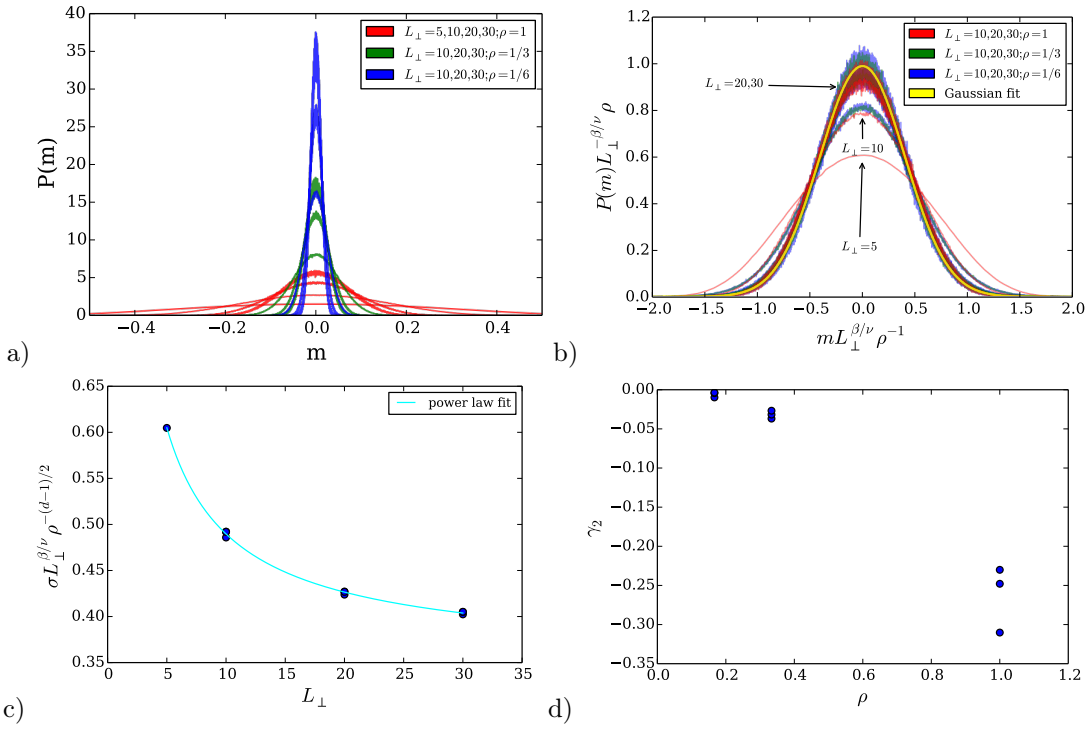

Figure 3.4: Results of Monte-Carlo simulation of 3D Ising systems with (+−) BC for various thicknesses $L_\perp$ and aspect ratios ρ at the critical temperature T_c^{3D}. **a)** Magnetization probability distribution $P(m)$. Whatever the aspect ratio, the distribution remains monomodal. **b)** $L_\perp^{-\beta/\nu}\rho P$ versus $mL_\perp^{\beta/\nu}\rho^{-1}$ for the same sizes as in a). We obtain a very convincing collapse of all data for thicknesses $L_\perp \geq 20$, whatever the aspect ratio. The scaling functions obtained for thicknesses $L_\perp = 5, 10$ have greater variances. The continuous line is a Gaussian fit of the distribution for the biggest available system. **c)** $L_\perp^{\beta/\nu}\rho^{-1}\sigma$ as a function of $L_\perp$. The continuous line is a power law fit of form $\hat{\sigma} + b_{eff} L_\perp^{-\omega_{eff}}$, intended as a guide to the eye. **d)** Kurtosis of all the distributions as a function of ρ. The kurtosis depends mainly on ρ and goes to zero in the slab limit $\rho \to 0$. It also depends in a less pronounced way on the confinement $L_\perp$, especially when $\rho = 1$.

3.5.2 Fixed (++) boundary conditions

With symmetry breaking (++) boundary conditions, the average magnetization $\langle m \rangle$ is no more expected to be zero, the total magnetic field imposed being non-zero. As can be seen in figure 3.5a) the magnetization probability distribution is monomodal but the position m_{max} of its maximum depends on the system size. The average magnetization $\langle m \rangle$ depends mainly on the thickness $L_\perp$ and only little on the aspect ratio as can be see in figure 3.5b).

With the boundary conditions breaking the symmetry, the kurtosis is no longer the lowest order moment quantifying a difference from the Gaussian behavior. A slight asymmetry can be

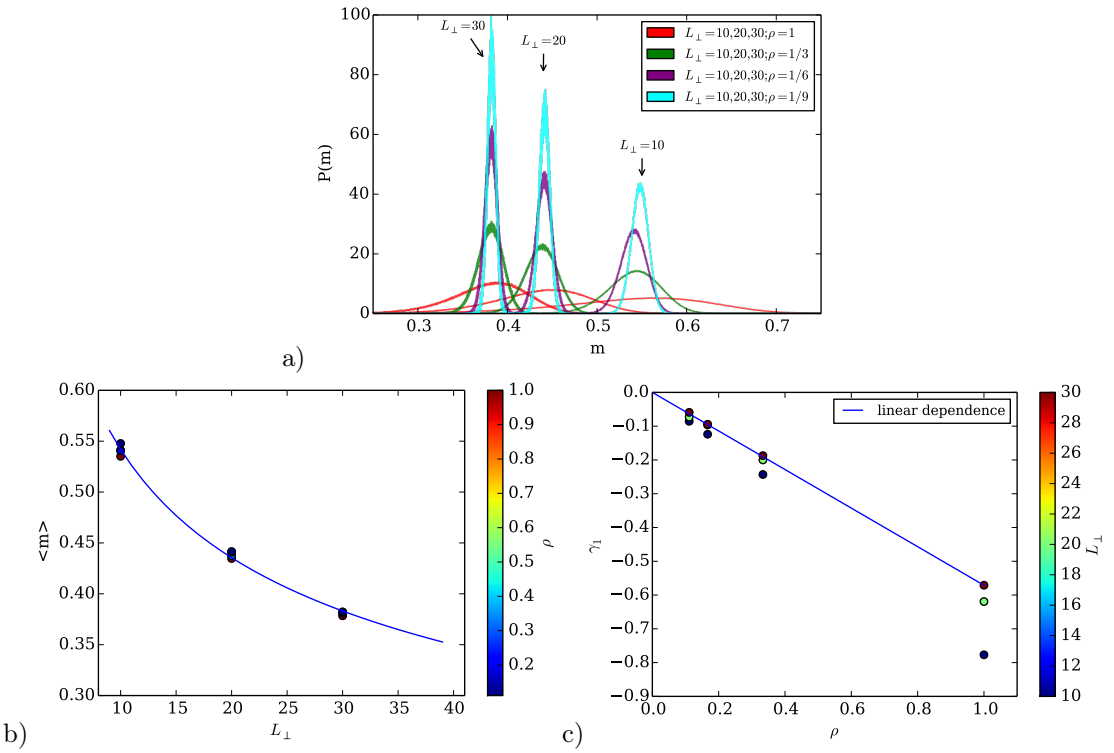

Figure 3.5: Results obtained by Monte-Carlo simulation of 3D Ising system with fixed (++) BC for various system thicknesses $L_\perp$ and aspect ratios ρ at the critical temperature $T = T_c^{3D}$. **a)** Magnetization probability distribution $P(m)$ as a function of m. The distribution is always monomodal, but the symmetry breaking boundary conditions impose a non-zero average magnetization. **b)** The mean magnetization decreases with increasing $L_\perp$ and slightly depends on ρ for the smallest system thickness $L_\perp = 10$. The continuous line is a power law fit intended as a guide to the eye. Points color give ρ. **c)** Asymmetry of the distributions can be highlighted by looking at the skewness γ_1. We find the main trend to be $\gamma_1 \propto \rho$, represented by the continuous line, fitted on the data for the largest thickness $L_\perp = 30$. Points color give $L_\perp$.

noticed in the distribution which can be quantified by looking at the skewness of the distribution:

$$\gamma_1 = \langle \left(\frac{m - \langle m \rangle}{\sigma} \right)^3 \rangle \ , \tag{3.18}$$

which strongly depends on the aspect ratio, Fig. 3.5c). For a given thickness, the dependency of γ_1 with ρ appears linear in the range investigated here, as the fit displayed fit in figure 3.5c) shows, based on the largest thickness $L_\perp = 30$. The skewness $\gamma_1 \to 0$ in the slab limit $\rho \to 0$. This limit can be understood by stating that when the limit $\rho \to 0$ is taken, the central-limit

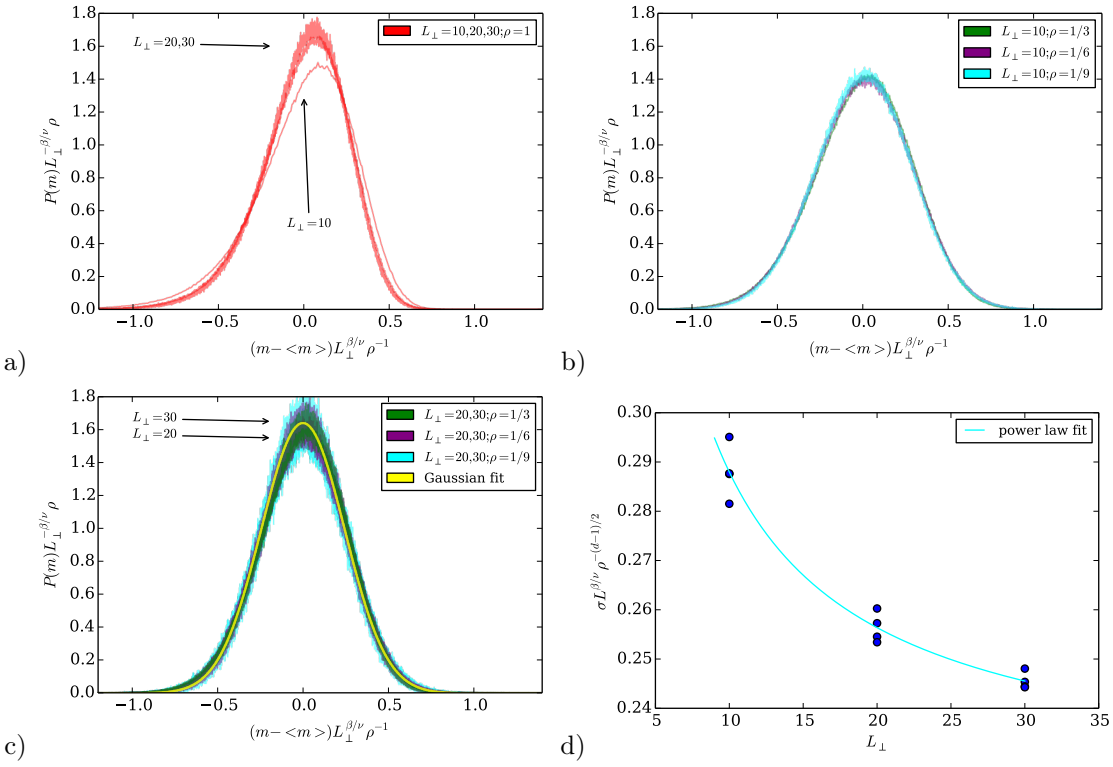

Figure 3.6: Results obtained by Monte-Carlo simulation of 3D Ising system with fixed (++) BC for various system thicknesses $L_\perp$ and aspect ratios ρ at the critical temperature $T = T_c^{3D}$. **a,b,c)** $L_\perp^{-\beta/\nu}\rho P(m - \langle m \rangle)$ versus $(m - \langle m \rangle)L_\perp^{\beta/\nu}\rho^{-1}$. For the sake of visibility, we have separated the most skewed distribution for $\rho = 1$ **(a)** and the smallest system thickness $L_\perp = 10$ for which the variance is notably different from larger system thickness **(b)**. For systems with $L_\perp \geq 20$ and $\rho < 1$, we obtain a convincing collapse within the current precision **(c)**. The continuous line is a Gaussian fit on data obtained with the largest system available. **d)** We can verify that the standard deviation follows Eq.3.7 by plotting σ as a function of $L_\perp^{-\beta/\nu}\rho$. The points for which this relation seems less verified are for the smallest system thickness $L_\perp = 10$, confirming previous observations. Points color give $L_\perp$. The continuous line is a linear evolution based on data for $L_\perp = 30$.

theorem can be applied on the uncorrelated sub-volumes (as discussed in section 3.1) and ensures that we tend to a symmetrical gaussian distribution. However, particularly for $\rho = 1$, γ_1 still noticeably depends on $L_\perp$, this effect decreasing as $\rho \to 0$.

We focus on the fluctuations of the magnetization around its mean value by centering the probability density and looking at $L_\perp^{-\beta/\nu}\rho P(m-\langle m\rangle)$ versus $(m-\langle m\rangle)L_\perp^{\beta/\nu}\rho^{-1}$, Fig. 3.6. For the sake of visibility, we have separated data for $\rho = 1$ (Fig. 3.6a). In this case, a significant skewness prevents the collapse with data for other values of ρ, but the amplitude and standard deviation of the distributions scale well with data for other system sizes. We also particularize data for the smallest system thickness $L_\perp = 10$ (Fig. 3.6b) for which the variance is notably different from larger system thickness. For systems with $L_\perp \geq 20$ and $\rho < 1$ (Fig. 3.6c), we obtain a convincing collapse within the current precision, which agrees well with a Gaussian behavior as shown by a Gaussian fit on data for the largest system available (giving $\hat{\sigma} = 0.25(1)$). The scaling of Eq.3.8 seems to be approached as $L_\perp$ grows. As for the case of fixed (++) boundaries, we present the evolution of the scaled standard deviation $L_\perp^{\beta/\nu}\rho^{-1}\sigma$ with $L_\perp$. As this quantity also depends on ρ, we only display a power law fit (Eq. 3.17) as a guide to the eye. We stress the fact that the effect of ρ on the reduced standard deviation $L_\perp^{\beta/\nu}\rho^{-1}\sigma$ diminishes with increasing $L_\perp$ and $L_\perp^{\beta/\nu}\rho^{-1}\sigma$ tends towards a non zero value, giving us confidence that the scaling of Eq.3.8 is approached.

3.6 Conclusion

In this chapter, we have seen how both the aspect ratio and boundary conditions of an Ising system influence the fluctuations of the order parameter at the critical temperature. We used simple arguments to propose a scaling form in the limit of slab geometry $L_\parallel \gg L_\perp$, in which case the probability density tends to a gaussian distribution in all studied cases. The data collapse was obtained by taking into account both the aspect ratio and the thickness $L_\perp$.

We have seen that in the case of fixed (+−) boundary conditions, the gaussian limit for fluctuations is much more easily reached. This is a consequence of the topological constraint imposed by the competing boundaries. The induced separation in positively and negatively oriented regions is related to the phenomenon of wetting [61, 62]. In a thermodynamically stable gaseous system, the presence of a surface can, by the action of attractive van der Waals forces, favor the condensation of the gas, forming a macroscopically thick wetting layer of liquid. In the Ising system, the + and − oriented phases can be interpreted as liquid and gas phases. A picture more closely related to wetting experiments than the symmetric (+−) case would be a semi-infinite Ising system with one fixed + boundary (respectively −) and a small bulk magnetic field $h < 0$ (resp. $h > 0$). In this case, the stable bulk phase is the negatively (reps. positively) oriented one but the presence of the boundary can induce a wetting transition at which a film of positively oriented spins (resp. negatively oriented) can develop from the boundary. In chapter 4,

we will see that wetting layers provide a experimental way to obtain a fluid system in slab geometry with small, controlled, thicknesses $L_\perp$. This allows for high precision measurements of the critical Casimir force, which will be the topic of the next chapter. The critical Casimir force is actually a consequence of the confinement of critical fluctuations. Thus, as we will show, the Casimir force being intimately related to the magnetic fluctuations, the boundary conditions will strongly influence the force, just as they influence the magnetic fluctuation spectrum.

Chapter 4

The Critical Casimir Force

4.1 Introduction to the critical Casimir force and experimental approaches

The origin of the critical Casimir force is in the confinement of critical fluctuations of a medium undergoing a continuous phase transition. The name "Casimir" comes from its quantum electrodynamics forerunner predicted by Hendrik Casimir in 1948 [14]. The now famous electrodynamic Casimir force occurs between two conducting and uncharged metallic plates in vacuum. As the plates put a constraint on the quantum fluctuations of the electromagnetic field, the imbalance between inside and outside the cavity of length L they form generates an attractive force of infinite range, decaying as L^{-4}. Its critical counterpart has been predicted by Fisher and de Gennes in 1978 [15]. In a confined critical system, the divergence of the correlation length is truncated by the finite size L of the system. The thermal fluctuations are thus constrained by the finite size of the system and, similarly to the electrodynamic case, this constraint results in a force. A simple way to comprehend this effect is to consider that when the correlation length develops up to the distance L separating the boundary conditions of the system, the boundaries interact through the correlated fluctuations.

Measurement of this effect requires high precision experiments. The first reason is that one must stabilize the system sufficiently close to its critical point to observe finite size effects, so that the correlation length develops up to the smallest system size. If, strictly speaking, a system is always finite, it is experimentally challenging to maintain a correlation length of the order of the micron, thus any larger systems can be considered infinitely large. For example, in a binary mixture of PMMA-3-octanone [63], the critical amplitude of the correlation length has been showed to be $\xi_0 \sim 0.97(2)\,\mathrm{nm}$ for a critical temperature $T_c \sim 306.58(4)\,\mathrm{K}$, so that stabilizing the reduced temperature at $t \sim 6.5 \times 10^{-5}$ and thus the correlation length at $\xi = \xi_0 t^{-\nu} = (6.5 \times 10^{-5})^{-0.6301} \times 0.97\,\mathrm{nm} \sim 0.4\,\mu\mathrm{m}$ requires a control on temperature of $\sim 0.02\,\mathrm{K}$. In ^4He, the critical end point at which the lambda line of normal/superfluid transitions meet

the liquid/gas line of phase transitions is located at $T_\lambda = T_c = 2.1786K$ [6] and the correlation length amplitude $\xi_0 = 0.1422(5)\,\mathrm{nm}$ [9]. Thus, if one achieves the same relative precision on temperature $t \sim 6.5 \times 10^{-5}$ as in our previous example, the correlation length can develop up to $\xi = \xi_0 t^{-\nu} = (6.5 \times 10^{-5})^{-0.67115} \times 0.1422\,\mathrm{nm} \sim 94\,\mathrm{nm}$. This actually compares well with the film thicknesses which were investigated in very succesful measurements of the Casimir force in ^4He, which ranged approximately from 20 nm to 34 nm [6, 64]. Another reason for the difficulty of measuring the Casimir force is its small amplitude: if one confines critical fluctuations that would occur at room temperature $T_{amb} \sim 300\,\mathrm{K}$ between two plates separated by $L \sim 1\,\mu\mathrm{m}$, the order of magnitude of the confinement force by unit surface is $\sim 4\,\mathrm{mN\,m^{-2}}$ [13]. Nonetheless, this effect should not be neglected: as we will see in the following, it can counterbalance other well known forces such as van der Waals interactions with a substrate or gravitational potential energy in wetting experiments. It can trigger colloidal self organizations [65, 66] and could have interesting applications in micro mechanical devices thanks to its great tunability [13] (see section 4.2.3). From this point of view, phase transitions in binary mixtures have the advantage of occurring at much higher temperature ($T_c \sim 306.58(4)\,\mathrm{K}$ in our example) than in superfluid systems such as ^4He ($T_c = 2.1786\,\mathrm{K}$), giving rise to a stronger effect.

The first direct measurements of the critical Casimir force were performed only recently in a binary mixture of water and lutidine [47, 67]. The confinement was performed by approaching a colloidal particle, immersed in the binary fluid and trapped by optical tweezers, close to a planar surface. Here, the confinement is in a sphere-plane geometry and not the plane-plane one that was already discussed in chapter 3. The plane-plane geometry is difficult to realize experimentally as the parallelism of confining plates has to be maintained. However, theoretical and numerical works directly tackling sphere-plane geometry [68, 69] are more rare than in the slab geometry. The slab geometry is the simplest confined geometry, clearly identifying a confining length, and the two geometries can be related by the Derjaguin approximation in the case of small confinement compared to the sphere curvature $R \gg L$ [47] or by the small sphere approximation in the opposing limit [69, 70]. Moreover, indirect measurements of the Casimir force in wetting layers make slab geometry experimentally relevant. A wetting layer can be formed (Fig.4.1) on a substrate, as a gas at a pressure and temperature close to their liquid-gas equilibrium values might condensate under the action of van der Waals interactions [13, 71, 72]. The interactions of the fluid particles with the substrate displaces the liquid-gas equilibrium point and the thickness of the layer is determined by the competition between van der Waals interactions favoring the condensation and other unfavorable interactions such as gravity [6, 64, 73] or a slight discrepancy between temperature of the substrate and the gas [5]. For example, in ref. [64], the wetting is formed on a pedestal placed at a height h above a bulk reservoir of ^4He, the principle of such an apparatus being sketched in figure 4.1d). The height h controls the equilibrium thickness L of the film, which results from the competition of a chemical potential contribution due to gravity and van der Waals interactions. If the fluid undergoes an internal continuous phase transition, such as a superfluid transition in wetting films of ^4He [64] or ^3He $-^4$ He mixture [6, 73], or

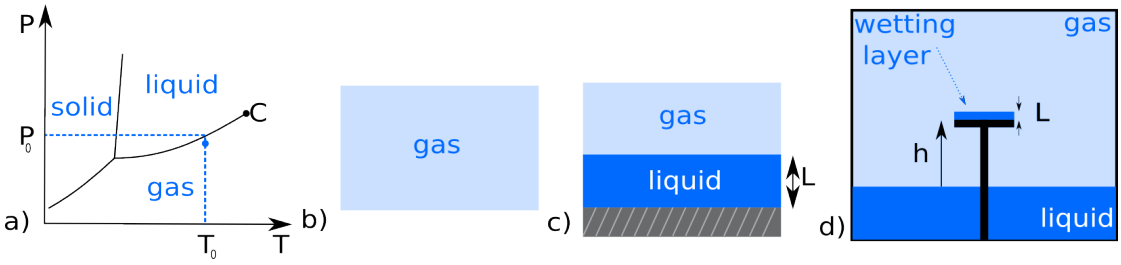

Figure 4.1: **a)** Schematic phase diagram of a fluid. A gas at pressure and temperature close to their liquid-gas equilibrium values (P_0, T_0) **(b)** will form a wetting layer **(c)** close to a wall due to van der Waals interactions with the substrate. Its thickness L diverging when getting towards (P_0, T_0). (Figures a, b, c, reproduced from ref. [13]). **d)** Sketch of an experimental cell to obtain a wetting layer of thickness L controlled by the height h of a pedestal above a liquid reservoir (see main text and ref. [64] for a more realistic sketch).

a demixing transition in a binary polymer mixtures [5, 74], the associated fluctuations will be confined between the liquid-substrate and liquid-gas boundaries. The Casimir force related to the internal transition will modify the equilibrium thickness of the film. Monitoring the wetting layer equilibrium thickness when approaching the critical or tricritical point of the internal phase transition yields an indirect measurement of the Casimir force in slab geometry. Consequently it appears natural to define the critical Casimir force through finite-size scaling of the free energy in slab geometry, as will be the topic of section 4.2. We stress on the fact that the forces responsible for the confinement of the system here are multiple, such as the van der Waals interaction and the critical Casimir force, and all have comparable amplitudes. We will comment again on the definition of a confinement force in chapter 7 in which we will encounter non critical confinement effects induced by the periodic boundary conditions.

Confinement of any correlated thermal fluctuations can result in Casimir-like effects. At a critical point however, as we have seen in the previous part, the correlation length diverges, making the critical Casimir effect both long ranged and universal. Thus, the critical Casimir force can be seen as a direct consequence of finite-size scaling and is characterized by a universal scaling function. Universality allows us to map experimental realizations onto much simpler models belonging to the same universality class. The superfluid transition belongs to the 3D XY universality class and the demixing of binary mixtures to the 3D Ising one. Both these models are consequently at the heart of numerous numerical and theoretical works on the Casimir force. We are particularly interested in the Ising universality class, as the Ising model is the simplest model of phase transitions, but the concepts we will develop are very general. In section 4.3, we will review some numerical approaches for computing the critical Casimir force in model systems and present in detail one method that we have reproduced in a 3D Ising system and which forms in part the basis of the magnetic method presented in chapter 5.

4.2 Finite-Size scaling and the critical Casimir force

4.2.1 Finite-size scaling of the free-energy in slab geometry

Let us consider a 3D critical system in slab geometry of size $L_\parallel \times L_\parallel \times L_\perp$ with $L_\perp \ll L_\parallel$ and $A = L_\parallel^2$, fig.4.2. We have already encountered this geometry in chapter 3: it allows one to clearly identify a confining dimension $L_\perp$ and is of great experimental relevance, as it maps to the set up of wetting experiments.

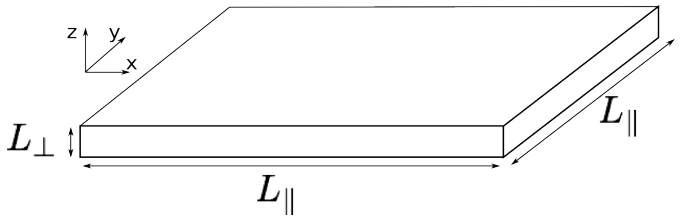

Figure 4.2: The slab geometry.

Near the bulk critical point where the bulk correlation length ξ becomes similar to the confining size $L_\perp$, the boundary conditions affect the spectrum of allowed fluctuations and the free-energy $\Omega(T, h, L_\perp, A)$ is no longer extensive. Here, the free energy only depends on the sizes of the system, temperature T and h which represents the field conjugate to the order parameter. For a magnetic system, h is proportional to the applied magnetic field. In a simple fluid near the liquid gas critical point $h \sim \mu - \mu_c$ is the chemical potential, measured with respect to the critical value μ_c, while near the demixing transition of a binary fluid, h depends on the difference in chemical potential of the two species. All these systems belong to the Ising universality class in which h is a scalar, but our analysis can easily be extended to include vector fields and order parameters, relevant for other universality classes such as the XY one, describing helium films near the superfluid transition.

Strictly speaking, thermodynamics require a fourth variable N, the number of particles, and hence a more general free energy $\Omega(T, h, L_\perp, A, N)$. We will develop our formalism in the case of a lattice model, particularizing the 3D Ising model on a cubic lattice, once again taking advantage of universality to conserve generality. The number of magnetic elements is therefore set by their density $n = \frac{N}{V} = \frac{1}{\sigma^3}$ where σ is the microscopic distance separating nearest neighbors, which is naturally fixed (for convenience, we can set $\sigma = 1$). The magnetic model thus becomes thermodynamically equivalent to a fluid system with fixed interaction range σ or, as we will see in more details in chapter 7, to a fluid binary mixture with fixed total density. In this case volume fluctuations impose fluctuations in the number of particles, so that one is dealing with a uniform medium. While spontaneous fluctuations of this kind clearly cannot exist in conventional magnetic systems [75], they do in fluid systems and allows us to discuss here the critical Casimir

force in full generality. This point will be further discussed in the following chapter.

The slab limit takes $L_\parallel$ very large, even with respect to the correlation length, so that an extensive behavior is conserved in the x and y directions (dependence on a finite aspect ratio $L_\perp/L_\parallel$ [75, 76] is not considered here). We can separate Ω in three different terms [23, 47, 77]. Two standard extensive contributions to the free-energy, defined in units of k_BT: a bulk term

$$\omega_{bulk}(T,h) = \lim_{L_\perp\to\infty}\lim_{A'\to\infty}\frac{\Omega(T,h,L_\perp,A')}{L_\perp A' k_B T} \ , \tag{4.1}$$

and a surface term

$$\omega_{surf}(T,h) = \lim_{L_\perp\to\infty}\left(\lim_{A'\to\infty}\frac{\Omega(T,h,L_\perp,A')}{A' k_B T} - L_\perp\omega_{bulk}(T,h)\right) \ . \tag{4.2}$$

describing surface tension at boundaries in the z direction. In the case of periodic boundary conditions, this term is of course zero. In the x, y directions transverse to the confining one, we will always assume that surface terms are negligible in the limit of slab geometry or implement periodic boundary conditions in simulations. Close to a critical point the free-energy acquires a new, non-trivial dependance on $L_\perp$ and thus we can give the complete decomposition of the free energy in the limit of slab geometry [47, 77]

$$\frac{\Omega_{slab}(T,h,L_\perp,A)}{Ak_BT} = \lim_{A\to\infty}\frac{\Omega(T,h,L_\perp,A)}{Ak_BT} = L_\perp\ \omega_{bulk}(T,h) + \omega_{surf}(T,h) + L_\perp\omega_{ex}(T,h,L_\perp) \ , \tag{4.3}$$

where ω_{ex} is the excess free energy due to the confinement of critical fluctuations, which therefore vanishes far from the critical point ($T = T_c, h = 0$) and in the thermodynamic limit $L_\perp \to \infty$. The excess part can be seen as an interaction term between the confining boundary conditions, the range of the interaction being proportional to ξ. It can also be related to the finite-size scaling hypothesis discussed in chapter 2, but in the special case of the slab geometry. In the thermodynamic limit the bulk term dominates, which the scaling hypothesis decomposes in an analytic and a singular terms

$$\omega_{bulk} = \omega_a(T,h) + \omega_s^0(t,\tilde{h}) \ , \tag{4.4}$$

where $\tilde{h} = h/k_BT_c$ and we have seen in chapter 2 that, for periodic boundary conditions, the excess term is a confinement contribution to the singular term

$$\omega_{ex} = \omega_s(t,\tilde{h},L_\perp) - \omega_s^0(t,\tilde{h}) \ , \tag{4.5}$$

where $\omega_s(t,\tilde{h},L_\perp) \underset{L_\perp\to\infty}{\to} \omega_s^0(t,\tilde{h})$. The excess free energy density thus will have a universal form which depends on the bulk universality class. In the case of non periodic boundary conditions, it also depends on the confining surfaces as they can deeply modify the form of the fluctuations, as we have seen in chapter 3, and the excess free energy depends on the surface universality class, as we will develop in section 4.2.3. The excess part of the free energy being fostered by the truncation of the diverging correlation length at a critical point, the relevant variable is the

ratio of the confining size $L_\perp$ and the correlation length $\xi(t,\tilde{h})$. Finite-size scaling then allows us to define a universal scaling function of the excess free energy (see section 2.2.1)

$$\omega_{ex}(t,\tilde{h},L_\perp) = L_\perp^{-d}\tilde{\Theta}\left(\mathrm{sgn}(t)\frac{L_\perp}{\xi_t},\frac{L_\perp}{\xi_h}\right) , \tag{4.6}$$

with d the spatial dimension, $\mathrm{sgn}(t)$ returns the sign of t as the function is not necessarily symmetric around T_c, and

$$\xi_t = \xi_0^+|t|^{-\nu} \ , \ \xi_h = \xi_0^h|\tilde{h}|^{-\nu/(\beta+\gamma)} \ , \tag{4.7}$$

are expressions of the correlation length ξ either above T_c at $h=0$ (ξ_t) or at $t=0$ for $h\neq 0$ (ξ_h), where critical exponents take their usual meaning [4, 23, 78]. $\xi_0^\pm$ and ξ_0^h are non-universal amplitudes of the correlation length. However, the ratio ξ_0^+/ξ_0^- is universal, so that either length scale can be used to define a scaling variable without losing universality. Often, the simpler scaling form

$$\omega_{ex}(t,\tilde{h},L_\perp) = L_\perp^{-d}\Theta\left(u_t,u_h\right) \ , \tag{4.8}$$

with the relevant scaling variables

$$u_t = tL_\perp^{1/\nu} \ , \ u_h = \tilde{h}L_\perp^{(\beta+\gamma)/\nu} \ , \tag{4.9}$$

is used, all length being dimensionless, measured in units of the microscopic length σ. One should nonetheless keep in mind that to compare different systems of a certain universality class, the universal form of Eq.4.6 has to be used, so that the change in the values of non universal amplitudes $\xi_0^\pm$ and ξ_0^h from a system to the other is taken into account.

4.2.2 The critical Casimir force

In equilibrium and in the anisotropic slab limit defined above, the confining force per unit area is defined

$$F_\perp = -\frac{1}{A}\frac{\partial\Omega_{slab}}{\partial L_\perp}\Big|_{T,h,A}, \tag{4.10}$$

which can be separated in a regular bulk pressure term and an anomalous term introduced by the restriction of the critical fluctuations

$$F_\perp = \underbrace{-k_BT\omega_{bulk}(T,h)}_{\text{bulk pressure in } z \text{ direction}} \underbrace{-k_BT\frac{\partial L_\perp\omega_{ex}}{\partial L_\perp}\Big|_{T,h}(T,h,L_\perp)}_{\text{critical Casimir force}} , \tag{4.11}$$

defining the critical Casimir force per unit area

$$f_c = -k_BT\frac{\partial(L_\perp\omega_{ex})}{\partial L_\perp}\Big|_{T,h} = -k_BT\left(\omega_s-\omega_s^0+L_\perp\frac{\partial\omega_s}{\partial L_\perp}\Big|_{T,h}\right) . \tag{4.12}$$

In fact, $L_\perp^{-1}$ plays an equivalent role in the criticality to reduced temperature and field, resulting in a third singular variable $Q = \frac{\partial V(\omega_s-\omega_s^0)}{\partial L_\perp^{-1}}$, in analogy with the magnetic moment $M = Vm$

and the entropy S. The Casimir force, $f_c = k_B T L_\perp^{-1}(Q/V)$, is the natural physical observable related to this thermodynamics for which one finds a universal scaling form [78]

$$f_c = k_B T L_\perp^{-d} \theta\left(u_t, u_h\right) \ , \tag{4.13}$$

from which we define Δ the universal scaling amplitude

$$\theta(0,0) = (d-1)\Delta \ . \tag{4.14}$$

Eq. (4.12) relates the Casimir force universal scaling function to that for the excess free energy Θ (Eq.4.8) by

$$\theta = (d-1)\Theta - \frac{u_t}{\nu}\frac{\partial\Theta}{\partial u_t}\Big|_{u_h} - \frac{u_h(\beta+\gamma)}{\nu}\frac{\partial\Theta}{\partial u_h}\Big|_{u_t} \ . \tag{4.15}$$

Hence, if one scaling function is known, the other can be deduced by solving Eq.4.15 (this will be further discussed in chapter 6). This relation relates the underlying universal scaling functions of the Casimir force f_c, the excess free energy f_{ex}, the internal excess energy u_{ex} and the excess order parameter m_{ex}

$$\frac{f_c}{k_B T} = (d-1)\omega_{ex} + t\nu^{-1}u_{ex} + \tilde{h}\frac{\beta+\gamma}{\nu}m_{ex} \ , \tag{4.16}$$

where

$$t u_{ex} = -tT\frac{\partial\omega_{ex}}{\partial T}\Big|_{h,L_\perp} = -L_\perp^{-d}u_t\frac{\partial\Theta}{\partial u_t}\Big|_{u_h}\frac{T}{T_c} \sim -L_\perp^{-d}u_t\frac{\partial\Theta}{\partial u_t}\Big|_{u_h} \ , \tag{4.17}$$

and where

$$\tilde{h}m_{ex} = -\tilde{h}\frac{\partial\omega_{ex}}{\partial\tilde{h}}\Big|_{T,L_\perp} = -L_\perp^{-d}u_h\frac{\partial\Theta}{\partial u_h}\Big|_{u_t} \ . \tag{4.18}$$

4.2.3 Importance of boundary conditions

The universal scaling form (Eq.4.13) of the Casimir force fully describes the phenomenon in all the experimental systems and models of a given universality class. However, this effect comes from the restriction of fluctuations by boundary conditions and is not a purely bulk phenomenon. Thus, the function θ depends both on the bulk universality class and on the surface universality class.

Various boundary conditions can be considered, either periodic, free or displaying a surface field coupled to the order parameter. The periodic boundary conditions, only relevant in simulations of course, are characterized by the absence of surface free energy, leaving only a bulk phenomenon. The free, or Dirichlet, boundary conditions are characterized by a lack of interactions at the boundary and correspond in a magnetic system to a boundary with a non-magnetic material and in general to a wall with no local influence on the order parameter. This corresponds to the ordinary (O) surface universality class [3, 58] with lower ordering at the surface than in the bulk. It is for example the relevant boundary condition for wetting experiments with a superfluid [6, 73], as the superfluid order parameter vanishes at the boundaries.

The addition of a strong boundary field corresponds to the normal or extraordinary surface universality class [58, 79], characterized by a higher ordering at the surface than in the bulk. For a magnetic system, this amounts to putting a magnetic field acting only on boundary spins, with the limit case of fixing the value of boundary spins to either positive (+) or negative (−) value. We use the convention that $L_\perp$ refers to the number of layers of fluctuating spins, whatever the boundary conditions [57–59]. In the case of a binary fluid, this is equivalent to having walls which preferentially adsorbs one of its two components. In the first direct measurements of the critical Casimir force, performed in a binary mixture of water and lutidine [47, 67], surface treatment allowed for the investigation of both symmetric $(++), (--)$, and antisymmetric $(+-)$ boundary conditions, showing direct experimental evidence that the Casimir force changed from attractive for symmetric boundaries to repulsive for antisymmetric ones (Fig.4.6).

Consequently, surface treatment and patterning has been of great interest as a way of tuning the Casimir force [80–86]. In the case of boundary conditions weakly coupled to the order parameter (weakly adsorbing walls for binary mixture or weak boundary magnetic fields for magnetic systems), crossover situations occur between $+, O$ and $-$ boundary conditions [58, 87–89] and, for example, weak asymmetric boundary conditions of different strength can be set so that the sign of the Casimir force in the Ising 3D universality class changes with temperature [87].

More complex boundary conditions than flat uniform walls have been explored. Crenellated boundary conditions [81] have recently been considered theoretically and in the case of walls structured by periodic arrays of wedges and ridges [84] mean-field approaches predict not only a Casimir force acting normally on the confining walls but also transversally. The substrate can also be flat but chemically structured [90, 91]. Structuring with alternating + and − stripes can foster a lateral Casimir force in binary mixtures [92] and trigger the organization of colloids along the strips when immersed in the critical binary fluid close to the structured substrate [93]. The effective potential felt by the colloids is well described by the Casimir force [83, 94], thanks to the Derjaguin approximation applied to the Casimir scaling function obtained in plane-plane geometry [3]. For certain dimensions of the substrate's structures, a colloid is expected to undergo a critical Casimir force of changing sign with distance. A "levitation" distance exists which can be made stable with respect to thermal fluctuations and be tuned by the temperature [82]. In the limit case of very narrow stripes, the structured boundary conditions can even mimic the O boundary conditions [80]. This has recently also been attained with a surface with fixed + or − spins randomly distributed, with resulting surface field of zero mean [95]. Disorder introduced through random surface fields distributed according to a Gaussian distribution with vanishing mean have been showed to increase the Casimir force compared to the O boundary case [96].

Thus, the great variety of behaviors of the critical Casimir force, allowed by various boundary conditions, make it a promising candidate for technological applications in micro and nano-mechanical devices, where it could counterbalance the electrodynamic Casimir force which is responsible for collapse of the structures [13].

4.2.4 Limit behavior

The critical Casimir force comes from the confinement $L_\perp$ and by the divergence of the correlation length, itself governed by t and $\tilde{h}$, so we expect the limit behaviors in the Ising universality class

$$\begin{cases} \theta(u_t, u_h) \underset{u_t \to \infty}{\to} 0 \ , \\ \theta(u_t, u_h) \underset{u_h \to \infty}{\to} 0 \ . \end{cases} \tag{4.19}$$

Far from the critical point, θ for a confinement between two planar walls is expected to decay exponentially fast, following the analytic form

$$\theta(u_t) \underset{|u_t| \to \infty}{\to} A_0 |u_t|^{\nu d} \exp(-U_0 |u_t|^\nu) \ , \tag{4.20}$$

in the Ising model for $d = 2, 4$ and $(+, \pm)$ boundaries [83], for $d = 3$ and $(+-)$ boundary conditions at $T > T_c$ and for $(++)$ boundaries for T both above and below T_c [57, 77, 97].

In the case of the XY universality class though, the presence of Goldstone modes make the correlation length infinite even at low temperature: ξ_0^- is not defined and the θ function tends to a non-zero constant value at low temperature.

4.3 Numerical computation of the Casimir force : example of the coupling parameter approach

4.3.1 Introduction on numerical computations of the Casimir force

Numerical simulation is an ubiquitous way of computing the universal scaling function θ as it allows the study of various geometries and boundary conditions. To study liquid-gas criticality or critical binary mixtures, molecular simulations of Lennard-Jones systems can be thought as a way to mimic wetting experiments [62] or to measure directly a Casimir contribution to the pressure in confining geometries (this will be the topic of chapter 7). However, critical simulations of fluids are very challenging and, as far as we know, reference [62] has been the only attempt to capture a Casimir effect in this way. Therefore, universality has fully been exploited and model magnetic systems have been favored in numerical computation of the critical Casimir force.

A direct way to obtain the Casimir contribution to the confinement pressure in magnetic models such as the Ising, XY and Heisenberg models, is to construct a lattice stress tensor, which can be computed through Monte Carlo simulation [21, 77], but has only been exploited with fully periodic boundary conditions. Such a stress tensor had been used in other models analytically [20, 21] and has very recently been used for mean field calculations [81, 84].

However, a now ubiquitous approach to computing the critical Casimir force relies on the fact that, as we have seen in the previous section, the Casimir force is defined as the excess

contribution to the derivative of the free energy (Eq.4.10). Therefore, computing the free energy of a system or at least its variation with respect to system size can give access to the pressure from which one can extract the excess part if sufficient accuracy is reached. A text book approach to computing the free energy [2] uses the basic relation $\Omega = U - TS - Mh$, where U and S are the internal energy and entropy of the system. Monte-Carlo simulations give direct access to U and M and we can compute the entropy by a suitable integration of the measurable specific heat $C_V = T\frac{\partial S}{\partial T}\Big|_{V,h}$. Experimentally, the internal energy is not accessible, only the specific heat is. So, this methods needs another integration of C_V to extract Ω. Both in experiments and simulations, this method suffers from the great difficulty of accurately measuring C_V close to a critical point [9].

In numerical simulations, the value of all microscopic degrees of freedom being accessible, the number of numerical "observables" is much bigger than in experiments. If one can define a crossover Hamiltonian continuously interpolating between two different systems, one can compute the variation in free energy between them and it is therefore possible to design a simulation specifically for measuring the variation of free energy with respect to a change in system size [3, 98–101]. This very general approach is referred to as "thermodynamic integration" or "coupling parameter" approach. We will now present such a method which proved very efficient for computing the critical Casimir force and can be used in a very wide range of lattice systems and boundary conditions. We have reproduced some results of ref. [3] in the 3D Ising model with fully periodic boundary conditions. We present these results in some details as they form in part the basis of the magnetic method presented in chapter 5.

4.3.2 Crossover Hamiltonian

Following [3, 101] (see also [87, 100]) we calculated f_c for a 3D Ising model with a cubic lattice in film geometry. The present approach is to compute the variation in free energy caused by a change in system size, approximating the derivative of the free-energy with respect to system size $L_\perp$, which contains f_c the critical Casimir force. The idea is to define a crossover Hamiltonian which continuously interpolates between a $L_\perp$ layer thick system to a $L_\perp - 1$ layer thick one

$$\mathscr{H}_{cr}(\lambda) = (1-\lambda)\mathscr{H}_0 + \lambda\mathscr{H}_1 \ , \tag{4.21}$$

where $\mathscr{H}_0$ is the Hamiltonian of a $L_\perp$ layers system and $\mathscr{H}_1$ of a $L_\perp - 1$ layers one plus one decoupled layer, as schematized in figure 4.3. In the crossover system, if $\lambda = 0$, we have a regular 3D Ising system on a cubic lattice of size $L_\perp \times L_\parallel \times L_\parallel$. As $\lambda \to 1$, the spins of a layer k_0 (chosen far from the boundary conditions if they are not periodic) are continuously decoupled from their nearest neighbor in the z direction, while spins of layers k_0+1 and k_0-1 are coupled, all couplings in x and y directions remaining unchanged. This results in the decoupling of a 2D layer upon changing $\lambda \to 1$, until obtaining a $(L_\perp - 1) \times L_\parallel \times L_\parallel$ system plus a 2D decoupled layer.

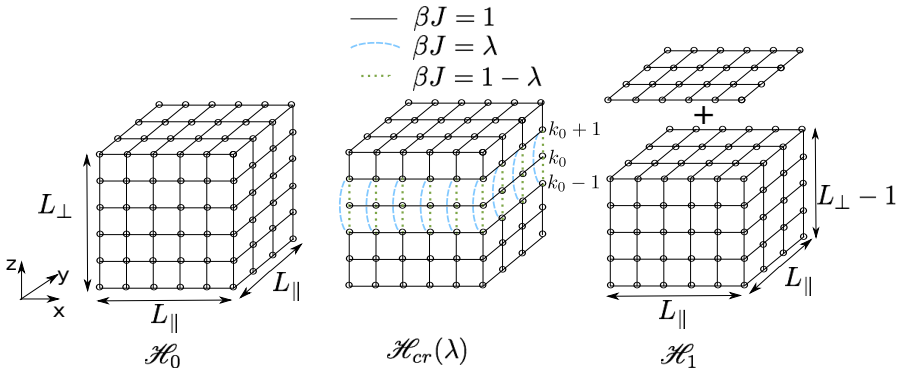

Figure 4.3: Definition of the crossover Hamiltonian $\mathscr{H}_{cr}(\lambda)$. With λ going from 0 to 1, the layer labeled k_0 is decoupled from the rest of the system and layer $k_0 + 1$ coupled to $k_0 - 1$. (Figure reproduced from ref. [3])

4.3.3 Computing the change in free energy with system thickness

The free energy of the cross-over Hamiltonian, for a given value of the parameter λ, is

$$\Omega_{cr}(\lambda) = -k_B T \ln \left(\sum_{\{S_i\}} \exp(-\varkappa \mathscr{H}_{cr}(\lambda)) \right) , \tag{4.22}$$

where $\sum_{\{S_i\}}$ means a sum over the phase space and $\varkappa = 1/k_B T$. So, we notice that the derivative of the free energy with respect to the crossover parameter

$$\frac{d\Omega_{cr}(\lambda)}{d\lambda} = \frac{\sum_{\{S_i\}} (\mathscr{H}_1 - \mathscr{H}_0) e^{-\varkappa \mathscr{H}_{cr}(\lambda)}}{\sum_{\{S_i\}} e^{\mathscr{H}_{cr}(\lambda)}} = \langle \mathscr{H}_1 - \mathscr{H}_0 \rangle_{\mathscr{H}_{cr}(\lambda)} , \tag{4.23}$$

with $\langle . \rangle_{\mathscr{H}_{cr}(\lambda)}$ a statistical average performed in the crossover system. This average can be efficiently computed using Monte Carlo simulation and amounts to computing the average of the quantity

$$\mathscr{H}_1 - \mathscr{H}_0 = -\sum_{x,y} S_{x,y,k_0+1} S_{x,y,k_0-1} - S_{x,y,k_0} S_{x,y,k_0+1} - S_{x,y,k_0-1} S_{x,y,k_0} . \tag{4.24}$$

Then, if we calculate this quantity for different values of λ, an integration over the crossover parameter give access to the difference in free energy

$$\Omega_{1-0} = \int_0^1 d\lambda \, \langle \mathscr{H}_1 - \mathscr{H}_0 \rangle_{\mathscr{H}_{cr}(\lambda)} = \Omega_1 - \Omega_0 , \tag{4.25}$$

between the $\{L_\perp$ layers$\}$ and $\{L_\perp - 1$ layers $+ 1$ layer$\}$ systems, which we can decompose using the formalism of Eq.4.3

$$\Omega_{1-0} = \Omega_{slab}(T, h, L_\perp - 1, A) - \Omega_{slab}(T, h, L_\perp, A) + \Omega_{2D}(T, h, A) , \tag{4.26}$$

with $\Omega_{2D}(T, A)$ the free energy of the decoupled layer, and $A = L_\parallel^2$. If the system is sufficiently thick to consider that a variation of one layer is infinitesimal ($L_\perp \gg 1$), we are estimating the derivative of the free energy Ω_{slab}

$$\Omega_{1-0}(T, h, \ell, A) \underset{L_\perp \gg 1}{\approx} \underbrace{-\frac{\partial \Omega_{slab}}{\partial L_\perp}\Big|_{T,h,A}(T, h, \ell, A)}_{\text{bulk pressure} + A f_c} + \Omega_{2D}(T, h, A) \ , \tag{4.27}$$

evaluated at $\ell = L_\perp - 1/2$, which therefore contains the critical Casimir force according to Eq.4.10,4.11. The intuitive choice $\ell = L_\perp - 1/2$ has been shown rigorously to facilitate the approach to the scaling limit by minimizing the importance of corrections to scaling terms [75].

4.3.4 Extracting an excess contribution

Surface terms have been suppressed by the derivation as they do not depend on $L_\perp$. We are only interested in the Casimir contribution, so we also need to get rid of the 2D and 3D bulk contributions. This can be done by taking advantage of the extensivity of the bulk 3D contribution and of the independence of the 2D term on ℓ. Thus, we repeate the procedure for two sets of length scales centered on ℓ and $\alpha\ell$, all other parameters remaining equal. Subtracting results from the two pairs of length scales eliminates the free energy from 2D layer and the bulk contribution,

$$\Omega_{1-0}(T, h, \alpha\ell, A) - \Omega_{1-0}(T, h, \ell, A) \approx A f_c(T, h, \alpha\ell) - A f_c(T, h, \ell) \ , \tag{4.28}$$

providing a first estimate of the Casimir force

$$f_c^0(T, h, \ell) \approx f_c(T, \ell) - f_c(T, h, \alpha\ell) \ . \tag{4.29}$$

Given the universal scaling form of f_c (Eq. 4.13), one can define a scaling function for f_c^0

$$f_c^0(T, h, \ell) = k_B T \ell^{-d} \theta^0 \left(u_t[\ell], u_h[\ell]\right) \ . \tag{4.30}$$

related to θ at two different values of u_t and u_h by :

$$\theta^0(\ell) = \theta(\ell) - \alpha^{-d}\theta(\alpha\ell). \tag{4.31}$$

Provided that at a given temperature and field the Casimir effect decreases with increasing system size, if $\alpha > 1$, $\alpha^{-d} < 1$ and $\theta(\alpha\ell) < \theta(\ell)$. Choosing $\alpha^{-d} \ll 1$, the scaling function θ^0 will provide a good estimate for the functional form of $\theta(u_t, u_h)$ as $\theta(\alpha\ell) \ll \theta(\ell)$ and α^{-d} is a small parameter, the system of size $\alpha\ell$ acting as a reference system, large enough to be considered at the thermodynamic limit. This is of course a difficult limit to reach in a simulation but, thankfully, there exists another way of improving the estimate of θ from θ^0.

4.3.5 Iteration procedure

To extract a complete estimate of θ from the measured quantity θ^0, one can apply the procedure developed in ref. [3] to solve Eq.4.31 iteratively. Here is presented an extended version of this procedure to include a non zero field h. We rewrite Eq.4.31 in the form

$$\theta(\ell) = \theta^0(\ell) + \alpha^{-d}\theta(\alpha\ell) \ , \tag{4.32}$$

clearly showing that, as we already mentioned, if α is chosen greater than 1, we can consider, as a first approximation to the function $\theta(u_t, u_h)$:

$$\theta^0(u_t, u_h) \approx \theta(u_t, u_h) \ . \tag{4.33}$$

It seems fairly logical to consider that an improved estimate θ^1 of θ will then be given by

$$\theta^1(\ell) = \theta^0(\ell) + \alpha^{-d}\theta^0(\alpha\ell) \ , \tag{4.34}$$

considering the form of Eq.4.32. Using Eq.4.31 and 4.34 to express θ^1 as a function of θ, we can move to higher order approximations of $\theta(u_t, u_h)$. This leads to defining the following recursion relation

$$\theta^{n\geq 1}(u_t, u_h) = \theta^{n-1}(u_t, u_h) + \alpha^{-2^{n-1}d}\theta^{n-1}(\alpha^{2^{n-1}/\nu}u_t, \alpha^{2^{n-1}(\beta+\gamma)/\nu}u_h) \ . \tag{4.35}$$

This relation can be rewritten as a recursion procedure on the function $\theta^0(u_t, u_h)$ only, which converges towards

$$\begin{aligned} \lim_{n\to\infty} \theta^n(u_t, u_h) &\equiv \hat{\theta}(u_t, u_h) \\ &= \sum_{n=0}^{\infty} \alpha^{-dn}\theta^0(\alpha^{n/\nu}u_t, \alpha^{n(\beta+\gamma)/\nu}u_h) \ . \end{aligned} \tag{4.36}$$

The series defining $\hat{\theta}(u_t, u_h)$ converges because α^{-dn} decays exponentially fast with n and $\theta^0(u_t, u_h)$ is expected to be bounded, having a finite maximum close to the critical point and decaying exponentially quickly for $u_t, u_h \to \pm\infty$. By injecting the expression of function $\hat{\theta}(u_t, u_h)$ into Eq.4.31, or equivalently Eq.4.32, we see that it is indeed a solution to the equation. The function $\theta(u_t, u_h)$ can therefore be estimated using an approximation $\theta^n(u_t, u_h)$ obtained after a finite number of iterations.

For a typical value $\alpha = 2$, this iteration procedure converges rather quickly in three dimensions. For the third iteration $n = 3$, we already get : $\alpha^{-2^{n-1}d} \sim 10^{-4}$, $\alpha^{2^{n-1}/\nu} \sim 10^2$, $\alpha^{2^{n-1}(\beta+\gamma)/\nu} \sim 10^3$. The correction given by this third iteration is therefore expected to be small given the very small value of the parameter $\alpha^{2^{n-1}}$ and that the point $(\alpha^{2^{n-1}/\nu}u_t, \alpha^{2^{n-1}(\beta+\gamma)/\nu}u_h)$ reached will be far from the critical point, except for extremely small values of (u_t, u_h).

Note that, to obtain θ over a given range of u_t and u_h, using this recursion requires that the function θ^0 is measured over a much wider range, since each iteration dilutes the chosen window.

The iterative procedure requires access to increasingly high values $(\alpha^{n/\nu}u_t, \alpha^{n(\beta+\gamma)/\nu}u_h)$ of the scaling parameters, eventually falling outside the range of values for (u_t, u_h) explored in the simulation. We have only considered the case $h = 0$ and are only concerned by the variable u_t. To estimate θ^0 for values outside the range of u_t explored in the simulation, we have fitted the function θ^0 using an exponential ansätze of the form of Eq.4.20, which proved excellent.

Further, the procedure requires the use of values for $\theta^0(u_t, u_h)$ over the continuous range of variables (u_t, u_h), not just the discrete set used in a Monte Carlo simulation. These values can be estimated using spline interpolation of the computed values of θ^0. In practice we have chosen $\alpha \approx 2$, and have never used more than 2 iterations to obtain an estimate of θ in all the work presented in this thesis.

4.3.6 Simulation and results

We performed Monte Carlo simulations in order to accurately reproduce the results of ref. [3], where only the case of $h = 0$ has been considered (the effect of a magnetic field will be studied in chapter 5). We restrained ourselves to a 3D system with periodic boundary conditions in all three directions. Both the Wolff cluster algorithm and Metropolis algorithm (see chapter 2) were used in a hybrid Monte Carlo step composed of a Wolff step on the entire system followed by Metropolis iterations in layers $\{k_0 - 1, k_0, k_0 + 1\}$. For each temperature, 20 Monte Carlo simulations with different values of λ ranging from 0 to 1 were performed to allow for the integration of Eq.4.25, performed using the quadratic Simpson's rule.

In figure 4.4 are presented the function $\theta^0(u_t, 0)$ obtained for $(\ell = 9.5, \alpha\ell = 19.5, A = 60^2)$ and θ^2, an improved estimate of θ thanks to the iterative procedure of Eq.4.35, which converged within our present precision after two iterations. θ^0 and θ^2 are asymmetric and exponentially decays to zero far from the critical point, showing that it is a purely critical phenomenon. The scaling function is always negative, yielding an attractive Casimir force.

The main effect of the iterative process is to suppress the "shoulder" that is visible close to $u_t = 0$ in θ^0. This "shoulder" is the signature of the influence on function θ^0 of the Casimir force computed in the system of size $\alpha\ell$, as θ^0 can be seen as the scaling function of the difference between the Casimir force in the system of size ℓ minus the Casimir force computed in the system of size $\alpha\ell$ (Eq.4.29), which is of smaller amplitude and width.

Approximately 10^6 Monte Carlo steps were required to get the most accurate data presented. The choice of system sizes allow us to directly compare the function $\theta^0(u_t, 0)$ that we computed to the one presented for the same parameters in ref. [3], showing excellent agreement (Fig.4.4). This choice was primally motivated by several constraints: the width $L_\parallel$ has to be taken as large as possible to approach slab geometry (an aspect ratio $L_\perp/L_\parallel = 1/6$ has been showed in ref. [76] to already provide a good approximation of this limit). System thicknesses ℓ and $\alpha\ell$ should be as large as possible to ensure that the approximation of Eq.4.27 is valid and that we reached

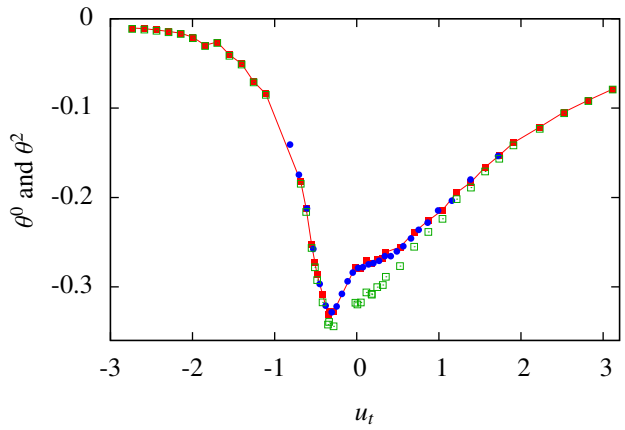

Figure 4.4: $\theta^0(u_t, 0)$ (red filled squares) obtained with $(\ell = 9.5, \alpha\ell = 19.5, A = 60^2)$ and the same function obtained for the same lattice sizes in ref. [3] (blue dots), showing very good agreement. Within our present precision, the iterative procedure of Eq.4.35 converged after two iterations, providing a better estimate $\theta^2(u_t, 0)$ (green open squares). Error bars are of the order or smaller than points size.

the scaling limit. Of course, a compromise has to be found as the computation time increases rapidly with increasing system size.

The fully periodic boundary conditions cannot be related to any experimental situation. But, as we have been able to reproduce to an excellent level of agreement results of reference [3] (Fig.4.4), we have not pursued any further the reproduction of the data and will rely on results presented in this reference paper for other surface boundary conditions. Nevertheless, before presenting experimentally relevant results, we must consider the influence of corrections to scaling.

4.3.7 Corrections to scaling

In chapters 1 and 2, we have seen that scaling behavior is only dominant close enough to the critical point [23]. In section 1.3.6, we gave the example of corrections to scaling in the thermodynamic limit of the susceptibility

$$\chi(T, h = 0) = |t|^{-\gamma}(A_\pm + B_\pm \tilde{K}_3 t^{-\nu y_3} + \dots) \ , \tag{4.37}$$

with $A_\pm, B_\pm$ non-universal amplitudes, so that the power law $|t|^{-\gamma}$ is indeed the dominant behavior close to T_c but $t^{-\nu y_3}$ might be important to take into account if one wants to extract critical exponents from measurements. In section 2.2.3, we extended this example to the case of corrections to finite-size scaling, in the case of the evolution of the amplitude at $(t, h) = (0, 0)$ of

the susceptibility

$$\chi(T_c, h = 0, L) = L^{2-\eta}\chi_s(0,0)(1 + b_1 L^{-\omega} + \dots) + \chi_a \ , \tag{4.38}$$

with χ_a an analytic background and b_1 a non universal amplitude to the leading correction to scaling $L^{-\omega}$ ($\omega = 0.84(4)$ in the Ising model [4]). In numerical simulations, corrections to finite-size scaling have often to be taken into account as the size of systems are limited by computers and algorithms capacities.

To get rid of these corrections, one must perform simulations in large enough systems, as allowed by the limitations of simulations techniques, or reach sufficient accuracy to disentangle universal behaviors from non universal corrections. Another possibility is to find models belonging to the universality class of interest in which the leading correction to scaling is suppressed [4]. This is the case of the Blume-Capel model of Hamiltonian

$$\mathscr{H}_{BC} = -\sum_{<i,j>} S_i S_j + k_B T D \sum_i S_i^2 \ , \tag{4.39}$$

where spins assume values $S_i \in \{-1, 0, 1\}$ and D is a parameter controlling the density of vacancies $S_i = 0$ [57, 59, 102]. For $-\infty < D < D_{tri}$ the model undergoes a continuous phase transition at a critical temperature $T_c^{BC}(D)$, belonging to the Ising universality class (actually, in the limit $D \to -\infty$ the model becomes equivalent to the Ising model). Numerically, it has been shown that there exist a point D^* at which the amplitude of the leading correction to scaling vanishes. One difficulty with this improved Hamiltonian approach is that it requires a precise estimate of the parameter value at which the leading correction is reduced, D^* in the Blume-Capel model, while observables are still subject to higher order corrections to scaling. Nevertheless, the Blume-Capel has been shown to give high accuracy measurements of the critical Casimir force [57, 59, 102]. Improved models are more delicate to implement than simpler models such as the Ising model itself. The simplicity and flexibility of the latter and the abundant literature on its numerical resolution at criticality still makes it today a suitable choice for the study of the critical Casimir force [96].

As for any other observable, corrections to scaling affect the critical Casimir force. Estimates of the scaling function θ obtained with different sets of systems size $L_\perp$ or $L_\parallel$ will differ if the system sizes are not large enough. Reference [3] gives a detailed discussion of corrections to scaling affecting θ in the 3D Ising and XY models for various boundary conditions. Firstly, the scaling behavior of the correlation length is affected by corrections to scaling: this effect can be captured by replacing the scaling variable $t(L_\perp/\xi_0^+)^{1/\nu}$ by a corrected one $x(t, L_\perp)$. Both the finite thickness $L_\perp$, which might be too small to be in the scaling limit, and the finite aspect ratio $\rho = L_\perp/L_\parallel$, which make the limit of slab geometry only approximate, can foster corrections to scaling. In ref. [3], for periodic boundary conditions in the Ising model, corrections of the form

$$x = t(L_\perp/\xi_0^+)^{1/\nu}(1 + g_\omega L_\perp^{-\omega})(1 + r_1\rho^2) \ , \tag{4.40}$$

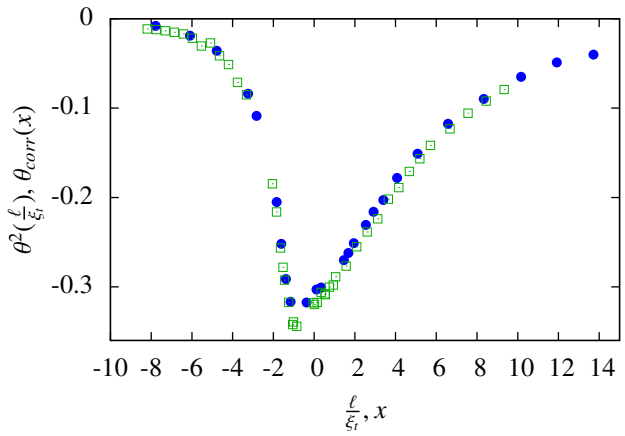

Figure 4.5: Effect of corrections to scaling computed in ref. [3]. We display our result for $\theta^2(\frac{\ell}{\xi_t})$ (green open squares), obtained with ($\ell = 9.5, \alpha\ell = 19.5, A = 60^2$) and already presented in Fig.4.4, as a function of the universal scaling variable $\frac{\ell}{\xi_t}$, with $\xi_t = \xi_0^+ |t|^{-\nu}$. We compare it to the the function $\theta_{corr}(x)$ (blue dots) obtained in ref. [3] for the same system sizes but taking corrections to scaling into account, affecting both the amplitude of the function θ_{corr} and the scaling variable x (see main text). Error bars are smaller than points size.

were used, where g_ω and r_1 are non-universal amplitudes and $\omega = 0.84(4)$ is the universal exponent for leading corrections to scaling. It turns out that for the investigated system sizes in ref. [3], $g_\omega \approx r_1 \approx 0$ already provided a data collapse. Secondly, the amplitude of the Casimir force is also affected by corrections to scaling and in ref. [3], for periodic boundary conditions in the Ising model, corrections of the form

$$\theta_{corr}(x) = (1 + g_2 L_\perp^{-\omega_{eff}})\hat{\theta}(x) \ , \tag{4.41}$$

were used, with $\hat{\theta}$ the estimate of the scaling function after employing the iterative procedure described above and g_2 and ω_{eff} fitting parameters to obtain the best data collapse.

We compare in figure 4.5 the estimate $\theta^2(\frac{\ell}{\xi_t})$ that we have obtained to the best estimate $\theta_{corr}(x)$ of ref. [3] taking into account corrections to scaling. In this case, we see that only rather small corrections were necessary. This is not always the case, and corrections to scaling can turn out to be much more important, as in the case of fixed boundary conditions, as we will see in chapter 5 (e.g. Fig. 5.8). Actually, various corrections to scaling ansätze have been explored in ref. [3], which proved more suited to other boundary conditions and to the results obtained in the XY model. We refer the reader to ref. [3] for further discussions on the matter.

4.3.8 Numerical simulations compared to experimental results

As we already mentioned, the fully periodic boundary conditions cannot be related to any experimental situation. The slab geometry describes well the experimental set up of wetting films of ^4He [64] or $^3He -^4 He$ mixture [6, 73, 74] subject to a superfluid transition, or a demixing transition in a binary polymer mixtures [5]. The first case belongs to the universality class of the 3D XY model with (O, O) confining boundary conditions and the other to the 3D Ising model with $(+, -)$ boundary conditions. The Casimir scaling function has been computed numerically in these cases [3] and the results compare very well with experiments in the XY universality class and are also in agreement in the Ising one, Fig.4.6.

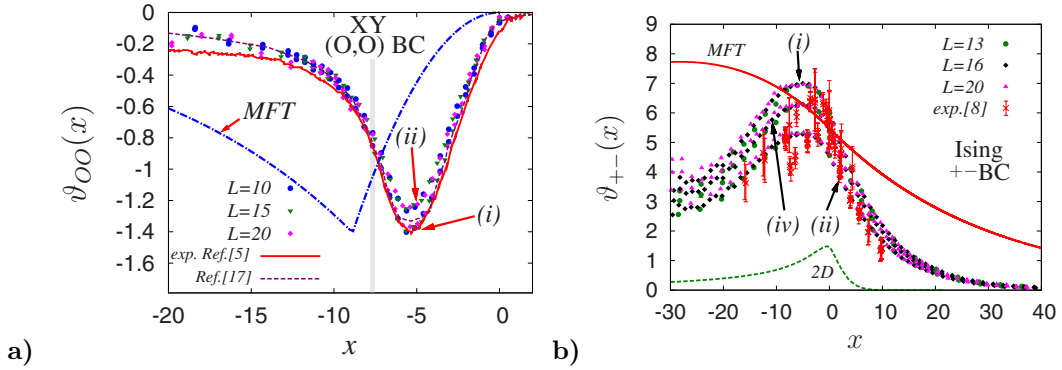

Figure 4.6: *Figure extracted from ref. [3]:* **a)** colored dots represent the scaling function of the Casimir force $\vartheta_{OO}(x)$ in the 3D XY universality class with (O, O) boundary conditions for different system dimensions and collapsed using two different corrections to scaling anzätse $(i), (ii)$ (see reference for details). The red curve comes from measurements of ref. [6, 64] and the purple dashed line represents other numerical results of ref. [103]. Excellent agreement is obtained between numerical and experimental works. **b)** Colored dots represent the scaling function of the Casimir force $\vartheta_{+-}(x)$ in the 3D Ising universality class with $(+, -)$ boundary conditions for different system sizes and collapsed using three different corrections to scaling anzätse $(i), (ii), (iv)$ (see reference for details). Red points with error bars come from measurements of ref. [5], showing good agreement with the numerical work.

4.3.9 Conclusion

The method of thermodynamic integration over a crossover parameter, or coupling parameter approach, has proved very efficient, leading to later studies, for example, in sphere-plane geometry [47], with variable boundary fields [87], a bulk field [78] or more recently in the presence of random surface fields [96]. However, this method clearly cannot be adapted to an experimental set up. Moreover, from our previous discussions it appears that, apart from the preliminary work of ref.

[62] in 1998 trying to directly reproduce wetting experiments in a Lennard-Jones simulation, there is a dichotomy between experimental measurements and numerical simulations of the Casimir force. Measurements are performed in fluid systems, whereas theoretical and numerical works study magnetic models. We have already mentioned above the possibility of computing the free energy through integration of the specific heat C_v. Such an approach is experimentally challenging and requires a double integration on temperature to estimate the free energy from C_v. We have recently developed and numerically tested a new protocol for the measurement of the magnetic Casimir force based on the concept of generalized thermodynamic forces, showing that equivalent results to previous works can be achieved by directly evaluating free energy changes through integration of the magnetization from a reference state at high magnetic field into the critical region. In chapter 5, we will describe our proposal for the first protocol adapted to experimental measurements of the critical Casimir force in magnetic systems. Conversely, in chapter 7, we will try to close the gap between experimental and numerical approaches, this time by numerically studying the Casimir effect in a fluid system, through simulations of a Lennard-Jones symmetrical binary mixture.

Chapter 5

The Critical Casimir Force in a Magnetic System ; an Experimental Protocol

On the one hand, spin models are the paradigm for computing the universal scaling function of the critical Casimir force, the most experimentally relevant being the Ising and XY models. Theoretical [20, 77, 97, 104] and numerical [3, 9, 21, 57, 58, 69, 75, 76, 78, 80, 103, 105] studies systematically use approaches based on generalized thermodynamic relationships between the constraining forces and the relevant free energy. On the other hand, experimental measurements of the critical Casimir effect were performed in fluid systems [5, 64, 67, 73, 74], as introduced in chapter 4, probing directly or indirectly the confining force. Thus, there is a clear segregation between theoretical and numerical works in magnetic systems on one side and experimental measurements in fluid systems on the other.

Given the success of spin models in the accurate computation of the critical Casimir force in almost all situations, it is paradoxical that no magnetic experiments exist which attempt to measure the scaling function from estimates of free energy differences, given that magnetic experiments have long been considered as the paradigm for studies of criticality (see for example ref. [17]) and that the nano-engineering of magnetic thin films is particularly well-advanced [18]. The reason is that the numerical techniques, accurate though they may be, are not adapted to experiments. Moreover, the experimental approaches developed for fluid systems are not suited for magnetic materials as they rely on directly or indirectly measuring a pressure, which is not in general a relevant thermodynamic observable for a solid material, especially in the absence of magneto elastic coupling.

We have developed and numerically tested a new protocol for measurement of the magnetic Casimir force based on the concept of generalized thermodynamic forces, showing that equivalent results to previous works can be achieved by directly evaluating free energy changes through integration of the magnetization from a reference state at high magnetic field into the critical region. Here, evolution of the free energy with system size yields the critical Casimir effect

without direct access to the constraining force. This procedure could be adapted into the first experimental protocol for magnetic thin films, or for systems as diverse as ferroelectrics, liquid crystals or polymers and could give access to all universality classes including quantum criticality. This work has been published in the Physical Review B [16].

5.1 Free energy and integration of observables

As we have seen in the previous chapter, extremely efficient numerical algorithms already exist for the simulation of the critical Casimir force within the framework of lattice based spin models. These algorithms make use of the thermodynamic relationship between force and free energy (Eq.4.12), making a discrete estimate of $\frac{\partial \Omega}{\partial L_\perp}$, rather than simulating a direct force measurement. We have detailed in the previous chapter (section 4.3) a method giving direct access to free energy changes induced by adiabatically disconnecting a single layer of spins from a connected stack of $L_\perp$ layers. The method provides accurate estimates for the Casimir force for different universality classes and boundary conditions both for zero field [3], and more recently for non zero field [78]. We also mentioned the possibility of defining a magnetic stress tensor, equating the critical Casimir force with its anisotropic part [21], thus circumventing the integration over the auxiliary degree of freedom λ. This technique has been successfully used for varied situations, limited at present to zero field and periodic boundaries. Nevertheless, successful as these techniques may be, it is clear that they have no experimental equivalent.

A more experimentally relevant approach relies on a simple statement: thermodynamic observables are defined as derivatives of the free energy. We mentioned a text book approach to computing the free energy [2] using both the average internal energy U and the entropy S computed by integration of the specific heat $C_v = T\frac{\partial S}{\partial T}\Big|_V$ to reconstruct the free energy $\Omega = U - TS$. The free energy can actually be directly computed by integration of the internal energy with respect to temperature as $U = \frac{\partial \varkappa \Omega}{\partial \varkappa}\Big|_h$, with $1/\varkappa = k_B T$. Free energy differences have been estimated by tracking the evolution of the excess internal energy with temperature for systems of size $L_\perp$ and $L_\perp - 1$ [9, 57, 69, 76, 103, 105]. Using this method it has been possible to make accurate estimates of the scaling function in the Ising universality class [57, 76] and of the scaling function extracted from work function measurements on helium films near the superfluid phase transition [103], showing excellent agreement with results of ref. [3] previously discussed (Fig.4.6). However, neither the internal energy at temperature T, nor that at a required reference state are themselves directly accessible in experiment. One still has the option of performing a double integration of the specific heat $C_v(T) = -T\frac{\partial^2 \Omega}{\partial T^2}\Big|_{V,h}$ with respect to temperature to access the free energy. This route has been explored in ref. [9] for the 3D XY universality class: numerical estimates of the universal scaling function of the Casimir force were compared to the one obtained using specific heat measurements in helium 4 [7, 8], obtaining a convincing agreement but with very strong size effects (additional to finite-size scaling) which became dominant when decreasing

the temperature, preventing the estimation of the Casimir function in the low temperature region.

The specific heat is a rather difficult quantity to measure and we have seen in figure 2.4 of chapter 2 that, because of its very slow divergence close to the critical point, its critical behavior seems the most difficult to capture. Thus we turn to the magnetization as the suitable first derivative of the free energy and most easily accessible magnetic observable.

5.2 Casimir force and integration of the magnetization

As in chapter 4, we concentrate on a system with scalar order parameter m, conjugate external field h, volume V and free energy $\Omega_{slab}(T, h, V)$, close to a second order phase transition. Anisotropic confinement is allowed for by setting $V = AL_\perp$, with $\sqrt{A} = L_\parallel \gg L_\perp$. We recall dimensionless variables, $t = (T - T_c)/T_c$, $\tilde{h} = h/k_B T_c$, with T_c the bulk three-dimensional critical temperature.

As mentioned in the previous chapter, in the case of a lattice model the fourth relevant thermodynamic variable N is omitted, as the magnetic moment density $n = \frac{N}{V}$ is fixed. In this case volume fluctuations impose fluctuations in the number of magnetic elements, so that one is dealing with a uniform magnetic medium. While spontaneous fluctuations of this kind clearly cannot exist in conventional magnetic systems [75], the evolution of the free energy with system size can give indirect access to the Casimir force and this is the goal of our approach. An alternative constraint would be to impose N constant, so that volume fluctuations would lead to magneto-elastic effects, as is the case in real magnets. In principle one could imagine magnetic experiments that directly measure Casimir forces through magneto-elastic coupling, although the separation of the critical and bulk contributions could be difficult. In practice, as magnetic exchange coupling varies rapidly with inter-atomic distance the critical properties are strongly perturbed and renormalization studies predict the transition to be driven first order by the coupling [106]. This driving to first order is reminiscent of the existence of a tricritical point for the Blume-Capel model, in which the density of magnetic elements is allowed to vary (see section 4.3.7). This, in itself is an interesting field of study, but in the present work we neglect all magneto-elastic effects and concentrate on the free energy which is generic to magnetic and fluid systems. For convenience, we set the microscopic length scale $\sigma = 1$.

As we developed in section 4.2, the free energy can be decomposed in slab geometry as

$$\frac{\Omega_{slab}(T, h, L_\perp, A)}{A k_B T} = L_\perp \; \omega_{bulk}(T, h) + \omega_{surf}(T, h) + L_\perp \omega_{ex}(T, h, L_\perp) \; , \tag{5.1}$$

and the critical Casimir force is defined as

$$f_c = -k_B T \frac{\partial (L_\perp \omega_{ex})}{\partial L_\perp}\Big|_{T,h} = k_B T L_\perp^{-d} \theta \left(u_t, u_h\right) \; . \tag{5.2}$$

The difference in free energy along an isotherm, between a reference state, (T, h_0) and a final

state (T, h) can be obtained through the magnetization

$$\Delta\Omega = -\int_{h_0}^{h} \langle M(T, h', L_\perp)\rangle dh' \ . \tag{5.3}$$

Even if we choose $T \sim T_c$, if $|h_0|$ is chosen to be sufficiently large, the correlation length at the reference state will be small so that the reference free-energy will be essentially that of the bulk $\Omega_{slab}(T, h_0, L_\perp) = V k_B T \omega_{bulk}(T, h_0)$. As a consequence $\Delta\Omega$ should contain all the information of the Casimir effect at (T, h). This is similar to the procedure that could be developed along the temperature axis by integrating the specific heat, but this route would require a double integration [9]. Repeating this procedure for systems of size $L_\perp$ and $L_\perp - \delta L_\perp$ and applying the extensivity principle for the free energy away from criticality one finds

$$\begin{aligned} \delta'\Omega(T, h, \ell) &\equiv \Delta\Omega(L_\perp) - \Delta\Omega(L_\perp - \delta L_\perp) \\ &= \delta\Omega(T, h, \ell) - \frac{\delta L_\perp}{L_\perp}\Omega_{slab}(T, h_0, L_\perp) \\ &= \delta\Omega(T, h, \ell) - \delta L_\perp A k_B T \omega_{bulk} \ , \end{aligned} \tag{5.4}$$

where $\delta\Omega$ is the increment in free energy, equating approximately to

$$\delta\Omega(T, h, \ell) \approx \delta L_\perp \frac{\partial\Omega}{\partial L_\perp}(T, h, \ell) \ , \tag{5.5}$$

evaluated at T, h and $\ell = L_\perp - \delta L_\perp/2$. This intuitive choice for ℓ has been shown rigorously to facilitate the approach to the scaling limit by minimizing the importance of corrections to scaling terms [75]. Non-critical surface free energy corrections cancel in the subtraction of the contributions from the two length scales. One now repeats the procedure for two sets of length scales centered on ℓ and $\alpha\ell$. Subtracting results from the two pairs of length scales eliminates the free energy from the reference state, $\Omega_{slab}(T, h_0, L_\perp)$, as well as the bulk contribution to the free energy at the point of interest, $\omega_{bulk}(t, h)$, providing a first estimate of the Casimir force:

$$\begin{aligned} f_c^0(T, h, \ell) &= -\left[\delta'\Omega(\ell) - \delta'\Omega(\alpha\ell)\right] \frac{1}{A\delta L_\perp} \\ &= -\left[\delta\Omega(\ell) - \delta\Omega(\alpha\ell)\right] \frac{1}{A\delta L_\perp} \\ &\approx f_c(\ell) - f_c(\alpha\ell) \ . \end{aligned} \tag{5.6}$$

One could also think of using a thermodynamically large cubic system as a reference bulk state, but this would require the growth of a large enough monocrystal without defects. Given the universal scaling form for f_c (Eq. (5.2)) one can define a scaling function for f_c^0

$$f_c^0(T, h, \ell) = k_B T \ell^{-d} \theta^0 \left(u_t[\ell], u_h[\ell]\right) \ , \tag{5.7}$$

where $u_t[\ell] = t\ell^{1/\nu}$ and $u_h[\ell] = \tilde{h}\ell^{(\beta+\gamma)/\nu}$ are the appropriate scaling variables. The scaling function $\theta^0(\ell)$ is related to θ at two different values of $u_t[\ell]$ and $u_h[\ell]$

$$\theta^0(\ell) = \theta(\ell) - \alpha^{-d}\theta(\alpha\ell) \ , \tag{5.8}$$

equation that can be solved using the iterative procedure described in Chapter 4, section 4.3.5.

5.3 Numerical method

We have tested these ideas through Monte Carlo simulation of a nearest neighbor Ising spin system with coupling strength $J = 1$ (for simplicity) and external field h, on a cubic lattice in slab geometry with $L_\parallel > L_\perp$. The magnetic order parameter is

$$\langle m \rangle = \frac{1}{V} \left\langle \sum_i S_i \right\rangle, \tag{5.9}$$

where $\langle X \rangle$ is a thermal average. In the previous chapters, we have sometimes used the observables $|m|$, as $\langle m(T, h = 0) \rangle = 0$ whatever the temperature in a finite size system where symmetry is not broken. Here, the relevant variable conjugate to the magnetic field h is $\langle m \rangle$, defined as a first derivative to the free energy.

To reduce critical slowing down we have used the Wolff algorithm, adapted to work in the presence of a symmetry breaking field (see Chapter 2). The boundary conditions were always set periodic in the $x - y$ plane but different boundaries along the z axis where explored: periodic or fixed $(+, +)$ and $(+, -)$ (see section 4.2.3). For temperatures below T_c, as the absolute value of the magnetic field $|h|$ increases, the number of rejected cluster flips increases dramatically, resulting in an increase of the autocorrelation time and therefore a loss of efficiency of the algorithm. Obtaining precise results at low temperature, particularly for $(+, -)$ boundary conditions requires a particularly large computation time [3]. The data we present in the article were obtained using a number of Monte-Carlo steps ranging from 5×10^4 for $(+, +)$ boundary conditions at the higher temperatures to 7×10^7 for temperatures far below T_c in systems with $(+, -)$ boundary conditions where the efficiency of the algorithm is at its lowest. The statistical error is evaluated using a modified bootstrap method [2]. As the presence of fixed boundary conditions and bulk magnetic field increases the correlation time τ_{corr} dramatically, we interpret the bootstrap method as providing a value for $\sigma_m / \sqrt{N_{\text{step}}}$ where $\sigma_m^2 = \langle m^2 \rangle - \langle m \rangle^2$ is the variance and N_{step} is the number of Monte-Carlo steps performed, rather than the error itself. To compute the statistical error we estimated the autocorrelation time τ_{corr} and then took the error to be $\sqrt{2\tau_{\text{corr}}\sigma_m^2 / N_{\text{step}}}$ [2], which proved in excellent agreement with the statistical noise observed. The simulations benefited from the numerical resources of the PSMN in Lyon [22].

From an numerical point of view, and for the same reasons as in the previous chapter (section 4.3), we chose to study preferentially system thicknesses $\ell = 9.5$ and $\alpha\ell = 19.5$ and initially took $\delta L_\perp = 1$. Different constraints motivate this choice: first ℓ has to be big enough with respect to the variation $\delta L_\perp$ so that the derivative of the free-energy with respect to the system size can be safely approximated by the differential $\frac{\delta \Omega_{slab}}{\delta L_\perp}$. In order to test the robustness of this approximation, $\delta L_\perp = 3$ and 5 have also been investigated. Secondly, ℓ must be big enough to allow an approach into the three dimensional scaling regime. This choice is moderated by the fact that the difference in magnetization for different system sizes falls to zero as the thermodynamic limit is approached, so that a pragmatic compromise is required, both in simulation and

in any future experiment. These considerations motivates the choice of relatively modest system size $\ell = 9.5$. Thirdly, α has to be as large as possible to have a fast convergence of the iteration process that extracts the approximation θ^k from the measured θ^0. Here $\alpha = 19.5/9.5 \approx 2$. The transverse size $L_\parallel$ should be chosen as big as possible with respect to $L_\perp$ in order to ensure that we stay in the anisotropic confinement regime. In all our simulations we used $A = 3600$ enabling us to directly compare our results with those from ref. 3 where one can find detailed discussions on the impact of system size and of corrections to scaling, on the form of the universal function of the Casimir force obtained in the Ising and XY models.

5.4 Choice of h_0 and integration procedure

In figure 5.1 we show the evolution of the magnetization with applied field for $T = T_c$ for $L_z = 9, 10, 19, 20$ and in the case of either periodic boundaries along z or $(+,-)$ boundaries. In the case of fully periodic boundary conditions, the difference in $\langle m(L_\perp, h)\rangle$, for small h is clearly visible for $L_\perp = 9$ and 10, becoming much smaller for the larger $L_\perp$. The Casimir force comes from the integral of these differences with field, so that system sizes straddling $L_\perp = 10$ appear to offer a good pragmatic place to start. For this length scale the effect is pronounced, while one is already in the scaling regime to within a reasonable approximation. In addition, magnetic films of this thickness can be produced with great precision so that these parameters already correspond to the state of the art for thin film production [18]. In the case of $(+,-)$ boundaries, Fig.5.1b),

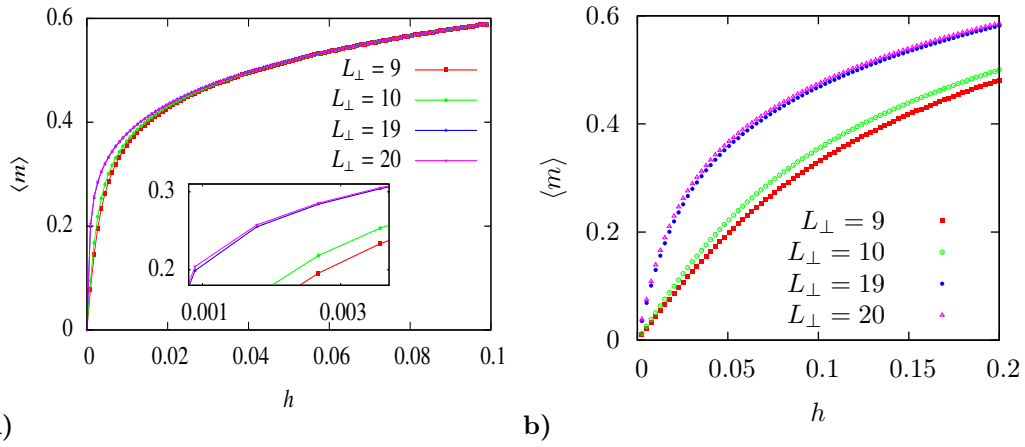

Figure 5.1: Magnetic order parameter vs. h at $T = T_c = J/0.22165$ for four different system thicknesses $L_\perp \in [9, 10, 19, 20]$, $A = 3600$ and either fully periodic boundary conditions **(a)** (**inset:** blow-up of the low field region of the magnetization) or $(+-)$ boundary conditions in the z direction **(b)**.

magnetization curves do not collapse for high values of h: the fixed boundary conditions can be considered as local magnetic fields $h_s = \pm J$ of total strength $\pm AJ$ and are in competition with the bulk magnetic field hV. This surface contribution is independent of $L_\perp$ and is suppressed in the differentiation process (Eq.5.4).

We can separate the magnetization in three contributions: bulk, surface and excess

$$\langle M(T,h,\ell,A)\rangle = V\langle m_{bulk}(T,h)\rangle + A\langle m_{surf}(T,h)\rangle + V\langle m_{ex}(T,h,\ell)\rangle \ . \tag{5.10}$$

To be able to extract the free-energy by integration of the order parameter, it is necessary to determine a suitable reference magnetic field h_0 for which the excess part can be safely considered negligible. From the magnetizations of four systems of same area A but four different thicknesses $L_\perp \in [\ell \pm \delta L_\perp/2, \alpha\ell \pm \delta L_\perp/2]$, we can define the function

$$\begin{aligned} D(T,h,\ell) =& \frac{1}{A\delta L_\perp}\langle M\left(\alpha\ell + \delta L_\perp/2\right) - M\left(\alpha\ell - \delta L_\perp/2\right) - M\left(\ell + \delta L_\perp/2\right) + M\left(\ell - \delta L_\perp/2\right)\rangle \\ =& \frac{1}{A\delta L_\perp}\langle M_{ex}\left(\alpha\ell + \delta L_\perp/2\right) - M_{ex}\left(\alpha\ell - \delta L_\perp/2\right) - M_{ex}\left(\ell + \delta L_\perp/2\right) + M_{ex}\left(\ell - \delta L_\perp/2\right)\rangle \ , \end{aligned} \tag{5.11}$$

where all the magnetizations are taken at the same temperature and magnetic field, omitted in the notation for the sake of lightness. This is a purely "excess" quantity, directly related to the Casimir effect as

$$\theta^0(u_t,u_h) = \frac{\ell^d}{k_B T}\int_h^{h_0} dh'\ D(T,h',\ell) \ . \tag{5.12}$$

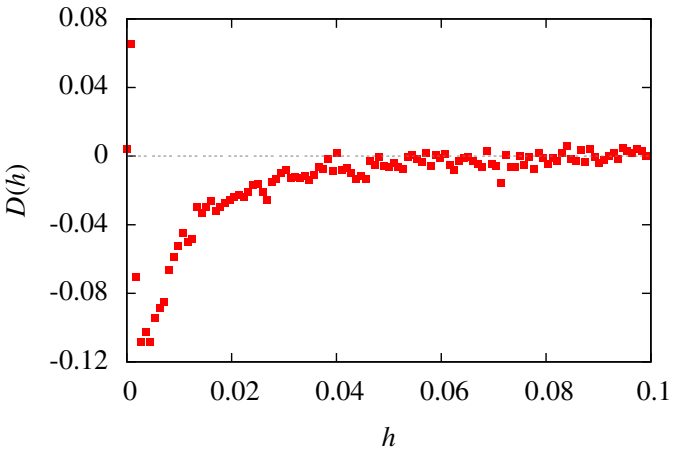

Figure 5.2: Function $D(T,h,\ell)$ defined in Eq.5.11 with respect to the magnetic field h. The data were obtained at $T = T_c$ for periodic boundary conditions and $\ell = 9,5$,$\alpha\ell = 19,5$ and $A = 3600$ (same data as in Fig.5.1). The integration of $D(T,h,\ell)$ over h gives θ^0. $D(T,h,\ell)$ goes to zero as h is increased, h_0 should be chosen so that $D(T,h,\ell)$ is zero within the current precision of the simulation, ensuring that finite size effects are suppressed by this field.

Functions D and θ^0 also depend on the choice of the parameters α and $\delta L_\perp$ but we omit this dependences in our notations, again for sake of lightness. To illustrate the procedure further we concentrate on the case of fully periodic boundaries of Fig.5.1a), for which $\ell = 9.5$, $\alpha\ell = 19.5$ and $\delta L_\perp = 1$ and figure 5.2 shows the corresponding function $D(T, h, \ell)$. At zero magnetic field the value of the magnetization $\langle m(L_\perp, h = 0)\rangle = 0$ is imposed by magnetic moment reversal symmetry, thus $D(T, h = 0, \ell) = 0$ (Fig 5.2). At low magnetic field the magnetization depends on $L_\perp$ and $D(T, h, \ell) \neq 0$. The magnetization curves asymptotically merge as the magnetic field is increased, reducing the correlation length and consequently suppressing finite-size effects, so that $D(T, h, \ell) \underset{h\to\infty}{\to} 0$, this limit being unchanged by the presence of surface fields as D is a purely excess quantity. Roughly speaking, we can convince ourselves from figure 5.2 that for $h \gtrsim 0.08$, D can safely be considered null within the current precision of the simulation. Carrying out the integration of Eq.5.12 using a reference magnetic field $h_0 > 0.08$ would add more noise than signal to θ^0. We can thus use D to choose a suitable value for h_0, large enough so that the value of $\theta^0(u_t, u_h)$ reaches an asymptote. The integration of Eq.5.12 was then performed using Simpson's rule from h_0 to h for all computed values of h. Note that h_0 depends on the temperature considered and, as the size of the critical region shrinks when getting away from T_c, the reference magnetic field will vanish accordingly. A possible pitfall of this method could arise if the function D did not, as expected, decay exponentially fast at high magnetic field. For example, a power law decay, even far from the critical point, could result in the choice of a reference field for which D is negligible with respect to the noise but which truncates a significant part of the integral of Eq.5.12.

5.5 At zero magnetic field

5.5.1 First estimate θ^0 at zero magnetic field

To make contact with previous works, in Figure 5.3 we compare the zeroth order scaling function, $\theta^0(u_t, 0)$ extracted using the magnetic protocol described above with that from reference [3] for $(+,+)$ and $(+,-)$ boundary conditions. In all cases $\ell = 9.5$, $\delta L_\perp = 1$ and $\alpha\ell = 19.5$. One can observe excellent agreement between the two data sets for both boundary conditions, thus confirming our protocol as a viable method of extracting critical Casimir forces. We have also successfully tested our protocol against the coupling parameter method for periodic boundaries. The difference in sign and amplitude of the Casimir force between $(+,+)$ and $(+,-)$ boundaries has its origin in the excess entropy of the trapped interface. This spectacular inversion and scale change is perfectly captured by our thermodynamic protocol. From here, the universal function θ can be extracted by iteratively solving Eq.5.8.

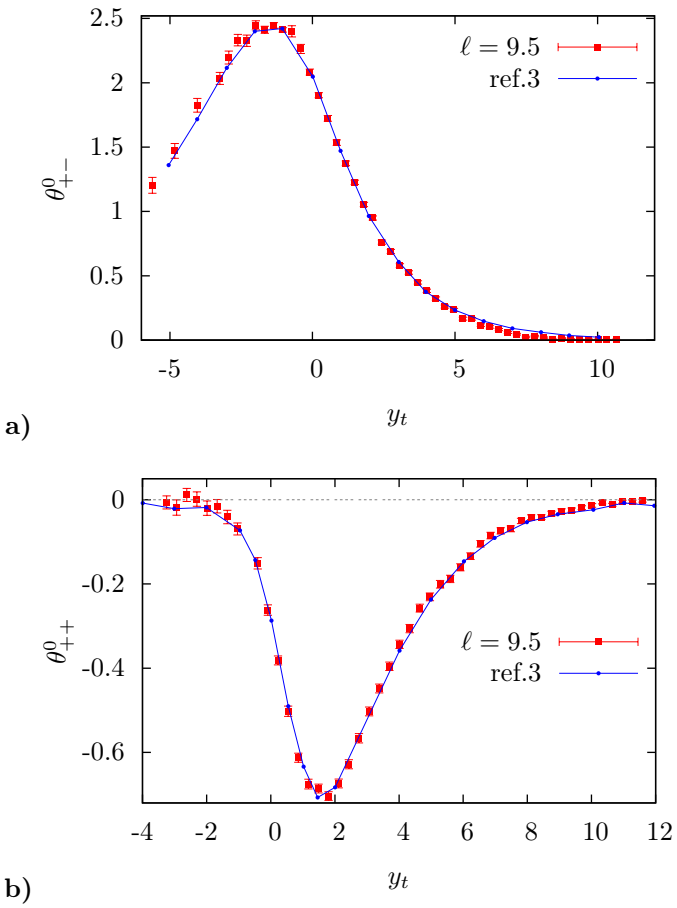

Figure 5.3: Zeroth order scaling function θ^0 vs $u_t = t\ell^{1/\nu}$ for $h = 0$. Data from the magnetic protocol outlined in the text (red cross), data from ref. [3] (blue line). Figure **a)** $(+,+)$ boundaries, **b)** $(+,-)$. In all cases $\ell = 9.5$, $\delta L_\perp = 1$ and $\alpha\ell = 19.5$, while $A = 3600$. The error bars were computed using a modified bootstrap method and an estimate of the autocorrelation time.

5.5.2 Iteration procedure

As we have already seen in Chapter 4, with our choice of system sizes and $\alpha \approx 2$, the scaling function θ^0 already provides a good estimate for the functional form of $\theta(u_t, u_h)$. Nevertheless, to improve the estimate of θ, we can use the procedure described in section 4.3.5, which converged within two iterations. For $n = 3$, we found that all points $(\alpha^{2^{n-1}/\nu}u_t, \alpha^{2^{n-1}(\beta+\gamma)/\nu}u_h)$ (except for $(u_t = 0, u_h = 0)$ of course) fell outside the range of values of (u_t, u_h) explored in our Monte-Carlo simulation. Hence, their contribution could safely be considered to be negligible within the precision of our simulation. Figure 5.4 presents, as an example, the evolution of $\theta^n_{++}(u_t, 0)$ between $n = 0$ and $n = 2$, with data found using $\ell = 9.5$, $\alpha\ell = 19.5$, $\delta L_\perp = 1$ and $A = 3600$.

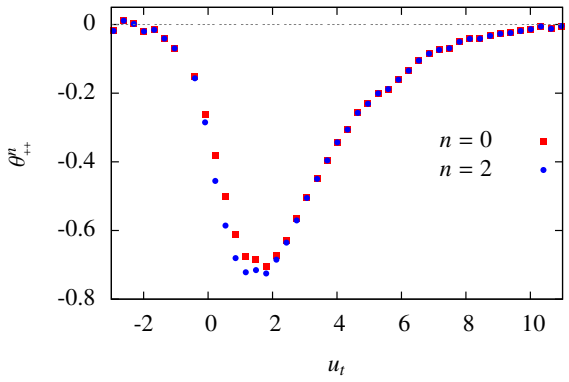

Figure 5.4: Evolution of the scaling function with the iteration procedure. Function $\theta^n_{++}(u_t, 0)$ of the Casimir force for $n = 0$ (red squares) and $n = 2$ (blue dots) as a function of reduced variable $u_t = t\ L_z^{1/\nu}$, computed using the proposed integration method for $(++)$ boundaries and $\ell = 9.5$, $\alpha\ell = 19.5$,$\delta L_z = 1$ and $A = 3600$.

5.5.3 Critical amplitude and corrections to scaling

Arriving at a scale free function from these system sizes also requires a delicate analysis of corrections to scaling [107]. Having made contact with previous work for these modest system sizes, we account for the corrections here by rescaling the data to the universal scaling amplitude, $\theta(0, 0) = 2\Delta$ for each set of boundaries. If this technique were developed in magnetic thin film experiments, it is likely that initial measurements would require scaling in the same way, as was the case for early experimental data for helium films to remove amplitude shifts due to uncontrolled surface roughness [6, 64]. Numerical estimates given in the literature vary: $\Delta_{++} = -0.376(29)$ and $\Delta_{+-} = 2.71(2)$ [3], $\Delta_{++} = -0.410(7)$ and $\Delta_{+-} = 2.806(10)$ [57]. Here we take values from [3], as our method relates to this work. We return to this subject below, where we present some initial finite size scaling results for the critical Casimir force in finite field.

5.6 Fixed $(+, +)$ boundary conditions and finite field

5.6.1 Positive magnetic field

Until recently [68, 78] there has been only minimal interest in the scaling of the critical Casimir force along the field axis. This can be explained in part by an absence of experimental motivation as it is difficult to probe the field variable in present setups: for the superfluid transition in ^{4}He films [64, 73] h is not accessible, while for binary liquid films [5], experiments are performed for fixed concentrations, rather than conjugate field. However, experiments on thin film magnets

lend themselves naturally to critical scaling in both u_t and u_h. Our numerical protocol is equally well adapted to work at non zero field and is in fact particularly efficient, as all points along an isotherm contribute to $\theta(u_t, u_h)$. Our procedure therefore opens up a new direction for the study of these forces. In Figure 5.5, we show $\theta(u_t, u_h)$ for $(+, +)$ boundaries, illustrating the form of the scaling function in the half plane, $h > 0$. This figure requires the same computational effort as the one dimensional data sets shown in Figure 5.3.

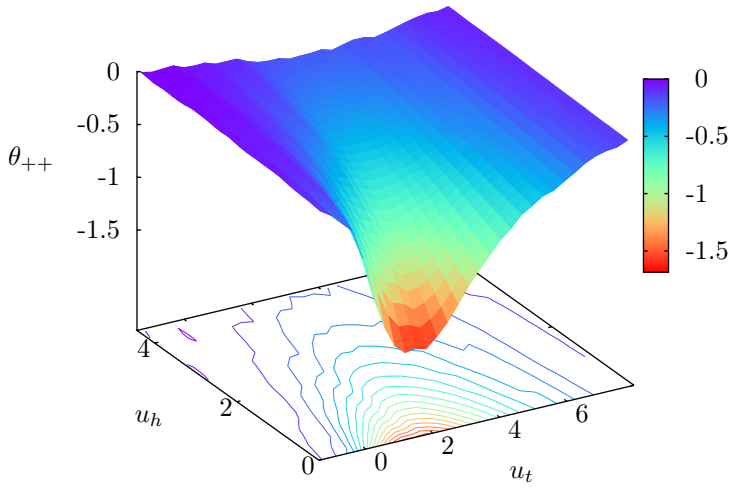

Figure 5.5: $\theta_{++}(u_t, u_h)$ for $(+, +)$ boundaries, found using the magnetic protocol outlined in the text for $\ell = 9.5$, $\alpha\ell = 19.5$, $\delta L_\perp = 1$ and $A = 3600$. The field is confined to the $+$ direction. The function was scaled to universal amplitude, $\theta_{++}(0, 0) = 2\Delta_{++} = -0.75$. The lines projected onto the base show contours of equal Casimir force.

5.6.2 Negative magnetic field

Minimum of the scaling function

The scaling function shows no minimum value as a function of field for $h > 0$. The minimum can be found in the half plane, $h < 0$, with the field in the opposite direction to the pinned boundaries. Remarkably, as we show in Figure 5.6, θ^0 plunges to values more than an order of magnitude lower, as one crosses the line to negative field values. This unexpectedly large amplitude [78] comes from the competition between opposing surface and bulk fields. At large separation, the applied field imposes two magnetization interfaces. For smaller $L_\perp$, this frustration is lifted

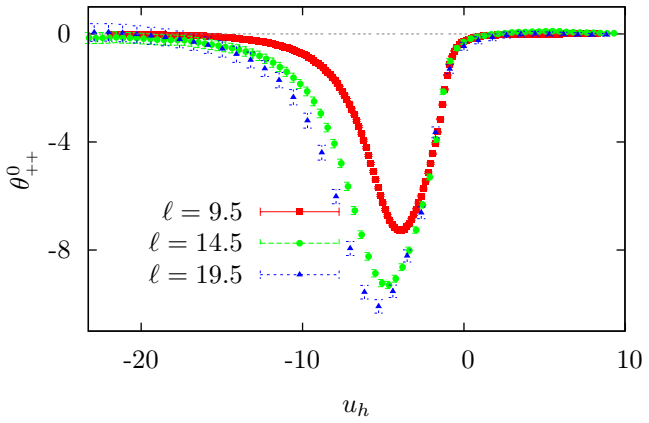

Figure 5.6: Zeroth order scaling function $\theta^0_{++}(0, u_h)$ for $(++)$ boundaries with field spanning both + and− directions. The data were obtained with three different sets of system sizes: $\ell = 9.5$, $\alpha\ell = 19.5$ (red squares), $\ell = 14.5$, $\alpha\ell = 29.5$ (green dots) and $\ell = 19.5$, $\alpha\ell = 39.5$ (blue triangles). For all sets of data $\delta L_\perp = 1$, A=3600 and $\alpha \approx 2$.

and symmetry is broken in the direction of the boundary field resulting in a particularly large Casimir force, which could be accessed in thin film experiments. This large effect can be quite straightforwardly understood when looking at magnetization curves of figure 5.7: finite size effects both influence the development of the amplitude of the magnetization but also the coercitive field for which $\langle m \rangle = 0$, so that close to this point, the change in magnetization with system size is quite significant. For small system sizes, this sharp evolution of the magnetization could lead to

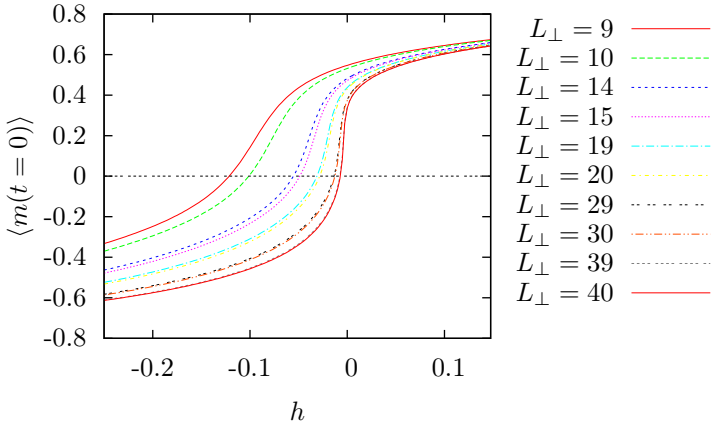

Figure 5.7: Magnetization with respect to field h at T_c for $L_\perp \times 60 \times 60$ systems with $(+,+)$ boundary conditions.

the failure of the approximation of derivatives by a finite difference with the change $\delta L_\perp$ and could explain the significant discrepancy between data for the Casimir effect displayed in figure 5.6 which were obtained with different sets of system sizes, $(\ell = 9.5, \alpha\ell = 19.5)$, $(\ell = 14.5, \alpha\ell = 29.5)$ and $(\ell = 19.5, \alpha\ell = 39.5)$, but keeping $\delta L_\perp = 1$ and $A = 3600$. This discrepancy can also be attributed to corrections to the slab limit [76], as the aspect ratio changes from one set of sizes to the other, or other corrections to the scaling limit. We will see later that it can be captured by a phenomenological change of the scaling length $\ell \to \ell_{eff}$.

One can notice that the error bars displayed on figure 5.6 are significantly larger for the lowest values of magnetic field than for the highest ones. This is due to the integration from high to low magnetic field we use to compute θ^0. Starting integration at the reference state h_0, we accumulate error during the integration process.

Iteration procedure

The large amplitude Casimir force encountered in the case of (++) boundaries for a field in the reverse direction, $h < 0$, as shown in Figure 5.6, puts a strain on the iteration procedure in the region where the scaling function evolves most rapidly with field. This produces a kink in the estimated function $\theta(0, u_h)$ for small, negative h, as shown in Figure 5.8 for three different system sizes $\ell = 9.5$, $\ell = 14.5$ and $\ell = 19.5$. The kink appears less pronounced for the larger system size, which suggests that it is an artifact of the procedure for small systems. More work would be required to confirm this point, considering in particular the rather low resolution of data for the biggest systems. However, it is clear that all sets of sizes produce very different estimates

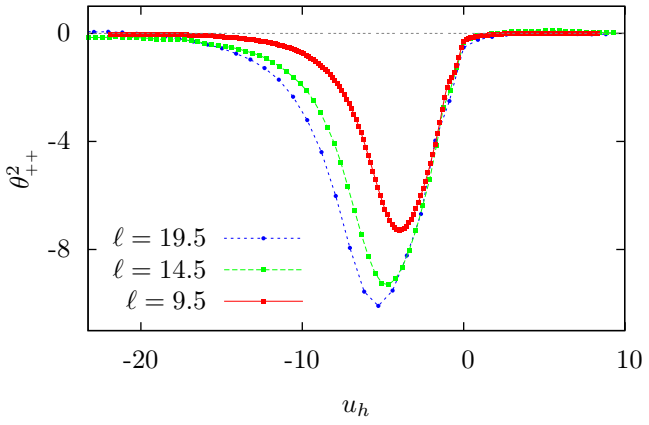

Figure 5.8: Improved estimate of the universal Casimir function $\theta^2_{++}(0, u_h)$, corresponding to the zeroth order scaling functions $\theta^0_{++}(0, u_h)$ of figure 5.6, obtained after applying $n = 2$ steps of the iterative procedure described in the text, that is to say to convergence within our current precision.

for the Casimir scaling function in the negative field region, suggesting that our results are far from the complete scaling regime. We therefore propose a rescaling method to take corrections to scaling into account.

Rescaling of θ_{++} : choice of an effective size ℓ_{eff}

The significant discrepancy between data for the Casimir effect obtained with two sets of system sizes, displayed in figure 5.6 and 5.8, can be attributed to the failure of the approximation of derivatives by finite differences but also to corrections to the scaling limit. Corrections of this amplitude are encountered elsewhere [3, 102]. They can be accounted for by introducing a phenomenological change to the scaling length [57, 75, 78, 87]: $\ell \to \ell_{\text{eff}} = \ell + \delta\ell$, see Figure 5.9, a process which can be justified analytically for the Blume-Capel model [57, 75]. Hasenbusch [57] argued that this correction could be understood as coming from the ad hoc separation of critical contributions in bulk and surface parts, forcing one to place a boundary separating surface spins from bulk spins. This choice modifies both critical contributions and leads to corrections to the scaling limit. We used this correction here in an exploratory manner. To obtain a data collapse, we calculate the necessary correction $\delta\ell$ so that $(\ell_{\text{eff}}/\ell)^d \theta^0_{++}$ is equal for the maxima of the three sets of data. We find, $\delta\ell = 2.57$ with an error of approximately 8 % considering the statistical error on the data (in ref. [16] we found a best collapse for $\delta\ell = 2.8$ but at that time the $\ell = 19.5$ results were not available). This correction affects both the amplitude of the function

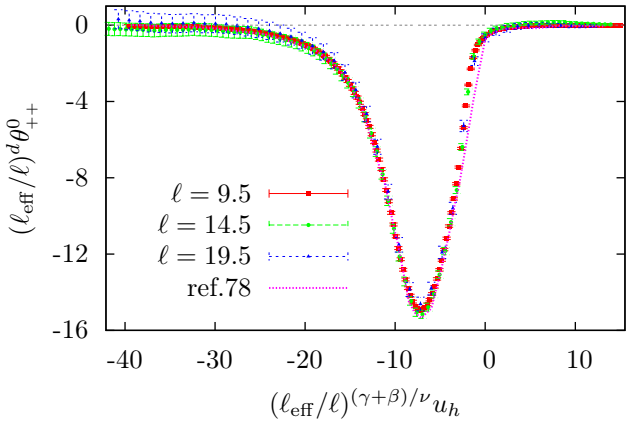

Figure 5.9: Zeroth order scaling function with $(+,+)$ boundaries for $(\ell = 9.5, \alpha\ell = 19.5)$ (red squares) and $(\ell = 14.5, \alpha\ell = 29.5)$ (green dots) and $(\ell = 19.5, \alpha\ell = 39.5)$ (blue triangles) collapsed using an effective length scale $\ell_{\text{eff}} = \ell + \delta\ell$. Here $\delta\ell = 2.57$. This correction affects both the amplitude of the function by a factor of $(\ell_{\text{eff}}/\ell)^d$ and the reduced parameter u_h by a factor $(\ell_{\text{eff}}/\ell)^{(\gamma+\beta)/\nu}$. For all data $\delta L_\perp = 1$ and $A = 3600$. For comparison we display data from ref. [78] (purple dashed line).

by a factor of $(\ell_{\rm eff}/\ell)^d$ and the reduced parameter $u_h = \tilde{h}L_\perp^{(\beta+\gamma)/\nu}$ by a factor $(\ell_{\rm eff}/\ell)^{(\gamma+\beta)/\nu}$. As shown in Figure 5.9, we find that this single parameter is enough to make the data collapse both in amplitude and width and reach a nice agreement with data from ref. [78], except for negative values of u_h close to 0 (we will see that this gap is closed by the iterative procedure). The rescaling of the amplitude of θ due to the factor $(\ell_{eff}/\ell)^d$ is $\sim 2.05 \pm 0.25$ for $\ell = 9.5$ and compares well with the ad hoc rescaling by a factor of 2.24 of the amplitude we used for the same system size in figure 5.5, which ensures that $\theta_{++}(0,0) = 2\Delta_{++} = -0.75$ [3].

In ref. [78], corrections to scaling are captured using a much smaller value of $\delta\ell = 0.60(10)$. We believe this discrepancy can in part be attributed to the different conventions used to define the thickness $L_\perp$. In our study, $L_\perp$ refers to the number of layers of fluctuating spins, whatever the boundary conditions [58], and impose the fixed boundary conditions by adding two layers of fixed spins. Whereas, in ref. [78], all layers are included in the count defining $L_\perp$ and the boundary conditions is imposed by strong local magnetic fields acting on boundary spins.

When performing iterations on the rescaled data, one should use $\alpha_{\rm eff} = \frac{\alpha\ell+\delta\ell}{\ell+\delta\ell}$ rather than α. Figure 5.10a) shows how the approximation $(\ell_{\rm eff}/\ell)^d\theta^n_{++}$ for $\ell = 9.5$ evolves from $n = 0$ to $n = 2$,

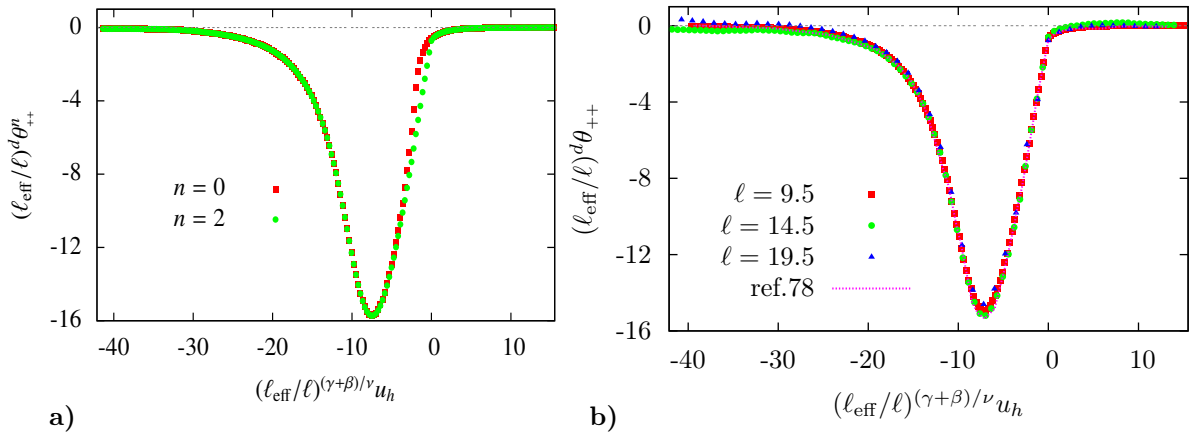

Figure 5.10: **a)** Recursion procedure combined with corrections to scaling. $(\ell_{\rm eff}/\ell)^d\theta^n_{++}(0,u_h)$ vs $(\ell_{\rm eff}/\ell)^{(\gamma+\beta)/\nu}u_h$, $n = 0$ (red squares), $n = 2$ (green dots). Data are for $\ell = 9.5$, $\alpha\ell = 19.5$, $\delta L_\perp = 1$ and $A = 3600$. Corrections to scaling that affect both the amplitude of the function and the reduced parameter $(\ell_{\rm eff}/\ell)^{(\gamma+\beta)/\nu}u_h$ also affects the iteration process, as an effective value $\alpha_{\rm eff} = \frac{\alpha\ell+\delta\ell}{\ell+\delta\ell}$ was used instead of α. Thus, we obtain the best estimate **(b)** of the universal scaling function $(\ell_{\rm eff}/\ell)^d\theta_{++}(0,(\ell_{\rm eff}/\ell)^{(\gamma+\beta)/\nu}u_h)$ for $(+,+)$ boundaries with field spanning both $+$ and $-$ directions, here for three sets of system sizes $(\ell = 9.5, \alpha\ell = 19.5)$ (red squares), $(\ell = 14.5, \alpha\ell = 29.5)$ (green dots) and $(\ell = 19.5, \alpha\ell = 39.5)$ (blue triangles). The data sets were rescaled to universal amplitude and width by replacing ℓ with $\ell_{eff} = \ell + \delta\ell$, with $\delta\ell = 2.57$. For comparison we display data from ref. [78] (purple dashed line).

the convergence point of our iteration procedure. The function $(\ell_{\text{eff}}/\ell)^d\theta^2_{++}(0,u_h)$ of Figure 5.10a) obtained using this procedure is in good agreement with that from reference [78], without any further renormalization although our protocol yields a bigger value of $\delta\ell$. The iterative procedure was applied to data obtained with all system sizes $\ell = 9.5, 14.5$ and 19.5, leading to our best estimate of the Casimir universal function $(\ell_{\text{eff}}/\ell)^d\theta_{++}(0,(\ell_{\text{eff}}/\ell)^{(\gamma+\beta)/\nu}u_h)$ displayed in figure 5.10b). The kink seen in Figure 5.8 is smoothed out in the rescaling process and the amplitude of the collapsed curves corresponds reasonably to that set by numerical estimates of the universal scaling amplitude, Δ_{++}. The agreement with results of reference [78] is very convincing, even though our estimate of $\delta\ell$ is only precise up to 8 %.

5.6.3 Low temperature and negative field region

In the low temperature region $T < T_c$, for negative magnetic fields, the magnetization can display a very brutal change of sign as shown in figure 5.11. The coercitive field changes with system size as it results from the competition between bulk and surface fields. The very sharp change of magnetization from positive to negative values makes our measurement very sensitive to the resolution in magnetic field. This non critical effect introduces a very important artifact in our method which cannot be reduced by any effective length scale and is extremely sensitive to the uncertainty in the coercive field value. Establishing the frontier from a result dominated by this artifact and the genuine Casimir effect would require more simulations.

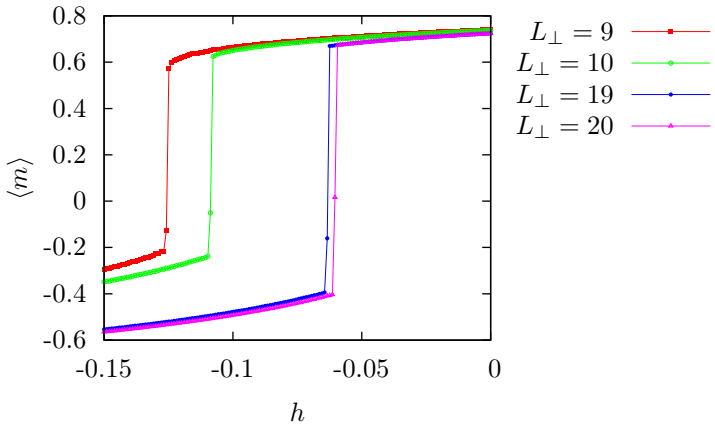

Figure 5.11: Magnetization with respect to field h at $T = 4.1J < T_c$ for $L_\perp \times 60 \times 60$ systems with $(+,+)$ boundary conditions.

5.7 Experimental perspectives

Having established the potential of the method to construct the Casimir scaling function from measurements of the magnetic moment, we now return to confrontation with experiment.

5.7.1 Influence of $\delta L_\perp$

The experimental feasibility of this protocol requires the fabrication of samples with thickness resolution better than $\delta L_\perp$ as well as the capacity to keep the uncontrolled errors generated by measurements on different samples at different times below the same threshold. The chances of success would clearly be increased if one could increase $\delta L_\perp$ above a monolayer. With this in mind we have investigated the measured Casimir effect for different values of $\delta L_\perp$. The results

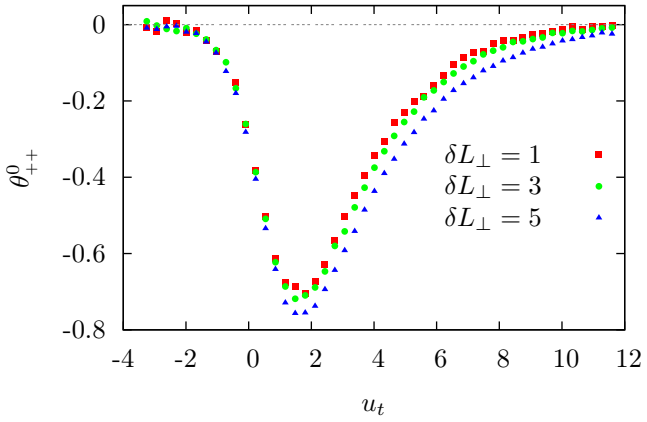

Figure 5.12: Scaling function θ^0 vs $u_t = t\ell^{1/\nu}$ for $h = 0$, $\ell = 9.5$ and $(+,+)$ boundaries. Data from the magnetic protocol outlined in the text (red squares) for $\delta L_\perp = 1$, $L_\perp = 10$, for $\delta L_\perp = 3$, $L_\perp = 11$ (green dots), for $\delta L_\perp = 5$, $L_\perp = 12$ (blue triangles). $A = 3600$.

are shown in Figure 5.12 for $\delta L_\perp = 1, 3$ and 5, for fixed $\ell = 9.5$. Remarkably, the evolution of the estimated function, θ^0, on moving from $\delta L_\perp = 1$ to 3 is extremely small, with a typical difference of less than 5% as the function passes through its minimum between $u_t = 1$ and $u_t = 2$. This small evolution is only just resolvable above the statistical error on our data, which is approximately 1.5% in this region. Even for $\delta L_\perp = 5$ the evolution remains less than 11% around the minimum of the function, while in all cases, increasing $\delta L_\perp$ enhances the measured Casimir force. In addition, as the free energy difference $\delta\Omega$ increases with $\delta L_\perp$, the statistical errors are reduced, even in the wings of the figure. The effect therefore appears extremely robust and our results strongly suggest that it would stand up to the technical problems encountered in dedicated experiments on magnetic thin films [19].

5.7.2 Experimental set ups

Perhaps the most important point to address is the scale of the magnetic field required. Most of the Casimir signal comes from small fields, but in order to capture the entire effect it was necessary to go to fields as large as $|h_0|/J \sim 0.3$ for certain temperatures and boundary conditions (see Figure 5.1,5.2 and 5.5). One is therefore limited to ferromagnets with Curie temperatures up to around 100 K for fields up to ~ 10 Tesla, provided that an "Ising model field" $h = 0.3J$ corresponds to a magnetic field $H \sim 0.3 \times 2k_B T_c \times 0.22165/(g\mu_B)$ in Tesla, using the bulk critical temperature $T_c = J/0.22165$, the Bohr magneton μ_B and a Landé factor $g = 2$ for 1/2 spins.

Experimental systems [19] potentially cover a wide range of universality classes and surface conditions, opening the possibility for a rich variation in universal behavior. Our protocol can easily be extended to cover many of these situations, and we stress on the fact that accessing the free-energy from integration of observables is a very general approach. Other universality classes can easily be treated, as can the anisotropic spin Hamiltonians often appearing in magnetic systems. In such cases one expects crossover from the microscopic starting point to the final universality class as the correlation length grows. These effects could be studied in detail and could be highly relevant for magnetic experiments. Boundary effects could be extended to include both rough and soft interfaces [6, 64, 84, 96]. However, materials with a strongly anisotropic spin Hamiltonian and hard smooth interfaces offer the most promising starting point.

Magnetic materials show essentially perfect model magnetism in many instances (see for example refs. [28, 108, 109]) and are excellent candidates for the exploration of different boundary conditions. Candidates for the Casimir effect would be ferromagnets and could include both metallic and insulating materials. Promising characteristics that one might consider include iron doped palladium films for which both the transition temperature and film thickness can be accurately controlled [110–112]. The films can be grown on non-magnetic substrates such as Vanadium allowing again for free magnetic boundaries, but they can also be grown on ferromagnetic substrates such as iron itself. This would allow for the study of fixed boundaries. Pinning the interface with moments pointing out of the sample, as can be done by roughening the interface [113], would lead to $(+,-)$ boundaries, hence enhancing the magnitude of the Casimir force. In the case of insulating compounds $Tb(OH)_3$ and K_2CuCl_4,$2H_2O$ are examples of Ising and Heisenberg ferromagnets respectively with Curie temperatures in the 5K range [19]. The metallic RKKY material, $HoRh_4B_4$ is a perfect mean field ferromagnet [38] which could offer access to mean field critical Casimir forces for the first time. The dipolar ferromagnet, $LiHoF_4$ is the archetypical transverse field Ising system [114] which, if produced as a film could provide a candidate for the study of Casimir forces at a quantum critical point [115]. Lutetium Vanadate $Lu_2V_2O_7$, a ferromagnet ordering at $T_C = 70K$ has been shown to be Heisenberg-like to an excellent approximation [116, 117].

Finally, we remark that our protocol could be extended to study non-magnetic systems such as ferroelectrics, liquid crystals or simple and binary fluids, as it offers a generic method when the

field conjugate to the order parameter is a control parameter. It could then be experimentally relevant in setups for fluid systems if the chemical potentials could be controlled, rather than the concentrations.

Chapter 6

Excess Free Energy in a Confined Geometry

In chapter 4, we have mentioned that the critical Casimir force could be decomposed (Eq.4.15 to 4.18) into three contributions from the excess free energy, the excess internal energy and the excess order parameter, which can all be expressed using the scaling function of the excess free energy. In the case of the Ising model with fully periodic boundary conditions, this relationship was studied theoretically in slab ($\rho > 1$), cubic ($\rho = 1$ and rod ($\rho < 1$) geometries [118, 119], in the 2D Ising model in rectangular geometry [76] and through Monte-Carlo simulations in 3 dimensions [76].

We will see in this chapter that we can take advantage of the relation between the scaling functions of critical Casimir force and the free energy to extract the excess free energy from data presented in chapters 4 and 5, for the case of fully periodic boundary conditions but also fixed $(++)$ and $(+-)$ confining boundary conditions. We will thus use in the present chapter the same notations and formalism as in chapter 5. We compute the universal scaling function Θ of the excess part of the free energy ω_{ex} in an Ising 3D system in slab geometry. The knowledge of such a scaling function gives access to all excess parts of observables deriving from the free energy: magnetization, specific heat and susceptibility, and of course the critical Casimir force [9]. However, to our knowledge, only little interest has been given to the computation of Θ compared to the abundant literature concerning the scaling function of the critical Casimir force.

6.1 The excess free energy from magnetization data

6.1.1 Fully periodic boundary conditions

As discussed in the previous chapter, the difference in free energy along an isotherm, between a reference state, (T, h_0) and a final state (T, h) is

$$\Delta\Omega = -\int_{h_0}^{h} M(T, h', L_\perp) dh' \ . \tag{6.1}$$

We have already detailed in section 5.2 how the choice of an appropriately large reference magnetic field $|h_0|$ enables us to construct purely excess quantities from this integration. In the case of periodic boundary conditions, there is no surface contribution ω_{surf} to the free energy (following the decomposition of Eq.5.1), so that repeating the procedure of Eq.6.1 for systems of size $L_\perp$ and $L'_\perp = \alpha L_\perp$ and applying the extensivity principle for the free energy away from criticality one finds

$$\begin{aligned}
\delta\omega &= -\left(\frac{1}{L_\perp}\Delta\Omega(L_\perp) - \frac{1}{L'_\perp}\Delta\Omega(L'_\perp)\right)\frac{1}{Ak_BT} \\
&\approx -\omega_{ex}(T, h, L'_\perp) + \omega_{ex}(T, h, L_\perp) \\
&= L_\perp^{-d}\left(\Theta\left(u_t, u_h\right) - \alpha^{-d}\Theta\left(\alpha^{1/\nu}u_t, \alpha^{(\beta+\gamma)/\nu}u_h\right)\right) \ ,
\end{aligned} \tag{6.2}$$

the subtraction eliminating the free energy from the reference states, $\Omega(L_\perp, h^0)$ and $\Omega(L'_\perp, h^0)$, as well as the bulk contribution to the free energy at the point of interest, providing a first estimate

$$\Theta^0\left(u_t, u_h\right) \equiv \delta\omega L_\perp^d = \Theta\left(u_t, u_h\right) - \alpha^{-d}\Theta\left(\alpha^{1/\nu}u_t, \alpha^{(\beta+\gamma)/\nu}u_h\right) \ , \tag{6.3}$$

of the excess free energy scaling function Θ defined as

$$\omega_{ex}(t, \tilde{h}, L_\perp) = L_\perp^{-d}\Theta\left(u_t, u_h\right) \ , \tag{6.4}$$

with $\Theta^0 \underset{\alpha\to\infty}{\to} \Theta$. As in the case of the estimation of the Casimir scaling function, choosing $\alpha \approx 2$ the scaling function Θ^0 already provides a good estimate for the functional form of $\Theta(u_t, u_h)$. To extract a complete estimate for Θ, one can apply the iterative procedure described in chapter 4, section 4.3.5, for the Casimir scaling function, as equation 6.3 is exactly for Θ what equation 4.31 was for θ.

6.1.2 Estimation of ω_{ex} from magnetization data

We used the same magnetization data as in chapter 5 to extract the free energy scaling function (Fig. 5.1) for fully periodic boundary conditions in slab geometry. Figure 6.1a) presents the zeroth order estimate of the excess free energy scaling function obtained by integration of the

difference between magnetization data for $L_\perp = 9, L'_\perp = 20$ and $A = 3600$. We notice that, unlike the critical Casimir force, the maximum amplitude seems to be located at the bulk critical temperature.

We used a fitting Ansatz to complete our data at high values of u_t

$$\Theta(u_t) \underset{|u_t|\to\infty}{\sim} \frac{A_0}{U_0}|u_t|^{\nu(d-1)} \exp(-U_0|u_t|^\nu) \tag{6.5}$$

which proved excellent as shown in Fig.(6.1b). This functional form derives from the exponential decay expected for the critical Casimir function $\theta(u_t) \underset{|u_t|\to\infty}{\sim} A_0|u_t|^{\nu d} \exp(-U_0|u_t|^\nu)$ (Eq.4.20) (the form of Eq. 6.5 being a solution of Eq.4.15 corresponding to the asymptotic exponential behavior of θ). In the low temperature limit, we alternatively assumed that $\Theta(u_t) \approx 0$ for low values of u_t for which $\theta(u_t) \approx 0$ within the available precision. This allows one to iteratively resolve Eq.6.3 to obtain a better approximation of Θ. This procedure converged after two iterations, Fig.(6.1b), and increases the amplitude of the best estimate Θ^2 compared to the zeroth order function. Our result for Θ compares well in amplitude and width with the similar results

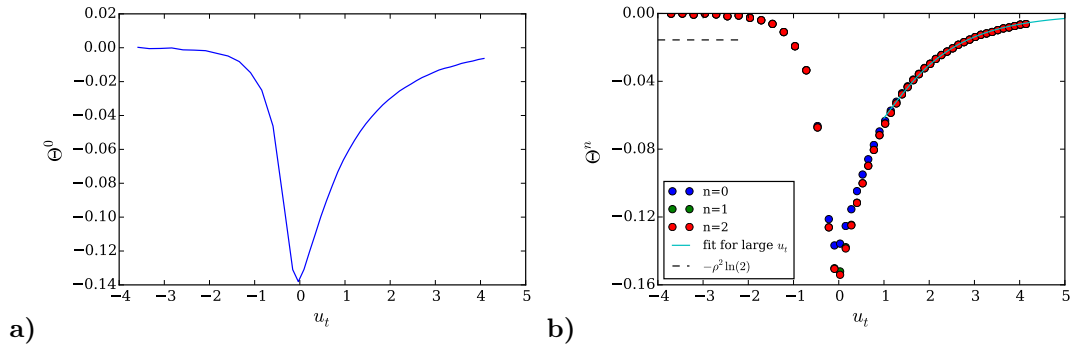

Figure 6.1: **a)** Zeroth order estimate of the scaling function of the excess free energy $\Theta^0(u_t, 0)$, obtained using two systems of thicknesses $L_\perp = 9, L'_\perp = 20$, with $A = 3600$ **b)** A better approximation Θ^n of Θ can be obtained using the iterative process described in chapter 4, converging after two iterations. Here the procedure converged after two iterations. To complete our data at high temperature, we used a n exponential fit (Eq.6.5) which proved excellent (light blue line). In ref [76], a low temperature limit $-\rho^2 \ln(2)$ (dashed black line, here $\rho = 9/60$) was found, which is not captured by our method.

of ref. [76] in which both the critical Casimir force and the excess free energy are estimated for the 3D Ising model with fully periodic boundary conditions and various aspect ratios ρ, using integration over temperature of the excess internal energy. However, in ref [76] the scaling function of the excess free energy displays a low temperature limit $\Theta(-\infty, 0) = -\rho^{d-1} \ln(2)$, which is not observed in our result (we represent it as dashed line in Fig. 6.1b). This has no influence on the estimation of the Casimir force as it is a purely ρ dependent term. This terms comes from the breaking of the positive/negative magnetization symmetry at low temperature [76, 120]. In

a finite system, both region of positive and negative magnetization of the phase space can be explored by thermal fluctuations of the order parameter, but in a thermodynamically large system ergodicity and hence symmetry is broken. Thus, an excess $-k_BT\ln(2)$ term in the total free energy is expected in a finite-size system for $T < T_c$ [120], leading to the $-\rho^{d-1}\ln(2)$ contribution to the scaling function Θ. As our procedure uses the difference in free energy $\Delta\Omega$ (Eq.6.1) between two states (t,h) and (t,h_0), the presence of a magnetic field systematically breaking the symmetry, this purely aspect-ratio depend contribution is suppressed. As the contribution $-\rho^{d-1}\ln(2)$ vanishes in the limit of slab geometry $\rho \to 0$, in view of accessing this limit our approach remains pertinent. Moreover, this ρ dependent term does not influence any quantity that we are interested in in the present work, such as the magnetization, the internal energy or the Casimir force, which are derivatives of the free energy at fixed volume or fixed aspect-ratio in the case of the Casimir force.

As for the magnetic protocol presented in chapter 5 for the computation of the critical Casimir force, no extra computational effort is required to extract an estimate of Θ for all values of h, see Fig.6.2, than to estimate it at $h = 0$ (Fig.6.1).

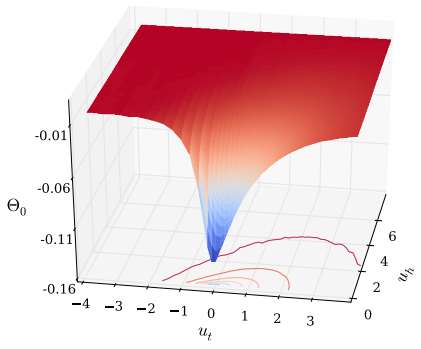

Figure 6.2: Zeroth order estimate of the scaling function of the excess free energy $\Theta^0(u_t,u_h)$ obtained using two systems of thicknesses $L_\perp = 9, L'_\perp = 20$, with $A = 3600$.

6.1.3 Excess internal energy extracted from the estimate of the excess free energy

The great advantage of having access to the excess free energy is that from it stems many other excess contributions to thermodynamic observables. In the limit of slab geometry, the derivative $\frac{\partial\Theta}{\partial u_t}\Big|_{u_h}$ gives access to the excess internal energy u_{ex} as

$$tu_{ex} = -tT\frac{\partial\omega_{ex}}{\partial T}\Big|_{h,L_\perp} = -L_\perp^{-d}u_t\frac{\partial\Theta}{\partial u_t}\Big|_{u_h}\frac{T}{T_c} \sim -L_\perp^{-d}u_t\frac{\partial\Theta}{\partial u_t}\Big|_{u_h} . \tag{6.6}$$

We use the approximation $u_{ex}\frac{T}{T_c} \sim u_{ex}$ as $\frac{T}{T_c}$ can be set to unity in the scaling limit within which we work. We stress on the fact that the presence of this approximation is implicit in

several thermodynamic relations where u_{ex} appears in this thesis, in particular in chapter 7.

We can use a numerical derivation of function Θ to estimate the excess internal energy. We present in Fig.6.3a) the estimate of u_{ex} extracted from the estimate of Θ presented in the previous section, for a system of thickness $L_\perp = 9$, using Eq.6.6.

To check the validity of our estimate of Θ, we compared the excess internal energy computed as a derivative of the excess free energy (Fig.6.3a) to an estimate of the same quantity as an excess part of the average value of the Hamiltonian per unit volume

$$u(T, h, L_\perp) = \frac{\langle \mathscr{H} \rangle}{k_B T V} \tag{6.7}$$

in units of $k_B T$ ($k_B = 1$ in our simulations), computed directly in the Monte-Carlo simulation of a system of thickness $L_\perp$. In order to give access to a simple, direct comparison with measurements of the internal energy u, we turn to the zeroth order excess internal energy

$$u^0_{ex} = -L_\perp^{1/\nu - d} \frac{\partial \Theta^0}{\partial u_t}\Big|_{u_h} , \tag{6.8}$$

corresponding to the difference in excess internal energy between systems of thicknesses $L_\perp$ and $L'_\perp$ used to compute the zeroth order scaling function Θ^0

$$u^0_{ex}(tL_\perp^{1/\nu}, 0) = u_{ex}(tL_\perp^{1/\nu}, 0) - u_{ex}(tL_\perp'^{1/\nu}, 0) . \tag{6.9}$$

This quantity should thus be equal to the difference in internal energy per particle between the two systems of thicknesses $L_\perp, L'_\perp$

$$u(T, h = 0, L_\perp) - u(T, h = 0, L'_\perp) = u_{ex}(tL_\perp^{1/\nu}, 0) - u_{ex}(tL_\perp'^{1/\nu}, 0) . \tag{6.10}$$

The comparison between $u(T, h = 0, L_\perp) - u(T, h = 0, L'_\perp)$ and $u^0_{ex}(tL_\perp^{1/\nu}, 0)$ is displayed in figure 6.3, showing excellent agreement and comforting us in the validity of our approach.

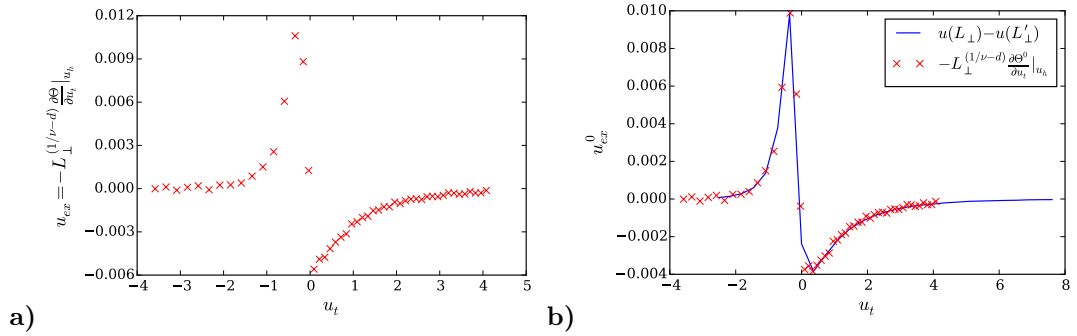

Figure 6.3: **a)** $u_{ex} = -L_\perp^{(d-1/\nu)} \frac{\partial \Theta}{\partial u_t}\Big|_{u_h}$ the excess part of the internal energy estimated for a system of dimensions $9 \times 60 \times 60$ and computed by derivation of the scaling function of the excess free energy Θ. **b)** Equivalent zeroth order quantity $u^0_{ex} = -L_\perp^{(d-1/\nu)} \frac{\partial \Theta^0}{\partial u_t}\Big|_{u_h}$ computed from the zeroth order function Θ^0 obtained using two system of thicknesses $L_\perp = 9, L'_\perp = 20$ and area $A = 3600$, compared to the variation in internal energy $u(L_\perp) - u(L'_\perp)$ between the two systems.

6.1.4 Extracting the critical Casimir force from the estimate of the excess free energy

As we have presented in chapter 4, the scaling function of the excess part of the free energy is related to the scaling function of the Casimir force by the equation

$$\theta = (d-1)\Theta - \frac{u_t}{\nu}\frac{\partial\Theta}{\partial u_t}\Big|_{u_h} - \frac{u_h(\beta+\gamma)}{\nu}\frac{\partial\Theta}{\partial u_h}\Big|_{u_t} . \tag{6.11}$$

The derivates of the scaling function of the free energy in equation 6.11 represent the excess internal energy u_{ex} expressed in units of k_BT

$$tu_{ex} = -tT\frac{\partial\omega_{ex}}{\partial T}\Big|_{h,L_\perp} = -L_\perp^{-d}u_t\frac{\partial\Theta}{\partial u_t}\Big|_{u_h}\frac{T}{T_c} \approx -L_\perp^{-d}u_t\frac{\partial\Theta}{\partial u_t}\Big|_{u_h} , \tag{6.12}$$

and excess magnetization

$$\tilde{h}m_{ex} = -\tilde{h}\frac{\partial\omega_{ex}}{\partial\tilde{h}}\Big|_{T,L_\perp} = -L_\perp^{-d}u_h\frac{\partial\Theta}{\partial u_h}\Big|_{u_t} , \tag{6.13}$$

so that Casimir force, excess free energy and excess magnetization are related by

$$\frac{f_c}{k_BT} = (d-1)\omega_{ex} + t\nu^{-1}u_{ex} + \tilde{h}\frac{\beta+\gamma}{\nu}m_{ex} . \tag{6.14}$$

Hence our estimate of $\Theta(t,h)$ extracted from magnetization data can be used to build up an equivalent estimate of the Casimir function θ using equation 6.11.

In the previous section, we have computed u_{ex} and u_{ex}^0 by derivation of Θ and Θ^0 with respect to u_t. We can now construct a zeroth order estimate θ^0 using

$$\theta^0 = (d-1)\Theta^0 - \frac{u_t}{\nu}\frac{\partial\Theta^0}{\partial u_t}\Big|_{u_h} - \frac{u_h(\beta+\gamma)}{\nu}\frac{\partial\Theta^0}{\partial u_h}\Big|_{u_t} . \tag{6.15}$$

and the final estimate θ of the scaling function of the critical Casimir force using Eq.6.11 (at $u_h = 0$, the excess magnetization does not contribute). In figure 6.4 we present θ^0 and θ constructed in this way and the contributions of the excess free energy and excess internal energy to these functions. We find excellent agreement with the independent results obtained for the same system dimensions using the adiabatic coupling approach outlined in chapter 4, both for θ^0 and θ, confirming the validity of our approach.

The rather pronounced noise in the wings of θ and θ^0 is due to the difficulty of estimating of the derivative of Θ and Θ^0 in these regions, the noise on the derivative being magnified by the factor u_t in Eq.6.11. We stress the fact that estimating the critical amplitude from the estimate of Θ or θ is strictly equivalent as $\Theta(0,0) = \Delta = (1/2)\theta(0,0)$, given that neither u_{ex} nor m_{ex} contribute to θ at the bulk critical point. Thus, the $(d-1)\Theta$ contribution to θ naturally dominates close to the bulk critical point and measuring the Casimir force f_c amounts to measuring the excess part of the free energy. On the other hand, far from the critical point, the excess internal energy contribution $tu_{ex} = -L_\perp^{-d}u_t\frac{\partial\Theta}{\partial u_t}\Big|_{u_h}$ becomes dominant.

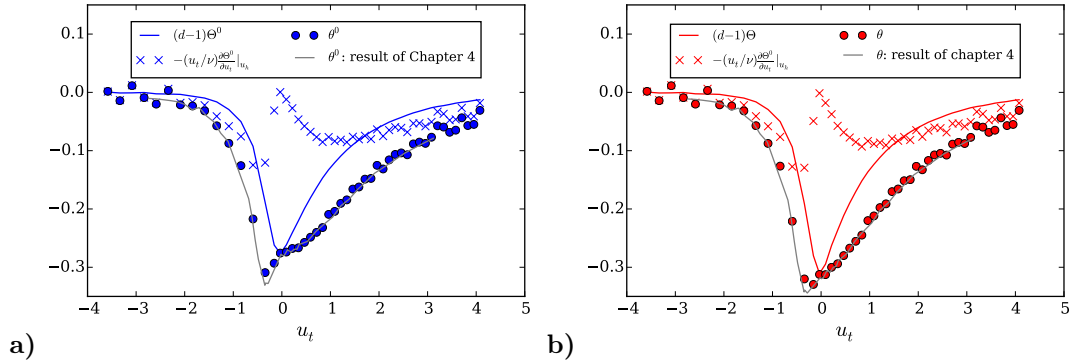

Figure 6.4: **a)** From the zeroth order estimate of the scaling function of the excess free energy Θ^0 we can construct the zeroth order scaling function of the critical Casimir force θ^0 using Eq.6.15. θ^0 (blue points) results from the sum of a contribution from the excess free energy (blue line) and excess internal energy (blue crosses). We get an excellent agreement between this approach and the coupling parameter one described in chapter 4 for the same system sizes (grey line). **b)** From this zeroth order scaling function, a better estimate Θ has been extracted, and a corresponding better estimate of θ can be constructed using Eq.6.11. θ (red points) results from the sum of a contribution from the excess free energy (red line) and excess internal energy (red crosses). This result for θ again compares very well with the best estimate of θ independently obtained in chapter 4 (grey line).

6.2 Computing the excess free energy by integration of the critical Casimir force

In the case on non-periodic confining boundary conditions, surface contributions to the free energy ω_{surf} come in the way of the previous approach as it is not an extensive contribution to the free energy. However, we can take advantage of the results of chapter 5 in which we have accurately computed the scaling function of the critical Casimir force. We have used Eq. 6.11 to reconstruct the scaling function of the Casimir force θ from the scaling function of the excess part of the free energy Θ. The reverse path can actually be taken: Eq.6.11 can be solved and the scaling function of the excess free energy Θ can be extracted from that of the Casimir force θ using

$$\Theta(u_t, u_h) = \int_1^\infty s^{-d}\theta(u_t s^{1/\nu}, u_h s^{(\beta+\gamma)/\nu})\mathrm{d}s \ , \tag{6.16}$$

which is a generalization to non-zero field h of the solution proposed in ref. [121]. This solution assumes that $\lim_{u_t\to\pm\infty}\Theta(u_t, u_h) = 0$ and $\lim_{u_h\to\pm\infty}\Theta(u_t, u_h) = 0$. In the limit $A \to \infty$, the function Θ is not analytic as the slab system undergoes a 2D phase transition at the apparent critical temperature $T = T_c(L_\perp)$ (see section 2.2.4 and ref. [3, 76]). We expect that this does not prevent us to solve Eq.6.11 as Θ and its derivatives involved in Eq.6.11 are still continuous and finite

functions. The present precision on our data did not allow the observation of a signature of this 2D transition.

The evolution of Θ at $h = 0$ can be deduced without any knowledge of θ at non-zero values of h, as Eq.6.11 reduces to

$$\theta(u_t, 0) = (d-1)\Theta(u_t, 0) - \frac{u_t}{\nu}\frac{\partial\Theta}{\partial u_t}\Big|_{u_h}(u_t, 0) \ , \tag{6.17}$$

which can be solved solely with knowledge of $\theta(u_t, 0)$ using

$$\Theta(u_t, 0) = \int_1^\infty s^{-d}\theta(u_t s^{1/\nu}, 0)\mathrm{d}s \ . \tag{6.18}$$

Equivalently, at the critical temperature

$$\theta(0, u_h) = (d-1)\Theta(0, u_h) - \frac{u_h(\beta+\gamma)}{\nu}\frac{\partial\Theta}{\partial u_h}\Big|_{u_t}(0, u_h) \ , \tag{6.19}$$

which can be solved using

$$\Theta(0, u_h) = \int_1^\infty s^{-d}\theta(0, u_h s^{(\beta+\gamma)/\nu})\mathrm{d}s \ . \tag{6.20}$$

A first observation, that is obvious from Eq.6.17, is that

$$\Theta(0, 0) = \frac{1}{d-1}\theta(0, 0) = \Delta \ , \tag{6.21}$$

with Δ the universal scaling amplitude of the critical Casimir force. This fixed point forces one to perform the integration of Eq. 6.18 (respectively Eq. 6.20) in two times: one for positive values of u_t (respectively u_h) and one for negative values. Moreover, the integral of Eq. 6.18 (respectively Eq. 6.20) must be truncated up to a reference state u_t^0 (respectively u_h^0) rewriting Eq. 6.18

$$\begin{aligned}\Theta(u_t) &= s_0^{1-d}\Theta(u_t s_0^{1/\nu}, 0) + \int_1^{s_0} s^{-d}\theta(u_t s^{1/\nu})\mathrm{d}s \\ &= \left(\frac{u_t^0}{u_t}\right)^{\nu(1-d)}\Theta(u_t^0, 0) + \int_1^{s_0} s^{-d}\theta(u_t s^{1/\nu})\mathrm{d}s \ ,\end{aligned} \tag{6.22}$$

with $s_0 = \left(\frac{u_t^0}{u_t}\right)^\nu$. An exact application of Eq. 6.22 requires the knowledge of $\Theta(u_t^0)$ at the reference point, which of course we do not know a priori. We notice that the influence of this reference value in Eq.6.22 is proportional to $u_t^{\nu(d-1)}$, so that any error on the determination of $\Theta(u_t^0)$ will be smoothed out when approaching the fixed point $u_t \to 0$. An error on the determination of the reference $\Theta(u_t^0)$ will principally affect Θ close to u_t^0 itself.

If a reference state u_t^0 or u_h^0 at which the Casimir scaling function can safely be considered zero is available, we make the assumption that the reference value $\Theta(u_t^0, 0)$ or $\Theta(0, u_h^0)$ can also safely be considered zero. This is consistent with the solutions provided by Eq.6.18 (respectively 6.20) which imposes that for sufficiently large values of u_t^0 (resp. u_h^0) for which θ decays monotonically towards zero: $\theta(u_t^0, 0) \geq (d-1)\Theta(u_t^0, 0)$ (resp. $\theta(0, u_h^0) \geq (d-1)\Theta(0, u_h^0)$). This can be easily shown: in the case of a monotonously decaying θ (for example at $h = 0$)

$$\theta(u_t^0 s^{1/\nu}, 0) \leq \theta(u_t^0, 0) \ , \tag{6.23}$$

for $s \geq 1$, leading to

$$\Theta(u_t^0, 0) = \int_1^\infty s^{-d}\theta(u_t^0 s^{1/\nu}, 0)\mathrm{d}s \leq \int_1^\infty s^{-d}\theta(u_t^0, 0)\mathrm{d}s = \frac{\theta(u_t^0, 0)}{d-1} \ , \tag{6.24}$$

the demonstration for $\theta(0, u_h^0) \geq (d-1)\Theta(0, u_h^0)$ being equivalent.

6.2.1 Fully periodic boundary conditions

As a first test of the present approach, we compare in figure 6.5 the estimate of $\Theta(u_t, 0)$ obtained by integration of the magnetization described in section 6.1.2 to the result given by integration of the critical Casimir function θ (Eq.6.18) using the data presented in chapter 4 (Fig.4.4). These two independent estimates show excellent agreement. Once again, the present approach does not capture the non-zero limit $-\rho^{d-1}\ln(2)$, as it assumes a vanishing Θ far from the critical point, and thus is relevant for the slab geometry limit $\rho \to 0$. The only notable difference between the two approaches compared in Fig. 6.5 is in the limit of large u_t where, as we stated, the integration of θ suffers from the greatest error due to the determination of a reference value $\Theta(u_t^0, 0)$. As in the previous approach, we completed our data in the high temperature region using the exponential decay expected for $\theta_{fit}(u_t, 0) = A_{fit}|u_t|^{\nu d}\exp(-U_{fit}|u_t|^\nu)$ (Eq.4.20) and accordingly determined the reference state for the integration of Eq.6.22 as $\Theta(u_t^0, 0) = \frac{A_{fit}}{U_{fit}}|u_t^0|^{\nu(d-1)}\exp(-U_{fit}|u_t^0|^\nu)$, with u_t^0 the highest available value for u_t.

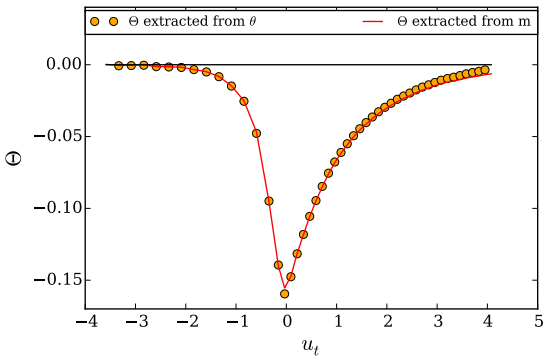

Figure 6.5: Scaling function of the excess free energy Θ for fully periodic boundary conditions obtained by integration of the magnetization (red line), see section 6.1.2 (Eq.6.2), compared to the result given by integration of scaling function of the Casimir force scaling function θ (yellow dots) using Eq.6.18 and data of chapter 4 for θ.

6.2.2 Fixed $(++)$ and $(+-)$ boundary conditions, $h = 0$

We extended our study to the case of fixed $(++)$ and $(+-)$ boundary conditions in the confining z direction, taking advantage of the data for the critical Casimir force presented in chapter 5. In figure 6.6, we present our best estimates for the scaling function θ_{++} and θ_{+-} of the critical Casimir force (see figures 5.3 and 5.5). These functions were obtained using our magnetic protocol in systems of dimension $\ell = 9.5$, $\alpha\ell = 19.5$, $A = 3600$ and after performing two iterations of the procedure described in chapter 4, section 4.3.5, to suppress the contribution of the system of thickness $\alpha\ell = 19.5$. To account for the rather important corrections to scaling on the

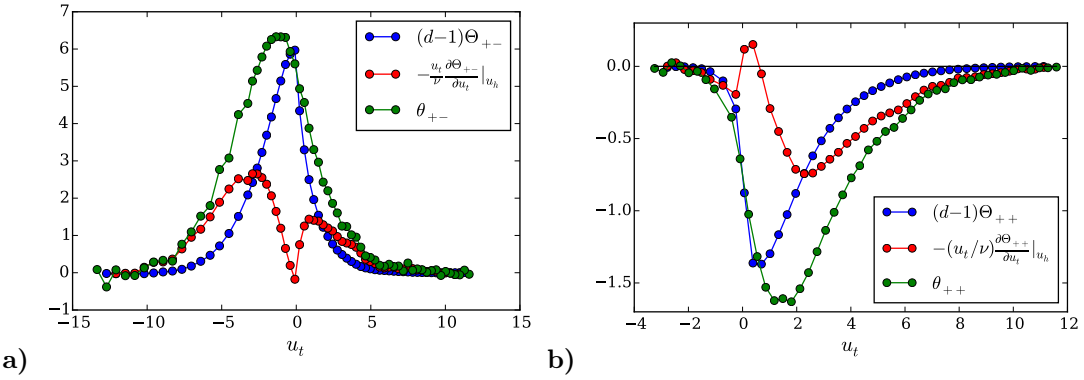

a) **b)**

Figure 6.6: Critical Casimir force scaling function $\theta_{+\pm}$ for fixed $(+-)$ **(a)** or $(++)$ **(b)** boundary conditions, estimated with the magnetic protocol of chapter 5 (green dots and line). Using Eq. 6.12, we estimated the corresponding scaling functions $\Theta_{+\pm}$ of the excess free energy. We can thus display the contributions to $\theta_{+\pm}$ (Eq. 6.11) of the excess free energy scaling function $(d-1)\Theta_{+\pm}$ (blue dots and line) and its derivative $-\frac{u_t}{\nu}\frac{\partial\Theta_{+\pm}}{\partial u_t}\Big|_{u_h}$ (red dots and line) . Amplitudes of functions $\theta_{+\pm}$ were rescaled to $\theta_{+-}(0,0) = 2\Delta_{+-} = 5.42(4)$ and $\theta_{++}(0,0) = 2\Delta_{++} = -0.75(6)$ [3] to account for corrections to scaling.

amplitude of the scaling functions, we rescaled them to the values $\theta_{+-}(0,0) = 2\Delta_{+-} = 5.42(4)$ and $\theta_{++}(0,0) = 2\Delta_{++} = -0.75(6)$ obtained in ref. [3] after extensive study of these corrections. Using Eq. 6.22 and the hypothesis that $\Theta_{+\pm}(u_t^0, 0) \approx 0$, we computed the corresponding scaling functions of the excess free energy $\Theta_{+\pm}$. Corrections affecting the scaling variable u_t are neglected here but could affect the behavior of $\Theta_{+\pm}$. The present results are thus preliminary.

We display in figure 6.6 the contributions (Eq. 6.11) to the functions $\theta_{+\pm}$ of the excess free energy scaling functions $(d-1)\Theta_{+\pm}$ and of their derivatives $-\frac{u_t}{\nu}\frac{\partial\Theta_{+\pm}}{\partial u_t}\Big|_{u_h}$ (which amounts to contributions of the excess internal energy, see Eq. 6.12). Of course, the sum of these two contributions amounts exactly to $\theta_{+\pm}$ as they have been consistently built as solutions of Eq. 6.11. As discussed in the case of fully periodic boundary conditions, the fixed point $\theta_{+\pm}(0,0) = (d-1)\Theta_{+\pm}(0,0)$ imposes that the critical Casimir force is dominated by the contribution of the

free energy close to the critical point. Far from the critical temperature, the contribution related to the excess internal energy becomes predominant.

6.2.3 Fixed (++) boundary conditions with non zero field

In section 5.6.2 of chapter 5, we have seen that a Casimir force an order of magnitude bigger than at zero magnetic field could be obtained at the critical temperature by imposing a non-zero magnetic field opposing the confining boundary conditions (++) (Fig. 5.10). Corrections to scaling were taken into account by introducing an effective length $\ell_{eff} = \ell + \delta\ell$, $\delta\ell$ being used as a fitting parameter to obtain a collapse of data obtained for three different sets of systems sizes (see section 5.6.2). Taking into account these corrections to the scaling limit, we have extracted an estimate of the free energy scaling function Θ_{++} from our best estimate of θ_{++} using Eq.6.20. We display in figure 6.7 the contributions (Eq. 6.11) to the function θ_{++} of the excess free energy scaling function $(d-1)\Theta_{++}$ and of its derivative $-u_h \frac{\beta+\gamma}{\nu} \frac{\partial \Theta_{++}}{\partial u_h}\Big|_{u_t}$, which amounts to a contribution of the excess magnetization (Eq. 6.13). In section 5.6.2, we mentioned that the large amplitude of the Casimir force in the strong negative magnetic field region could be intuitively understood by looking at magnetization curves of Fig.5.7. We see in figure 6.7 that indeed, for strong magnetic fields, the contribution of the excess magnetization clearly dominates. Thus, in this region access to the excess magnetization leads already to an approximation for the Casimir effect without access to the free energy.

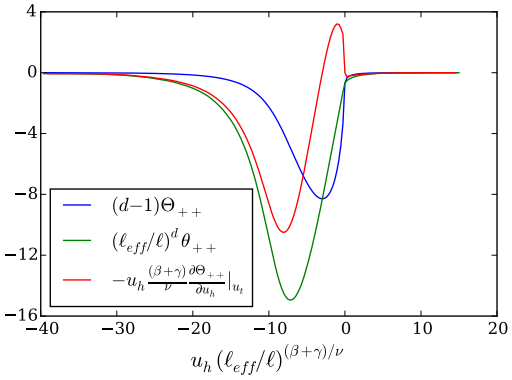

Figure 6.7: Critical Casimir force scaling function θ_{++} for fixed (++) boundary conditions at $T = T_c$ with non-zero magnetic field spanning positive and negative values (green curve), estimated with the magnetic protocol of chapter 5 (Fig. 5.10), using an effective length ℓ_{eff} to capture corrections to scaling (see section 5.6.2). From this function, the scaling function of the excess free energy Θ_{++} can be extracted (Eq.6.20). We can thus display the contributions to the function θ_{++} (Eq. 6.11) of the excess free energy scaling function $(d-1)\Theta_{++}$ (blue curve) and its derivative $-u_h \frac{\beta+\gamma}{\nu} \frac{\partial \Theta_{++}}{\partial u_h}\Big|_{u_t}$ (red curve), which amounts to a contribution from the excess magnetization (Eq. 6.13).

6.3 Conclusion

We have solved Eq. 6.11 in order to extract the scaling function Θ of the excess free energy from estimates of the scaling function of the critical Casimir force in the 3D Ising system with fully periodic and fixed $(+\pm)$ boundary conditions. This provided insights into the relative importance of contributions of the excess free energy, internal energy and magnetization to the critical Casimir force (Eq. 6.14). Moreover, the knowledge of the scaling function Θ gives in principle access to all excess quantities of observables deriving from it: this proved to be efficient in the case of the excess internal energy u_{ex} (Fig.6.3), a result that we will exploit in chapter 7. We will also see in chapter 7 that the knowledge of the scaling function of the excess free energy is necessary to study the anisotropy of the excess pressure which arises in confined slab geometry.

We have seen that solving Eq. 6.11, as well as deriving Θ directly from magnetization data in the case of fully periodic boundary conditions, could not capture the low temperature limit $-\rho^2 \ln(2)$ (Fig. 6.1) expected for non-zero aspect ratios [76], because of the cancellation of this term in the subtraction process between the chosen state (T, h) and a reference state (T, h_0). Thus, our results are valid when approaching the limit of slab geometry $\rho \to 0$. However, the study of the dependency on the aspect ratio of the critical Casimir force and the excess free energy, requiring data for various aspect ratios not explored in the present work, is an interesting perspective, which has already been explored for fully periodic boundary conditions in ref. [76]. The relation of Eq.6.11 linking free energy and Casimir force can be extended to include this aspect-ratio dependency [76, 118] by including a dependency on the aspect ratio in the excess free energy density scaling function

$$\omega_{ex}(t, L_\perp, \rho) = L_\perp^{-d} \Theta_\rho \left(u_t, \rho\right) \ , \tag{6.25}$$

the scaling function of the critical Casimir force becoming

$$\theta_\rho(u_t, u_h, \rho) = (d-1)\Theta_\rho - \frac{u_t}{\nu} \frac{\partial \Theta_\rho}{\partial u_t}\Big|_{u_h,\rho} - \frac{u_h(\beta+\gamma)}{\nu} \frac{\partial \Theta_\rho}{\partial u_h}\Big|_{u_t,\rho} - \rho \frac{\partial \Theta_\rho}{\partial \rho}\Big|_{u_t,u_h} \ , \tag{6.26}$$

with of course the limits $\theta_\rho \underset{\rho \to 0}{\to} \theta$ and $\Theta_\rho \underset{\rho \to 0}{\to} \Theta$.

Chapter 7

The Critical Casimir Force in a Lennard-Jones Binary Mixture

The Lennard-Jones model of fluids offers the possibility for simulations more closely related to experiments in liquid systems, than a simulation of the Ising model. Typically, in a Lennard-Jones fluid, the pressure is more naturally defined than in a magnetic lattice model. As stressed in previous chapters, we are particularly interested in critical binary mixtures, the demixing transition belonging to the Ising universality class and having been used for measurements of the critical Casimir force [5]. The order parameter is the composition of the mixture, equivalent to the magnetization in a magnetic system, particles being either of species A or B in one case, and spins being up or down in the other. The "magnetic" degree of freedom which is the species of the particles is coupled to the positional degrees of freedom, conveying a critical Casimir effect close to the demixing critical point. Complex geometries, fluctuations of the force and out-of-equilibrium measurements would be accessible to Monte Carlo or molecular dynamics simulations of such a fluid model.

To our knowledge, the only attempt to capture a critical Casimir effect through simulation of a fluid system was published in ref. [62]. In this work, wetting experiments were simulated using a Lennard-Jones symmetrical binary mixture confined in slab geometry between a simple hard wall and an attractive hard wall. The attractive wall is responsible for the formation of a wetting layer of binary mixture, similarly to van der Waals interaction in wetting experiments introduced in chapter 4. The thickness of this layer is then affected by the critical Casimir force arising close to the demixing transition. This effect was captured qualitatively in ref. [62] but did not give rise to a measurement of the critical Casimir scaling function.

In this chapter, we show preliminary results for the direct measurement of the critical Casimir force through Semi-Grand Canonical simulations of a symmetrical binary Lennard-Jones fluid. Convincing agreement with data obtained in the Ising model for the excess internal energy is found. Moreover, we make a theoretical prediction for a pressure anisotropy in the critical

pressure in slab geometry and for the relation between chemical potential and internal energy, for which we find confirmation in our numerical approach.

7.1 Lennard-Jones binary mixtures

7.1.1 Simple Lennard-Jones fluid

We consider a Lennard-Jones fluid confined in a three dimensional cell of thickness $L_\perp$ and area $A = L_\parallel \times L_\parallel$, figure 7.1 showing a snapshot of the simulation box. The boundary conditions are set periodic in all directions. A great variety of confining boundary conditions in the z direction could be studied, for example closed with a steeply repulsive ($\sim r^{-12}$) interaction or by fixing particles on the boundary. We will restrict ourselves to the fully periodic case in this initial study. The snapshot of figure 7.1 shows two different species of particles but for simplicity we

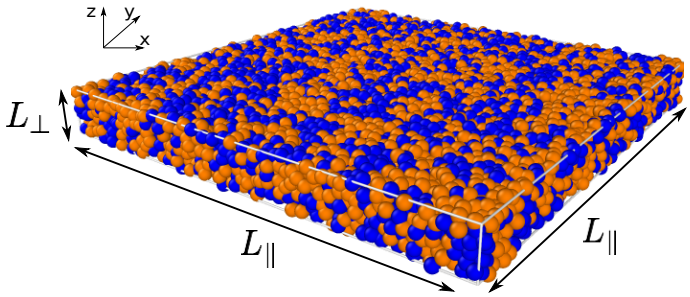

Figure 7.1: Snapshot of the simulation box used in this work, with two particle types and $L_\perp = 5\sigma$ and $L_\parallel = 60\sigma$.

will first describe the case of a one component fluid. The system is composed of N particles of diameter $\sim \sigma$, interacting one with another through a truncated and shifted Lennard-Jones potential. The standard Lennard-Jones potential is defined as:

$$v_{LJ}(r) = 4\epsilon \left[\left(\frac{\sigma}{r}\right)^{12} - \left(\frac{\sigma}{r}\right)^{6} \right] , \tag{7.1}$$

where r is the separation between the centers of the two particles, σ is a typical range of the interaction at which it turns from attractive to repulsive and ϵ is a typical interaction energy which sets the depth of the attractive potential, see Fig.7.2. The attractive part represents the dominant long range van der Waals-London interaction between simple spherical particles and the repulsive part the strongly repulsive short range interaction due to the Pauli principle opposing superposition (the steep r^{-12} form was chosen for computational convenience as it is the square of the attractive part dependency) [72]. For computational reasons, the potential $v(r)$ we used is a truncated and shifted version of the standard Lennard-Jones one. The potential is

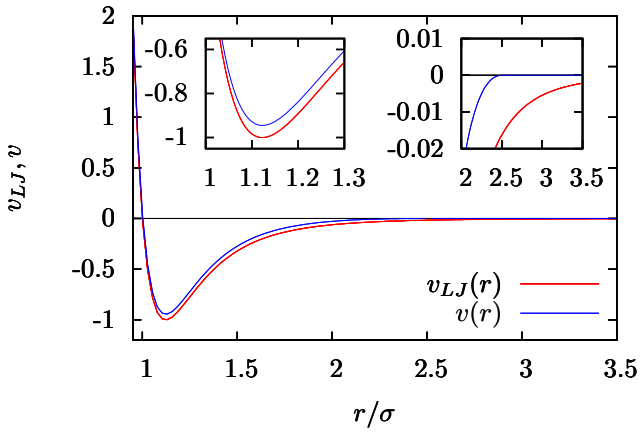

Figure 7.2: Lennard-Jones potential v_{LJ} and truncated and shifted potential v used in the simulations, here with $r_c = 2.5\sigma$ and $\epsilon = 1$.

put to zero when the separation between particle exceeds a cut-off length $r > r_c$, but with the constraint that the potential stays continuous and of continuous derivative at r_c

$$v(r) = \begin{cases} v_{LJ}(r) - v_{LJ}(r_c) - \dfrac{1}{2r_c}\dfrac{dv_{LJ}}{dr}(r_c)\left(r^2 - r_c^2\right) & \text{if } r \leq r_c \ , \\ 0 & \text{if } r > r_c \ . \end{cases} \tag{7.2}$$

Figure 7.2 shows how $v(r)$ with $r_c = 2.5\sigma$ differs from $v_{LJ}(r)$, the resulting amplitude shift being very small, and the two potentials being extremely similar. For simplicity, we used units of energy such that $\epsilon = 1$, and of length such that $\sigma = 1$.

7.1.2 Symmetrical binary mixture

To simulate a binary mixture, the Lennard-Jones potential is modified to take into account two species A and B with different interaction energy ϵ_{ij} and interaction range σ_{ij}, so that the Lennard-Jones potential becomes

$$v_{LJ}^{i,j}(r) = 4\epsilon_{ij}\left[\left(\frac{\sigma_{ij}}{r}\right)^{12} - \left(\frac{\sigma_{ij}}{r}\right)^{6}\right] \ , \tag{7.3}$$

on which the same regularization as in Eq.7.2 is made to obtain the simulation potential $v_{ij}(r)$. In symmetrical mixtures the parameters of the potential between identical particles are the same $\sigma_{AA} = \sigma_{BB} = \sigma$ and $\epsilon_{AA} = \epsilon_{BB} = \epsilon$. The binary nature of the fluid then comes from the unlike particles interaction $\sigma_{AB} = s\sigma$ and $\epsilon_{AB} = e\epsilon$, where s and e are parameters either bigger or smaller than 1. Of course, $s = e = 1$ is the simple Lennard-Jones case and in the limit cases $s = 0$ or $e = 0$ we obtain two non interacting simple Lennard-Jones fluids. In the following,

we restrict our study to the case of identical particle sizes $s = 1$ and interaction between unlike particles reduced by a factor of one half, $e = 1/2$.

7.1.3 The Semi-Grand Canonical ensemble

A Canonical binary Lennard-Jones fluid of $N = N_A + N_B$ particles confined in a volume V is described by four thermodynamic variables (T, V, N_A, N_B) and the internal energy is given by the Hamiltonian

$$\mathscr{H}_{int} = \sum_{i<j}^{N_A} v_{AA}(r_{ij}) + \sum_{i<j}^{N_B} v_{BB}(r_{ij}) + \sum_{i=1}^{N_A}\sum_{j=1}^{N_B} v_{AB}(r_{ij}) \ , \tag{7.4}$$

where v_{ij} is the shifted Lennard-Jones potential described in the previous section for a symmetrical mixture. The number of particles can be allowed to fluctuate in the Grand-Canonical ensemble, in which the full Hamiltonian includes two new terms

$$\mathscr{H} = \mathscr{H}_{int} - \mu_A N_A - \mu_B N_B \ , \tag{7.5}$$

with μ_A, μ_B chemical potentials associated with each type of particle and measured in units of ϵ [122–125]. The relevant Grand-Canonical thermodynamic variables are (T, V, μ_A, μ_B), so that the differential of the Grand Potential $\Phi(T, V, \mu_A, \mu_B)$ reads

$$\mathrm{d}\Phi = -S\mathrm{d}T - P\mathrm{d}V - N_A\mathrm{d}\mu_\mathrm{A} - N_B\mathrm{d}\mu_\mathrm{B} \ .$$

Defining $\mu = (\mu_A + \mu_B)/2$, $\mu_{AB} = (\mu_A - \mu_B)/2$ and $\Delta N = N_A - N_B$ we can perform a change of variables so that the Hamiltonian can be rewritten

$$\mathscr{H} = \mathscr{H}_{int} - \mu N - \mu_{AB}\Delta N \ . \tag{7.6}$$

and the differential of the Grand Potential

$$\mathrm{d}\Phi = -S\mathrm{d}T - P\mathrm{d}V - N\mathrm{d}\mu - \Delta N\mathrm{d}\mu_{AB} \ ,$$

showing that the Grand-Canonical ensemble can be equivalently described by the set of variables (T, V, μ, μ_{AB}), the chemical potential μ being the conjugate variable to the total number of particles and μ_{AB} to the composition of the mixture.

A Grand-Canonical simulation requires an efficient way of simulating a particle reservoir, inserting or suppressing particles in the simulation cell, an obviously difficult step in the case of a dense fluid. If one is interested in the demixing transition, this difficulty can be circumvented by working in the numerically relevant Semi-Grand Canonical ensemble, in which the total number of particles is fixed but its composition fluctuates [124, 125]. The Semi-Grand Canonical ensemble is described by the variables (T, V, N, μ_{AB}), so that the Semi-Grand Canonical potential is differentiated as

$$\mathrm{d}\Omega_{sgc} = -S\mathrm{d}T - P\mathrm{d}V + \mu\mathrm{dN} - \Delta\mathrm{N}\mathrm{d}\mu_{AB} \ .$$

The total number of particles is fixed but the nature of a particle can change during the simulation so that the $A-B$ symmetry can be broken and a transition between mixed to either $A-$rich or $B-$rich phase can occur, characterized by the "mixing" order parameter $\Delta N/N$. This transition can be driven by temperature but of course also by a symmetry breaking field, that is a non zero μ_{AB} so that one species is favored over the other by the A-B "color" reservoir. Nevertheless, we will fix in the following $\mu_{AB} = 0$ and keep a fully symmetric system with respect to $A-B$ exchange.

7.1.4 Linking the Semi-Grand Canonical fluid with the Ising model

We have already seen in the previous chapters that the demixing transition of binary mixtures belongs to the universality class of the Ising model, but what is the best thermodynamic ensemble to directly compare results computed in both systems ? The Ising model is equivalent to a lattice gas, an up spin representing an occupied spot and a down spin a vacancy, and to a lattice binary fluid, an up spin being a particle of type A and a down spin a particle B (see section 1.2.2). We can hence draw a qualitative parallel between the Lennard-Jones binary fluid and a magnetic system. In the case where the typical size of particles do not depend on its nature, $\sigma_{ij} = \sigma$, the influence of the nature of particle on the potential v_{ij} can be factorized

$$v_{ij}(r) = \frac{\epsilon_{ij}}{\epsilon} v(r) \ . \tag{7.7}$$

We have chosen $2\epsilon_{AB} = \epsilon_{AA} = \epsilon_{BB} = \epsilon$, which can be written in a compact way as

$$\epsilon_{ij} = \frac{\epsilon}{4}(S_i S_j + 3) \ , \tag{7.8}$$

where $S_i = 1$ if the particle is of type A and $S_j = -1$ if it is of type B. Thus

$$v_{ij}(r) = \frac{1}{4}(S_i S_j + 3) v(r) \ , \tag{7.9}$$

factorizing the binary fluid potential in a Lennard-Jones simple fluid part and an Ising like term. The Hamiltonian then reads

$$\mathscr{H}_{int} = \sum_{i<j}^{N} \frac{1}{4}(S_i S_j + 3) v(r_{ij}) \ , \tag{7.10}$$

and we can see our binary mixture as a simple model for ferrofluid, a Lennard-Jones fluid with an internal "magnetic" degree of freedom S_i which can be updated using a Metropolis type algorithm. If one considers a frozen positional configuration of the system, it is equivalent to an Ising system with quenched disorder and further neighbor interactions over a length scale 2.5σ. The mixing order parameter

$$\frac{\Delta N}{N} = \frac{1}{N} \sum_{i}^{N} S_i = m \ , \tag{7.11}$$

is straightforwardly related to an equivalent magnetization m, the difference in chemical potentials μ_{AB} playing the equivalent role of a magnetic field h. This analogy can also be seen when comparing the differential of the Semi-Grand Canonical potential, depending on (T, V, N, μ_{AB}),

$$\mathrm{d}\Omega_{sgc} = -S\mathrm{d}T - P\mathrm{d}V + \mu\mathrm{dN} - \Delta\mathrm{N}\mathrm{d}\mu_{AB} \ , \tag{7.12}$$

to the corresponding Ising free energy, depending on (T, V, N, h),

$$\mathrm{d}\Omega = -S\mathrm{d}T - P\mathrm{d}V + \mu\mathrm{dN} - \mathrm{Mdh} \ . \tag{7.13}$$

As mentioned in chapter 4, in the case of the lattice Ising model the variable N was omitted as the lattice imposes the density $n = N/V$. Strictly speaking this fourth variable is necessary and working at constant density makes the magnetic model thermodynamically equivalent to a simple fluid with fixed interaction range σ or, as in the present case, to a binary mixture with fixed volume and total number of particles, thus fixed total density, which is the case in the Semi-Grand Canonical ensemble.

The Semi-Grand Canonical ensemble hence appears as the most suitable ensemble to compute excess quantities in a Lennard-Jones simulation directly related to the results obtained in the Ising model in the previous chapters. A Grand-Canonical simulation of a binary mixture would be more directly related to the phenomenology of the Blume-Capel model (see section 4.3.7), in which a spin can take values $S_i = -1, 0, +1$, being equivalent (on a lattice) to A particle, B particle or the absence of a particle. The number of non zero spins, equivalent to the total number of particles N, being controlled by a parameter D, equivalent to the chemical potential μ.

7.1.5 Definition of the confinement force

In the Semi-Grand Canonical ensemble at fixed density n, the number of particles is controlled by the volume and the differential of the potential becomes

$$\mathrm{d}\Omega_{sgc} = -S\mathrm{d}T - (P - \mu n)\mathrm{d}V - \Delta N\mathrm{d}\mu_{AB} \ . \tag{7.14}$$

so that $P - \mu n$ is the natural conjugate variable to the volume. In chapters 4 and 5, to compute the critical Casimir force in the Ising model, we found access to the variation of free energy when adding or removing a layer of spins, performing a variation

$$(T, V, N, h) \ \rightarrow \ (T, V + \delta V, N + \delta N, h)$$

with $\mathrm{n} = \mathrm{N}/\mathrm{V} = (\mathrm{N} + \delta\mathrm{N})/(\mathrm{V} + \delta\mathrm{V})$ fixed. The corresponding variation of the free energy $\delta\Omega$ was thus implicitly related to the quantity $P - \mu n$ as

$$\delta\Omega = -P\delta V + \mu\delta N = (\mu n - P)\delta V \ , \tag{7.15}$$

and we expect the critical Casimir force in a Semi-Grand Canonical fluid to be contained in the generalized pressure $\tilde{P} = P - \mu n$.

At the beginning of chapter 4, we gave a quick introduction to measurements of the critical Casimir force. In wetting experiments, the confinement of critical fluctuations is realized by the formation of a wetting film. The thickness of such a film is determined by the competition between different contributions, for example: a gravitational contribution to the chemical potential, or coming from a temperature gradient, van der Waals interactions with the substrate and, of course, the critical Casimir force. All these contributions could be referred to as "confinement forces", as they all control the confinement of the system. We particularize the critical Casimir force as it is a purely critical, universal effect. In our simulations, the confinement is imposed and we measure the resulting forces instead of indirectly deducing them from the equilibrium volume of the system. Nevertheless, there is no reason a priori to consider that non critical confinement forces should not arise. We have discussed in previous chapters that fixed boundary conditions can impose topological constrains on the local composition (equivalently the magnetization) of the system. The boundaries not only affect the critical fluctuations but can also give rise to non critical contributions to the free energy. In the Ising model, we have considered that the periodic boundary conditions did not foster any non critical confinement force nor surface term and that fixed $(++)$ and $(+-)$ boundary conditions only gave rise to surface tension contributions. However, as it has been exploited in ref. [62] to mimic a wetting experiment in a Lennard-Jones simulation, the presence of a wall can induce a non critical confinement force, in addition to the critical Casimir force. In a dense fluid, the density pair correlation function decays in an oscillatory way [124] and in very small systems the boundary conditions can cut-off these oscillations, inducing confinement effects in the pressure and internal energy, which themselves oscillate with system size [126, 127]. We will see in the following that for particularly small system thicknesses, even periodic boundary conditions give rise to such non critical confinement effects [126] in both the pressure (see for example figure 7.7) and the internal energy (see for example figure 7.5), due to the incommensurability of the oscillations in the pair correlation function with the system size.

7.2 Semi-Grand Canonical simulation of a binary mixture

7.2.1 Simulation method

We simulated the symmetrical Lennard-Jones binary mixture described above in the semi-grand canonical ensemble with fully periodic boundary conditions. The simulations were performed by Francesco Puosi, post-doctoral researcher at the Physics Laboratory of the E.N.S. de Lyon, using the LAMMPS package for parallelized molecular simulations [128] and taking advantage of the numerical resources of the PSMN in Lyon [22].

The positions of the particles were updated using molecular dynamics using the Nosé-Hoover thermostat. We used a quite small time step of $10^{-5} \times \tau$, with $\tau = \sigma\sqrt{m/\epsilon} = 1$ the simulation

characteristic time scale (typically, using parameters describing a Lennard-Jones model for Argon, $\tau = 2\,\mathrm{ps}$), with m the mass of a particle. This represents a time step ten to a hundred times smaller than in standard simulations of simple fluids, but the perturbation of the dynamics due to the change in particle type forced us to use a smaller time step, leading to longer computation times. It is possible to use Monte Carlo updates of the position, which we verified to give results coherent with molecular dynamics, but this approach turned out to lead to significantly longer computation times. The change in particle type was performed using Monte Carlo updates, using a Metropolis rule (see chapter 2). As $\mu_{AB} = 0$ in all our simulations, the Metropolis step only takes into account the change in energy due to interactions between particles. Optimizing the parameters of the simulation to obtain agreement with previous results of ref. [124], we defined an update of the system by 1000 molecular dynamics steps for positions followed by N Monte Carlo steps for particle types. Equilibration was performed by starting from a system with all A type particles and required typically $\sim 3 \times 10^7$ steps, followed by $\sim 5 \times 10^7$ steps for measurement.

One major difficulty in the present simulations is to ensure that we study a demixing transition far from the liquid/gas transition. This turned out to be quite difficult to avoid in 2D systems, thus we focused on 3D simulations, which allowed for direct comparison with the results we obtained in Ising simulations, as well as with previous simulations on this model [76, 124]. Both the cases of cubic and slab geometries where explored.

7.2.2 Pressure measurement

The pressure is computed using to the Virial formula, giving access to $P = -\frac{\partial \Omega}{\partial V}\Big|_{T,N,\mu_{AB}}$ [129, 130], which reads

$$P = nk_BT + \left\langle \frac{1}{dV} \sum_i \vec{r_i}.\vec{f_i} \right\rangle \ , \tag{7.16}$$

where $\vec{r_i}$ is the position of particle i and $\vec{f_i}$ the sum of interactions with other particles, deriving from the potential of Eq.7.3. The x, y and z components of the pressure tensor are also computed, the component k being [128]

$$P_k = \left\langle \frac{1}{V} \sum_i m v_{k_i}^2 + \frac{1}{V} \sum_i r_{ki} f_{ki} \right\rangle \ , \tag{7.17}$$

using the k components of v_{ki} the velocity of particle i and the k components of positions and forces.

7.2.3 Computing the chemical potential

We calculate the chemical potential μ via the particle insertion method (or Widom method) [129, 131]. Let us first describe this method for a one component system of N atoms in a cubic box of

size L and volume $V = L^d$ at constant temperature T. The classical partition function of such a system is

$$Z(N,V,T) = \frac{V^N}{\Lambda^{dN} N!} \int_0^1 \dots \int_0^1 d\vec{s}^N \exp\left[-\varkappa \mathscr{H}_{int}(\vec{s}^N; L)\right] \ , \tag{7.18}$$

where the scaled coordinates $\vec{s}^N = \vec{r}^N/L$ are used, $\varkappa = 1/(k_B T)$ and $\Lambda = h/\sqrt{2\pi m k_B T}$. The chemical potential is defined as

$$\mu = \frac{\partial \Omega_C}{\partial N}\Big|_{T,V} \ , \tag{7.19}$$

with the canonical free energy

$$\Omega_C = -k_B T \ln(Z) \ . \tag{7.20}$$

For sufficiently large N, Eq.7.19 leads to

$$\mu = -k_B T \ln\left(\frac{Z_{N+1}}{Z_N}\right) \ , \tag{7.21}$$

which can be decomposed in an ideal gas part μ_{id} and interaction part μ_{int}

$$\mu = -k_B T \ln\left(\frac{V^N}{\Lambda^{dN} N!}\right) - k_B T \ln\left(\frac{\int d\vec{s}^{N+1} \exp\left[-\varkappa \mathscr{H}_{int}(\vec{s}^{N+1}; L)\right]}{\int d\vec{s}^N \ \exp\left[-\varkappa \mathscr{H}_{int}(\vec{s}^N; L)\right]}\right) \equiv \mu_{id}(n) + \mu_{int} \ . \tag{7.22}$$

The fact that the ideal part is defined using the de Broglie length makes it a difficult quantity to evaluate in a Grand-Canonical situation, as such a microscopic length scale is not naturally defined. This is not a problem in our case as the ideal gas part is an intensive quantity and will not contribute to finite-size effects. We focus on the interaction part μ_{int} and separate the potential energy of the $N+1$ system into the potential energy of the N-particle system, $\mathscr{H}_{int}(\vec{s}^N; L)$, and the interaction of the additional particle, $\Delta\mathscr{H}_{int} = \mathscr{H}_{int}(\vec{s}^{N+1}; L) - \mathscr{H}_{int}(\vec{s}^N; L)$. Then, μ_{int} reads

$$\mu_{int} = -k_B T \ln\left(\int d\vec{s}^{N+1} \left\langle \exp\left[-\varkappa \Delta\mathscr{H}_{int}\right]\right\rangle_N\right) \ , \tag{7.23}$$

where $\langle . \rangle_N$ is the ensemble average over the configurations of the N-particle system.

In practice, Eq.7.23 is implemented as follows: at regular time intervals, we generate a coordinate $\vec{r}^{N+1}$ uniformly in the simulation box and we compute the corresponding Boltzmann factor $\exp\left[-\varkappa \Delta\mathscr{H}_{int}\right]$. The excess part of the chemical potential is obtained by averaging this latter quantity over all generated positions.

We extended this method to the case of a symmetric binary mixture in the semi-grand canonical ensemble. In this case, it is necessary to take into account the possibility of (virtually) inserting either a A or B particle. Thankfully, the symmetrical nature of our mixture gives A and B particles an equivalent role. To compute $\mu = (\mu_A + \mu_B)/2$, we have used the particle insertion method, inserting randomly a A or a B particle with equal probability. For computational reasons, this was the easiest choice, but in further work we would be interested in computing separately μ_A and μ_B. If in principle, averaging μ_A and μ_B should lead to the same result as our random selection of A and B particles, critical slowing down could lead to local ergodicity

breaking leading to a discrepancy between the two approaches. We stress the fact that computing μ proved increasingly difficult with increasing density. We have been able to reach satisfactory precision only for densities lower than $n = 0.8$.

7.2.4 Using cubic geometry as a reference

In chapter 4, we have seen that one difficulty of extracting excess quantities is the subtraction of the bulk and surface contributions from our observables. As we restrict ourselves, for now, to fully periodic boundary conditions, we are only concerned by the bulk contribution. One solution is to use a large enough cubic system of volume L^3 as a "bulk" reference [78, 87], given that the critical region diminishes with increasing side length L as $L^{-1/\nu}$ and the amplitude of the critical Casimir force decreases as L^{-d}. Additionally, in the 3D Ising universality class, the maximum amplitude of the critical Casimir force scaling function is approximately 3 times smaller in cubic geometry than in slab geometry (see figures 3 and 4 of ref. [76]). Thus, we expect that in a cubic system of volume 32^3, in units of σ, the maximum Casimir effect is $3 \times (12/32)^{-3} \approx 57$ times smaller than in a system of thickness $L_\perp = 12$ in slab geometry. The critical region is also $(12/32)^{-1/\nu} \approx 5$ times narrower. As precision of simulation results increase, the excess contributions of the cubic system might be no longer negligible, one then would have to disentangle the different excess contributions (see section 4.3.5).

We studied systems in slab geometry of width $L_\parallel = 60$ and thicknesses ranging from $L_\perp = 5$ to 12, thus a cubic system of volume 32^3 can safely be used as an approximate reference "bulk" state, with the advantage that this reference can be simply subtracted from observables of interest. With the choice of cut-off $r_c = 2.5\sigma$, $L_\perp = 5$ is the smallest thickness conceivable in the case of periodic boundary conditions, smaller sizes would see particles interact with themselves. We also studied the cubic geometry with L ranging from 5 to 10. For the smallest size, the reference cubic system $L = 32$ is clearly a suitable reference state as $(32/5)^3 \approx 260$ and for the largest $L = 10$ system, we still expect a comfortable scale separation as $(32/10)^3 \approx 33$. We will see that our results are coherent with this statement.

7.2.5 Phase diagram and influence of density

In figure 7.3a), we present a sketch of a mean-field phase diagram for a square-well binary mixture close to the symmetrical case $e = 0.57$ [132]. In this case, the presence of a lambda line of continuous demixing transitions suppresses the critical point of the liquid/gas transition, turning it into a tricritical point. We have not tried to reconstruct a complete phase diagram from our Lennard-Jones simulations but kept the total density sufficiently high to study the demixing transition far from the liquid/gas one. In figure 7.3a), we built up the demixing phase diagram for $n \geq 0.4$ by displaying the evolution of the critical temperature T_c^n with density n, estimated from the maximum of the susceptibility of the reference cubic system. We notice that the critical

temperature has a maximum close to $n \sim 0.9$, exhibiting reentrant miscibility [134]. For values of the density sufficiently smaller with respect to $n = 1.0$, the average interaction energy $\langle v_{ij}(r) \rangle$ decreases as density is increased, as the attractive part of the interaction is dominant. Above a threshold value of the density close to $n = 1$, at which the mean inter-particular distance is σ, increasing the density will increase the average interaction energy, as the repulsive part of the potential becomes predominant. This gives a qualitative explanation for the diminution of the typical energy $k_B T_c^n$ for the demixing transition above a threshold density.

Looking for the most efficient density to work at, we have started with a rather high value $n = 1.0$ to avoid the liquid/gas transition, also allowing benchmarking with previous results [124]. Extracting excess quantities at such high density proved difficult. Computing the chemical

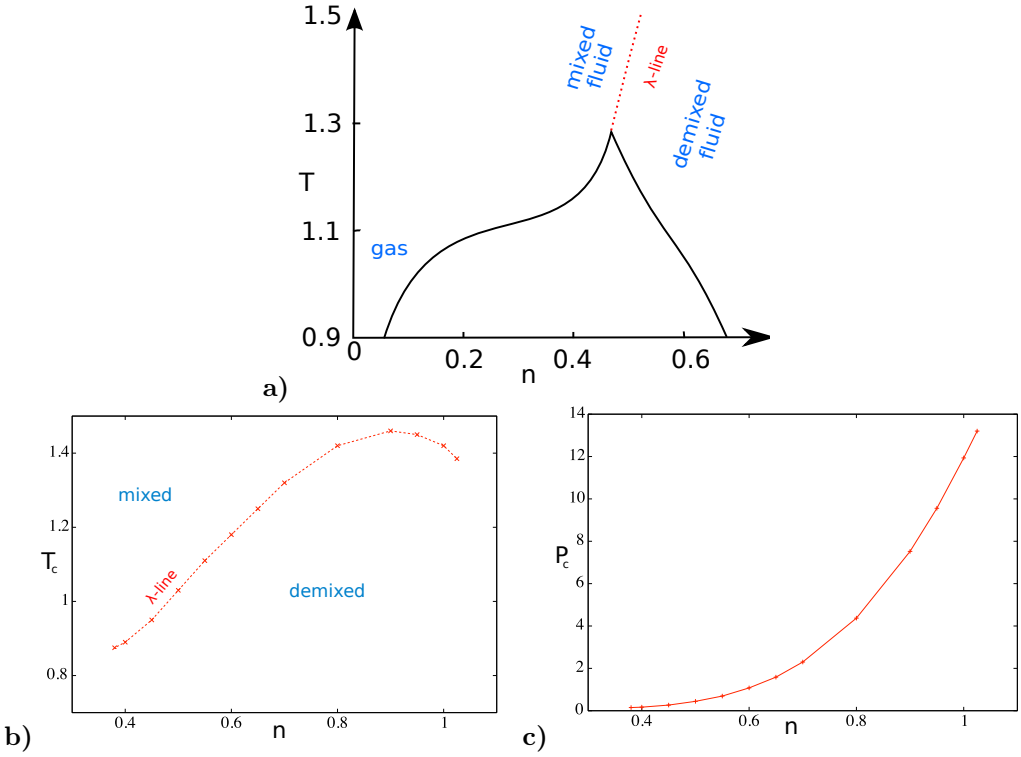

Figure 7.3: **a)** Sketch of the mean-field T-n phase diagram for a Lennard-Jones binary mixture (see ref. [132]). The continuous line represents first order liquid-gas transitions while the red dashed line is the $\lambda-$line of demixing continuous phase transitions. **b)** Partial phase diagram obtained by simulation of a Lennard-Jones symmetrical binary mixture, showing the evolution of the demixing critical temperature T_c^n with density n. A maximum for T_c^n is clearly visible and the system displays reentrant miscibility [133]. **c)** Evolution of the critical pressure P_c with the total density n.

potential requires the virtual insertion of an extra particle to the system, this being obviously a difficult action in a very dense fluid, already for $n = 0.8$. Moreover, the total pressure P_c at the critical temperature depends dramatically on the density, see figure 7.3c), decreasing approximately by an order of magnitude from $n = 1.0$ to $n = 0.5$. The critical Casimir force having an amplitude independent of the density, it seems intuitive to consider that working at lower density will make this excess quantity easier to extract from a smaller value of the total pressure. This was confirmed in practice and we gradually moved to lower densities, $n = 0.6$ and 0.7 allowing for our most accurate results up to now. We stress the fact that this difficulty arising from the small amplitude of the critical Casimir force relatively to the bulk pressure is lifted in experimental approaches when at least one confining wall is also in contact with a non confined fluid. In wetting experiments, the wetting layer is in equilibrium with the gas of binary mixture so that the bulk pressure in the confined layer is compensated by the gas pressure. Thus, the equilibrium thickness of the layer is only determined by confinement forces comparable in amplitude to the Casimir force. Equivalently, if the confinement is obtained by optically trapping a sphere close to a wall (or two spheres), the bulk pressure is compensated by completely immersing the sphere in the critical fluid.

7.3 Universal scaling functions: comparing Ising and Lennard-Jones data

7.3.1 Fully universal scaling form for the excess quantities

In the previous chapters, we were only concerned by the study of the Ising model and used the scaling form for the excess part of the free energy

$$\omega_{ex}(t, L_\perp) = L_\perp^{-d}\Theta\left(u_t\right) \ , \tag{7.24}$$

with $u_t = tL_\perp^{1/\nu}$. Restricting ourselves to the case of $\tilde{h} = 0$, equivalently $\mu_{AB} = 0$, we omit the dependency on this variable. The scaling forms for all observables of interest, in the present study, stem from the excess free energy, and in chapter 6, we developed the relation between the scaling function of the excess free energy Θ, the scaling function of the critical Casimir force θ

$$\theta(u_t, 0) = (d-1)\Theta(u_t, 0) - \frac{u_t}{\nu}\frac{\partial\Theta}{\partial u_t}\Big|_{u_h}(u_t, 0) \ , \tag{7.25}$$

and the excess internal energy density in units of k_BT

$$u_{ex} = -L_\perp^{1/\nu-d}\frac{\partial\Theta}{\partial u_t}\Big|_{u_h} \ . \tag{7.26}$$

Functions θ, Θ and $\frac{\partial\Theta}{\partial u_t}\Big|_{u_h}$ implicitly depend on the model considered, through the non-universal (i.e. model dependent) value of the correlation length amplitude ξ_0^+ (or equivalently ξ_0^-, the

ratio ξ_0^+/ξ_0^- being a universal quantity). As mentioned in section 4.2, to compare observables computed in different models of the same universality class, one must be careful in defining a fully universal quantity based on the scaling of the free energy

$$\omega_{ex}(t, L_\perp) = L_\perp^{-d} \bar{\Theta} \left(t \left(\frac{L_\perp}{\xi_0^+} \right)^{1/\nu} \right) , \tag{7.27}$$

defining the scaling variable

$$x_t = t \left(\frac{L_\perp}{\xi_0^+} \right)^{1/\nu} . \tag{7.28}$$

We omit again the dependency on $\tilde{h} \sim \mu_{AB}$.

The amplitudes of the scaling functions Θ and θ are independent of ξ_0^+. To compare data for the excess free energy and critical Casimir force obtained in different systems belonging to the same universality class, one should simply be careful to use the scaling variable x_t rather than u_t to obtain fully universal functions. The amplitude of the excess internal energy does, on the other hand, depend on ξ_0^+. The fully universal scaling form for the excess internal energy is therefore

$$L_\perp^d \left(\frac{L_\perp}{\xi_0^+} \right)^{-1/\nu} u_{ex} = -\frac{\partial \bar{\Theta}}{\partial x_t}\Big|_{\tilde{h}} = -{\xi_0^+}^{1/\nu} \frac{\partial \Theta}{\partial u_t}\Big|_{u_h} , \tag{7.29}$$

as a function of x_t. This allows for comparison of results we obtained in the Ising model with results in Lennard-Jones systems.

7.3.2 Amplitude of the correlation function

In the Ising model $\xi_0^+ = 0.501(2)$ is known to a very good approximation and we have used this value from the literature, see ref. [4]. We recall that all lengths are measured in units of the microscopic length scale σ which is taken equal to 1 in both the Ising and Lennard-Jones systems. For the case of a Lennard-Jones binary mixture, the correlation length amplitude ξ_0^+ depends on the density n and was estimated for each density using the concentration part of the structure factor [124, 135]. The partial pair correlation functions are given by

$$g_{ij}(r) = \frac{N}{n N_i N_j} \left\langle \sum_{k=1}^{N_i} \sum_{l=1}^{N_j} \delta(r - |\vec{r_k} - \vec{r_l}|) \right\rangle , \tag{7.30}$$

where i, j can be A or B, the type of particle. The fluctuations in the concentration of the system are described by a combination of these pair correlation functions [135]

$$g_{cc}(r) = x_A^2 x_B^2 (g_{AA} + g_{BB} - 2g_{AB}) , \tag{7.31}$$

where $x_A = N_A/N, x_B = N_B/N$. The Fourier transform $S_{cc}(q)$ of $g_{cc}(r)$ takes for small wave vectors an Ornstein-Zernike form

$$S_{cc}(q) = \frac{k_B T \chi}{1 + q^2 \xi^2} , \tag{7.32}$$

with the susceptibly for $T > T_c$

$$k_B T \chi = N(\langle x_A^2 \rangle - 1/4) \ , \tag{7.33}$$

equivalent to the magnetic susceptibility (Eq.2.7) with $m = x_A - x_B$. Thus, we can extract the correlation length ξ from small wave vector measurements of S_{cc} and estimate the amplitude ξ_0^+ by fitting the scaling form

$$\xi = \xi_0^+ |t|^{-\nu} \ , \tag{7.34}$$

using for ν an estimate from literature for the Ising universality class (see table 1.1). In figure 7.4a), we display the evolution of ξ with t and the corresponding fit for various densities, leading to estimates of ξ_0^+ displayed in figure 7.4b). As one can see clearly from figure 7.4, this estimation of ξ_0^+ is somewhat imprecise and will introduce an error on the amplitude of the scaling function of the excess free energy which, unlike the critical Casimir force, depends on ξ_0^+. Nevertheless, it appears clearly that the correlation length amplitude has a maximum value approximately located between $n = 0.7$ and 0.8, just as the critical temperature had a maximum value, but for a larger value of the density n.

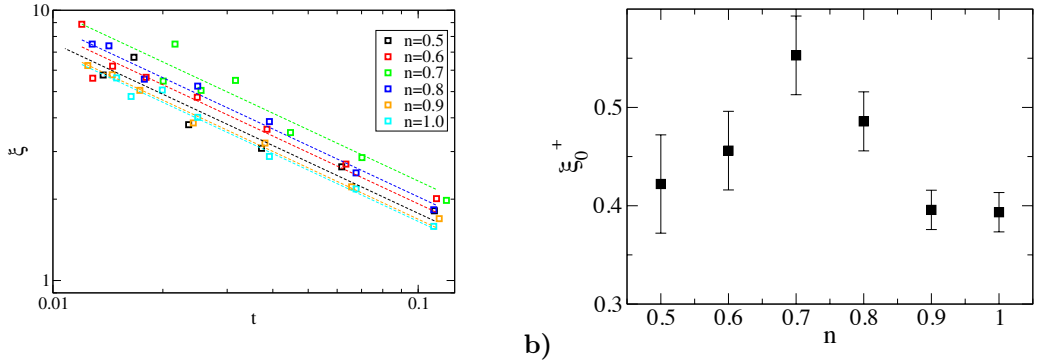

Figure 7.4: **a)** Power law behavior of the correlation length ξ for various densities. Dashed lines are fits of the form $\xi = \xi_0^+ |t|^{-\nu}$, using ξ_0^+ as the only fitting parameter. **b)** Corresponding estimates of ξ_0^+, as a function of density.

7.4 Excess internal energy of the Lennard-Jones binary mixture

The internal energy per unit volume u, in units of $k_B T$, of the Lennard-Jones system is defined by the statistical average of the interaction Hamiltonian (Eq.7.4)

$$u = \frac{\langle \mathscr{H}_{int} \rangle}{k_B T V} \ . \tag{7.35}$$

The excess part of u is obtained by simply subtracting the reference u_{ref} obtained for same temperature and density in the large $L = 32$ cubic system

$$u_{ex} = u - u_{ref} \ . \tag{7.36}$$

Using the universal scaling form of Eq.7.29, we compare in figure 7.5 the excess internal energy computed for the Ising model with fully periodic boundary conditions in chapter 6 with the same quantity computed in the Lennard-Jones binary mixture, for different values of the density and thickness $L_\perp$. All data for the Lennard-Jones fluid were obtained with $L_\parallel = 60$ and densities

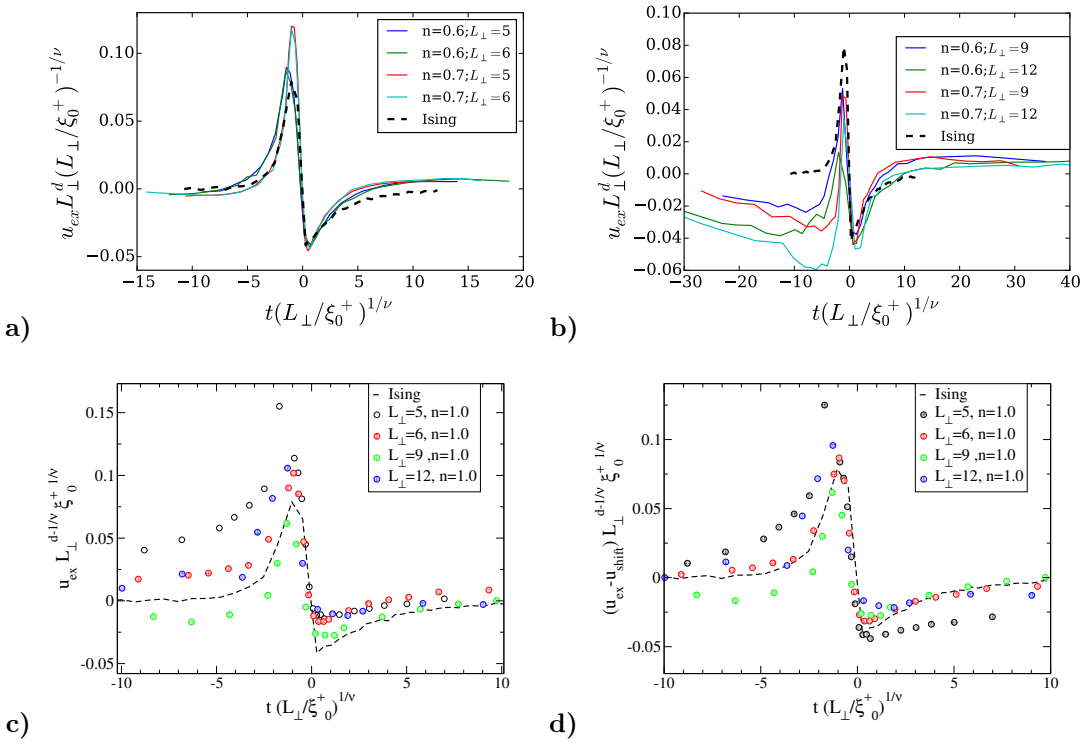

Figure 7.5: Excess internal energy universal scaling form $L_\perp^d \left(L_\perp/\xi_0^+\right)^{-1/\nu} u_{ex}$ with respect to the reduced temperature variable $x_t = t\left(L_\perp/\xi_0^+\right)^{1/\nu}$, obtained for the Ising model with fully periodic boundary conditions (dashed line, see section 6.1.3) and compared to the same quantity obtained in a symmetrical Lennard-Jones binary mixture (colored lines). All data for the Lennard-Jones fluid were obtained with $L_\parallel = 60$ and for densities $n \in [0.6, 0.7, 1.0]$. For clarity, we separated data for the two smallest investigated thicknesses $L_\perp = 5, 6$ **(a)** from data for the two largest ones $L_\perp = 9, 12$ **(b)** and data obtained for the highest density $n = 1.0$ **(c)**. Shifting data for $n = 1.0$ by a small amount $u_{shift}(L_\perp)$ **(d)** shows that the amplitude and width of the critical effect corresponds quite well to the Ising case.

$n = 0.6, 0.7, 1.0$. In the case of the two smallest investigated thicknesses $L_\perp = 5, 6$ (Fig. 7.5a),

we obtain a very convincing agreement with the scaling function of the Ising model,despite the small value of $L_\perp$. For the largest thicknesses investigated $L_\perp = 9, 12$ (Fig. 7.5b), the agreement remains convincing for high temperature data but not for $T < T_c$. In this last case, the apparently non systematic evolution of u_{ex} and the important discrepancy between data for different densities and systems sizes makes us expect this to be related to the difficulty of thermalizing such large systems, requiring very important computation resources, and we believe that higher precision could lead to a collapse of all the data. Another possible explanation, is the important change in aspect ratio from thickness $L_\perp = 5, 6$ to $L_\perp = 9, 12$. However, simulations in Ising systems have proved systems of sizes $L_\perp \sim 10$ and $L_\parallel \sim 60$ to be a good approximation of the slab limit (see chapter 5). If this were the case, the discrepancy between Ising and Lennard-Jones systems would thus have to be explained. Further work is required to confirm this point. For density $n = 1.0$, Fig. 7.5c), the general behavior of the excess energy is still in agreement with that of the Ising model. The rather poor collapse of data for several thicknesses $L_\perp$ makes us expect that we do not yet capture the main scaling behavior of this quantity, but removing a shift value $u_{shift}(L_\perp)$ to u_{ex} to center the scaling function, Fig. 7.5d), we see that the amplitude and width are coherent with Ising data. We believe these shifts arise from the non critical confinement effects discussed in section 7.1.5 and should be present in single component fluid simulations, which we have not yet simulated at the moment of the redaction of this manuscript.

The nice agreement observed between excess internal energy of the Ising and Lennard-Jones models gives us confidence in the validity of our current approach. Moreover, this agreement can also be observed in cubic geometry. In this case, the critical Casimir force is directly related to the excess internal energy [76]

$$\varkappa f_c^{cubic} = \frac{t}{\nu d} u_{ex} \ , \tag{7.37}$$

so that the excess internal energy can easily be related to the scaling function θ^{cubic} of the critical Casimir force in cubic geometry

$$\frac{t}{\nu d} u_{ex} L^d = \theta^{cubic} \ , \tag{7.38}$$

which was computed through Monte Carlo simulations in the Ising model in ref. [76]. In figure 7.6a), we display Tu_{ex} for various sizes $L \in [5, 6, 9, 10]$ as a function of temperature for a density $n = 0.7$. A finite-size critical effect is clear, a peak in u_{ex} appearing close to $T_c^{0.7} = 1.32$, and its amplitude decreases with increasing size. However, the excess internal energy does not go to zero far from the critical temperature, especially for the smallest system size $L = 5$. The limit value u_{shift} reached by the excess energy decreases with increasing size L in a non monotonic way, oscillating around zero. We have already mentioned that such non critical effects have been observed in single component fluid simulations [127]; oscillations of the internal energy being related to the particularly small sizes used. Increasing the system size would then make this effect negligible but for now, to focus on the critical effect, we removed the limit value u_{shift} from u_{ex} before trying the finite-size scaling from of Eq.7.38. One can notice from figure 7.6a) that u_{shift} is more pronounced at $t < 0$ than $t > 0$ for $L = 5$. Thus, $u_{shift}(L, sign(t))$ both

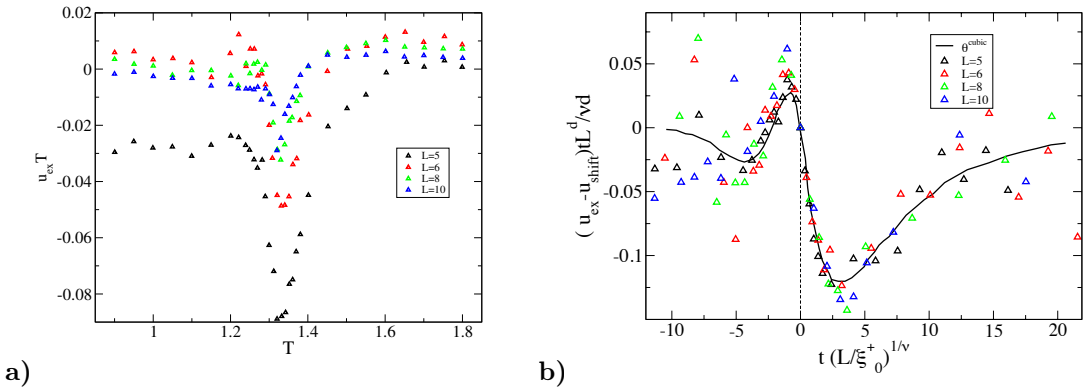

Figure 7.6: Excess internal energy u_{ex} obtained in a symmetrical Lennard-Jones binary mixture in cubic geometry (colored points) **(a)**. Following Eq.7.38, this excess internal energy can be compared to the scaling function of the critical Casimir force θ^{cubic} in cubic geometry computed in ref. [76] in the Ising model (solid black line), after removing a non critical contribution $u_{shift}(L, sign(t))$ to u_{ex} **(b)**. Lennard-Jones data were obtained in systems of size $L \in [5, 6, 9, 10]$ at density $n = 0.7$.

depends on L and the sign of t and for each system size. As the system changes from a mixture to a simple fluid when crossing the transition, it is not surprising that the shift evolves from high to low temperature. Hence, we have subtracted two different values of u_{shift} to u_{ex} for data above and below the critical temperature. This proved to be an acceptable approximation within the current precision but could eventually result in a discontinuity around $T_c^{0.7}$ in the data, as u_{shift} is in principle a continuous function of the temperature (this will be the case below). In figure 7.6b), we show the convincing agreement between excess internal energy data computed in our Lennard-Jones simulations and θ^{cubic} estimated in ref. [76] in the Ising model, the agreement being excellent except for low temperatures where our data are clearly dominated by statistical noise.

As we developed in chapter 6, the knowledge of the excess internal energy scaling function gives access to the scaling function of the excess free energy and thus to the critical Casimir force scaling function, or any excess quantity stemming from the excess free energy. However, the specificity of the present Lennard-Jones simulation is that it can give direct access to the critical Casimir force and its fluctuations. Thus, we are interested in the direct measurement of the pressure and chemical potential, rather than extracting the average Casimir force through measurement and integration of the excess internal energy.

7.5 Critical pressure anisotropy in slab geometry

7.5.1 Universal scaling function for the pressure anisotropy

We have mentioned at the end of chapter 6 that it is possible to extend our study of the Casimir effect to the case of non zero aspect ratios, simply by adding a dependency on $\rho = L_\perp/L_\parallel$ to the universal scaling functions [76]. The excess free energy density, in units of $k_BT = 1/\varkappa$, then scales as

$$\omega_{ex}(t, L_\perp, \rho) = L_\perp^{-d}\Theta_\rho\left(u_t, \rho\right) \ . \tag{7.39}$$

For the sake of simplicity, we will not take into account the dependency on the field $h \sim \mu_{AB}$, which we always set to zero in Lennard-Jones simulations. The critical Casimir force by unit of surface in the confining direction z is then given by

$$\begin{aligned} \varkappa f_c^\perp &= -\tfrac{1}{L_\parallel^{d-1}}\tfrac{\partial(V\omega_{ex})}{\partial L_\perp} \\ &= L_\perp^{-d}\left[(d-1) - \tfrac{u_t}{\nu}\tfrac{\partial}{\partial u_t} - \rho\tfrac{\partial}{\partial\rho}\right]\Theta_\rho(u_t,\rho) \ , \end{aligned} \tag{7.40}$$

and corresponds to the extension to arbitrary values of ρ of f_c, the definition of the Casimir force we have used up to now in this work (Eq.5.2). Of course, in the limit of slab geometry

$$f_c^\perp \underset{\rho\to 0}{\to} f_c \ . \tag{7.41}$$

The evolution of the form of the Casimir force scaling function with ρ has already been studied in Monte Carlo simulations of the Ising model [76], but another effect that this formalism allows one to tackle is the Casimir effect in the transverse directions x, y, related to a change in the width $L_\parallel$ rather than the thickness $L_\perp$. We define the excess contribution to the confining force in the transverse directions as the derivative of the excess free energy with volume at fixed $L_\perp$

$$\begin{aligned} \varkappa f_c^\parallel &= -\tfrac{\partial(V\omega_{ex})}{\partial V}\Big|_{L_\perp} \ , \\ &= -\tfrac{1}{L_\perp L_\parallel^{(d-1)}}\tfrac{\partial(V\omega_{ex})}{\partial L_\parallel}\Big|_{L_\perp} \ , \\ &= -\tfrac{L_\perp^{-d}}{(d-1)}\left[(d-1) - \rho\tfrac{\partial}{\partial\rho}\right]\Theta_\rho \ . \end{aligned} \tag{7.42}$$

As expected from the clearly asymmetric roles played by $L_\perp$ and $L_\parallel$ in this geometry, the critical force is anisotropic and $f_c^\parallel$ differs from $f_c^\perp$. The two forces can be related using Eq.7.40 and 7.42

$$f_c^\parallel = \frac{1}{d-1}\left[-f_c^\perp - k_BTL_\perp^{-d}\frac{u_t}{\nu}\frac{\partial\Theta_\rho}{\partial u_t}\right] \ , \tag{7.43}$$

and the anisotropy is directly related to the excess internal energy $-L_\perp^{-d}u_t\frac{\partial\Theta_\rho}{\partial u_t} = tu_{ex}$. We remark that an average of the forces in the three directions x, y, z gives

$$\frac{\varkappa}{d}(f_c^\perp + (d-1)f_c^\parallel) = -L_\perp^{-d}\frac{u_t}{\nu d}\frac{\partial\Theta_\rho}{\partial u_t} = \frac{t}{\nu d}u_{ex} \ , \tag{7.44}$$

and is directly related to the excess internal energy. In the limit of cubic geometry, $\rho \to 1$, we of course expect to recover isotropy and

$$f_c^{\perp} = f_c^{\parallel} \tag{7.45}$$

so that

$$\frac{\varkappa}{d}(f_c^{\perp} + (d-1)f_c^{\parallel}) \underset{\rho\to 1}{\to} \varkappa f_c^{cubic} = \frac{t}{\nu d} u_{ex} \ , \tag{7.46}$$

and the critical Casimir force f_c^{cubic} is directly related to the excess internal energy, a result already demonstrated in ref. [76], giving us confidence in our approach.

Let us now study the anisotropy itself. Eq.7.43 leads to

$$f_c^{\parallel} - f_c^{\perp} = \frac{k_B T}{d-1}\left[\frac{-d}{k_B T} f_c^{\perp} + \frac{t}{\nu} u_{ex}\right] \ . \tag{7.47}$$

In the slab limit, we know that

$$\varkappa f_c^{\perp} \underset{\rho\to 0}{\to} \varkappa f_c = (d-1)\omega_{ex} + t\nu^{-1} u_{ex} \ , \tag{7.48}$$

which implies

$$\rho \frac{\Theta_\rho}{\partial \rho}\Big|_{x_\perp} \underset{\rho\to 0}{\to} 0 \ . \tag{7.49}$$

this limit being the signature of the recovery of extensivity of the free energy $V\omega_{ex}$ with respect to $L_\parallel$. Thus, the anisotropy becomes

$$\varkappa(f_c^{\parallel} - f_c^{\perp}) \underset{\rho\to 0}{\to} -d\omega_{ex} - t\nu^{-1} u_{ex} = -\varkappa f_c^{\perp} - \omega_{ex} \ , \tag{7.50}$$

and consequently

$$\varkappa f_c^{\parallel} \underset{\rho\to 0}{\to} -\omega_{ex} = -L_\perp^{-d}\Theta\left(u_t\right) \ . \tag{7.51}$$

The universal scaling form of the anisotropy in the limit of slab geometry is thus

$$L_\perp^d \varkappa(f_c^{\perp} - f_c^{\parallel}) \underset{\rho\to 0}{\to} \theta(u_t) + \Theta(u_t) \ , \tag{7.52}$$

the sum of the scaling functions of the critical Casimir force and of the excess free energy that we have estimated in chapters 5 and 6 in the Ising model in the limit $\rho \to 0$. In the following, we will always assume that this limit is reached, at least to a good approximation.

7.5.2 Pressure anisotropy in a Lennard-Jones binary mixture

In Lennard-Jones simulations, the critical Casimir forces are expected to be excess quantities of the generalized pressure $\tilde{P} = P - \mu\rho$. However, the anisotropy must clearly come from the pressure itself and not from the chemical potential, which is an intrinsically isotropic quantity. Lennard-Jones simulations allow for the computation of this anisotropy and of its fluctuations, as

the virial formula for the pressure naturally provides instantaneous measurements of the pressure in x, y and z directions. Thus, we can compute the anisotropy in pressure

$$P_\perp - P_\parallel \equiv P_z - \frac{P_x + P_y}{2} \ , \tag{7.53}$$

which we display in figure 7.7. For clarity, in figure 7.7a), we only display $P_\perp - P_\parallel$ for the smallest $L_\perp = 5$ and largest $L_\perp = 12$ thicknesses investigated, both for $n = 0.6$ and $n = 0.7$. In all cases, $L_\parallel = 60$. Considering the current precision, no anisotropy is seen in the case $L_\perp = 12$, whereas a clear one is seen for $L_\perp = 5$. We distinguish two features in this anisotropy. Firstly, the minimum

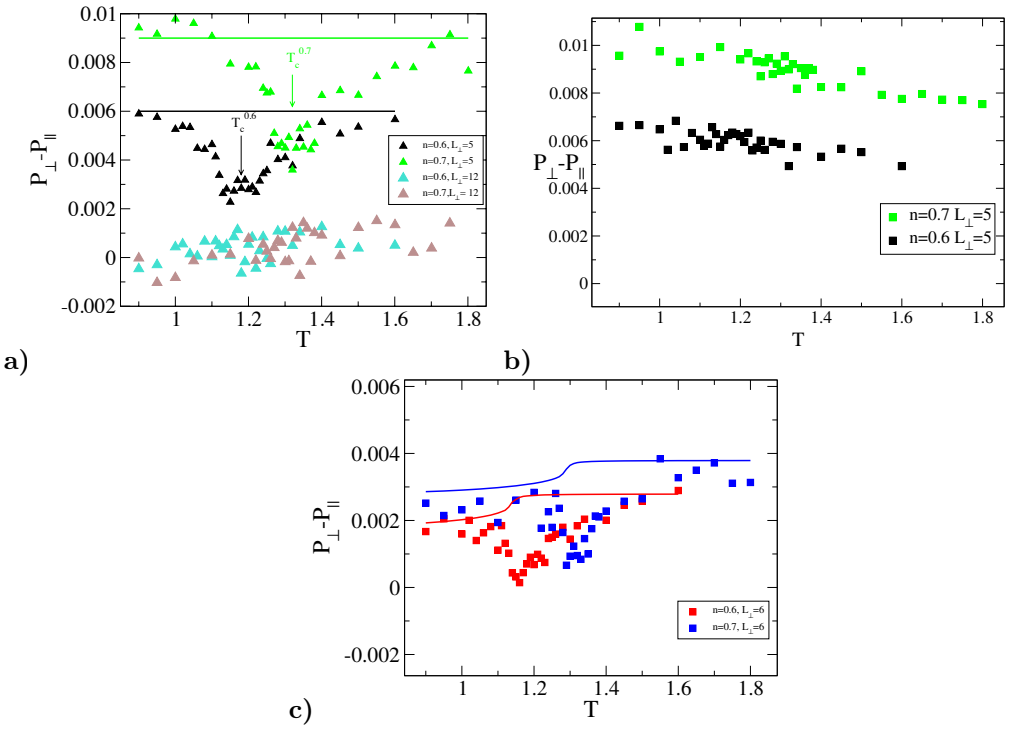

Figure 7.7: Pressure anisotropy $P_\perp - P_\parallel$ in a Lennard-Jones system in slab geometry of thickness $L_\perp = 5, 12$ for two values of the total density $n = 0.6, 0.7$. In all cases $L_\parallel = 60$. In the case of a symmetrical binary mixture **(a)**, for $L_\perp = 5$, the pressure anisotropy clearly has a minimum value close to the demixing critical temperature T_c^n (located by arrows). Continuous lines show estimates of the non critical pressure anisotropy $P_{shift}(T, n, L_\perp)$. In the case of a one component Lennard-Jones fluid **(b)** an anisotropy is still present. In the case of a binary mixture confined with $L_\perp = 6$ **(c)**, the limit value of the pressure anisotropy appears different for high and low temperatures. We used the ansatz $P_{shift}(T, n, L_\perp) = A(n, L_\perp) + B(n, L_\perp)|m(T)|$ (continuous lines) to capture this effect ($m(T) = (N_A - N_B)/N$).

of the anisotropy is located close to the critical temperature, which changes significantly with the density, so that we can clearly identify a critical effect in the anisotropy. Secondly, far from the critical temperature, the anisotropy does not tend to zero, so that a non critical anisotropy is also detected. In figure 7.7b), we display the difference $P_\perp - P_\parallel$ that we obtain in a one component Lennard-Jones fluid, for the same densities $n = 0.6$ and 0.7 and dimensions $L_\perp = 5$ and $L_\parallel = 60$. An anisotropy in the pressure is observed, of approximately the same amplitude as the non critical anisotropy observed in the binary mixture. This effect is induced by the periodic boundary conditions and was observed in single component fluid models (including Lennard-Jones) in non cubic geometries in ref. [126]. It was shown that the pressure anisotropy oscillates as the system size is changed, vanishing as the system grows, but significant for systems of small size $< 10\sigma$. This effect was considered in ref. [126] as a *periodic error* on pressure measurements but we can interpret it, as discussed in section 7.1.5, as a non critical confinement force.

To check the scaling form of Eq.7.54 for the anisotropy, we need to subtract the non critical contribution to the pressure anisotropy. It is tempting to use the anisotropy found in the single component Lennard-Jones system to subtract non critical anisotropy in the mixture's pressure. However, in the case of a binary mixture, the composition changes with temperature. This is not the case of course in the one component fluid and thus there is no reason for the non critical anisotropy to evolve in the same way in both two and one components fluids. As a preliminary test, we have simply subtracted an ansätze $P_{shift}(T, L_\perp, n)$ for the baseline shift to $P_\perp - P_\parallel$ and tested the validity of the scaling form

$$\varkappa L_\perp^d (P_\perp - P_\parallel - P_{shift}(T, L_\perp, n)) = \theta(u_t) + \Theta(u_t) \ . \tag{7.54}$$

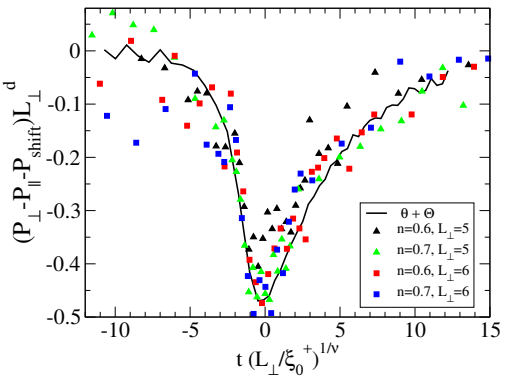

Figure 7.8: Finite-size scaling of the critical part of the pressure anisotropy computed in the symmetrical Lennard-Jones binary mixture for $L_\perp = 5, 6$, $L_\parallel = 60$ and $n = 0.6, 0.7$ (colored points). The data are in very good agreement with the expected universal scaling function $\theta + \Theta$, sum of the scaling function for the critical Casimir force and for the excess free energy, computed in the Ising model (solid black line).

assuming the limit $\rho \to 0$ is verified. For $L_\perp = 5$, we used a constant shift $P_{shift}(T, n, L_\perp) = A_{shift}(n, L_\perp)$, represented in figure 7.7a). For $L_\perp = 6$, the limit value of the pressure anisotropy appears different for high and low temperatures (Fig. 7.7c). Assuming that this change in the non critical anisotropy is related to the change in composition of the mixture, we used the ansatz

$$P_{shift}(T, n, L_\perp) = A_{shift}(n, L_\perp) + B_{shift}(n, L_\perp)|m(T)| \ , \tag{7.55}$$

to capture this effect, with $m(T) = (N_A - N_B)/N$ the order parameter. We display $P_{shift}(T, L_\perp, n)$ in figure 7.7c): this ansatz is very close to using two different constant shifts for temperatures above and below T_c^n as it quite sharply evolves close to the critical temperature.

In figure 7.8, we test the scaling form of Eq.7.54, comparing the critical part of the pressure anisotropy to the sum of functions θ and Θ obtained through Monte Carlo simulation in the Ising model (see chapters 5 and 6). The agreement between Lennard-Jones and Ising data is very convincing and clearly confirms our predictions for the universal scaling function of the critical pressure anisotropy. The maximum of the scaled pressure anisotropy seems slightly lower for $L_\perp = 5, n = 0.6$, but this discrepancy could be absorbed in the choice of a larger value of P_{shift}. Increasing the thickness $L_\perp$, P_{shift} decreases so that we expect that for sufficiently large systems only the critical anisotropy should remain. However, we have not been able to reach this limit with sufficient precision for now.

7.6 Pressure and chemical potential

7.6.1 Generalized pressure and critical Casimir force

As discussed previously, we expect to be able to extract the critical Casimir force from the measurement of the pressure and the chemical potential. We expect the form

$$\begin{aligned} P_\perp &= f_c^\perp + n\mu_{ex} + P_{bulk} \ , \\ P_\parallel &= f_c^\parallel + n\mu_{ex} + P_{bulk} \ . \end{aligned} \tag{7.56}$$

In section 7.5.2 we have seen that, for the smallest system thicknesses, we must add to this picture a non critical confinement pressure $P_{shift}(T, L_\perp, n)$. Making the hypothesis that this effect solely affects $P_\perp$, that it to say that $L_\parallel$ is large enough not to cut-off the density pair correlation function, we get

$$\begin{aligned} P_\perp &= f_c^\perp + n\mu_{ex} + P_{shift}(T, L_\perp, n) + P_{bulk}(T, n) \ , \\ P_\parallel &= f_c^\parallel + n\mu_{ex} + P_{bulk}(T, n) \ , \end{aligned} \tag{7.57}$$

which is coherent with our observations for the anisotropy $P_\perp - P_\parallel$. In figure 7.9, we show the excess part

$$P_{ex,\perp} = P_\perp - P^{cubic}(T, n) \ , \tag{7.58}$$

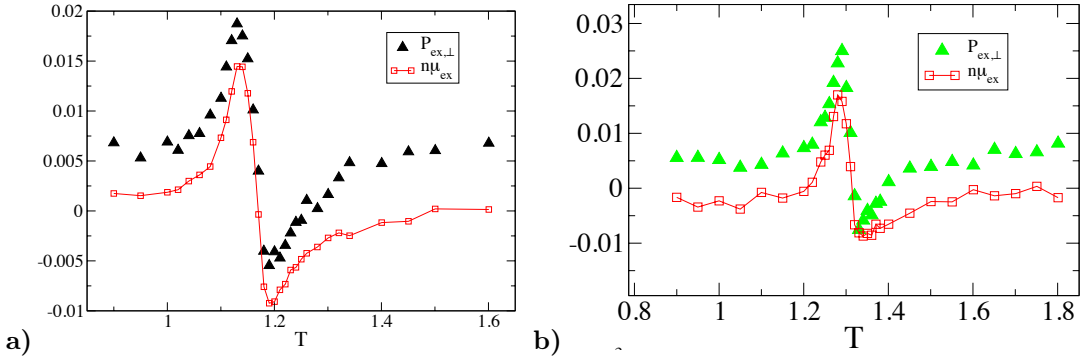

Figure 7.9: Excess part $P_{ex,\perp}$ (Eq.7.58) of the confinement pressure $P_\perp$, compared to the excess chemical potential multiplied by density $n\mu_{ex}$. All data are obtained in systems of sizes $L_\perp = 5, L_\parallel = 60$. For clarity, we separate data obtained at density $n = 0.6$ **(a)** and $n = 0.7$ **(b)**.

of the confinement pressure $P_\perp$, using the pressure $P^{cubic}(T, n)$ computed in the large $L = 32$ cubic system as an estimate of the bulk pressure $P^{bulk}(T, n)$. The presence of $P_{shift}(T, n, L_\perp)$ is clear. The form and amplitude of the excess pressure is incompatible with the critical Casimir force $f_c^\perp$ (see for example Fig.4.5), which does not change sign with temperature and is expected to have an amplitude of $\approx -3 \times 10^{-3}$ for $L_\perp = 5$, $n = 0.6$, thus an order of magnitude smaller than the critical effect observed in figure 7.9. Defining the excess part of the chemical potential

$$\mu_{ex} = \mu(T, n, L_\perp) - \mu^{cubic}(T, n) \ , \tag{7.59}$$

it appears clearly in figure 7.9 that $P_{ex,\perp}$ and $n\mu_{ex}$ are dominated by a similar term. This term resembles the excess internal energy and from the amplitudes shown it seems that this term will cancel in taking the difference between the two quantities. We notice in figure 7.9 a small shift, so that $n\mu_{ex}$ does not decay to zero far from the critical temperature, which we interpret once again as a non critical confinement effect. Therefore, we shall use a shift μ_{shift} for each densities to recover the limit of vanishing μ_{ex} far from T_c^n. We complete again our decomposition of $P_\perp$

$$P_\perp = f_c^\perp + n\mu_{ex} + \tilde{P}_{shift}(T, L_\perp, n) + P_{bulk}(T, n) \ , \tag{7.60}$$

and rather than separately estimating μ_{shift} and P_{shift}, which would be quite delicate, we define the generalized pressure non critical shift

$$\tilde{P}_{shift}(T, n, L_\perp) = P_{shift} - n\mu_{shift} = \tilde{A}(n, L_\perp) + \tilde{B}(n, L_\perp)|m(T)| \ , \tag{7.61}$$

which we expect to depend on the change in composition of the system (as in the case of the pressure anisotropy in section 7.5.2) $\tilde{A}, \tilde{B}$ being fitting parameters. Thus, the confinement excess generalized pressure

$$\tilde{P}_{ex,\perp} = P_{ex,\perp} - n\mu_{ex} \ , \tag{7.62}$$

should contain both a non critical confinement effect and the critical Casimir force. We expect that its critical part $\tilde{P}_{ex,\perp} - \tilde{P}_{shift}$ amounts to the critical Casimir force in the slab limit $f_c^{\perp} \underset{\rho \to 0}{\to} f_c$ and thus scales as

$$\frac{L_\perp^d}{k_B T}(\tilde{P}_{ex,\perp} - \tilde{P}_{shift}) = \theta(x_t) \ . \tag{7.63}$$

In figure 7.10, we show preliminary results for this analysis for $n = 0.6, 0.7$, $L_\perp = 5$ and $L_\parallel = 60$. Looking at $\tilde{P}_{ex,\perp}$ (Fig. 7.10 a, b), it is clear that the noise level is still quite high with respect to the effect we are trying to capture. However, we can estimate the non critical effect using the form of Eq.7.61 (see Fig. 7.10 a, b). For density $n = 0.6$, the change of $\tilde{P}_{shift}$ across the transition is much more pronounced than for $n = 0.7$, for which the shift is almost a constant. We then compare $\frac{L_\perp^d}{k_B T}(\tilde{P}_{ex,\perp} - \tilde{P}_{shift})$, to the scaling function θ computed in the Ising model, see figure 7.10 c, d). This shows a promising tendency for $n = 0.7$ and a promising agreement

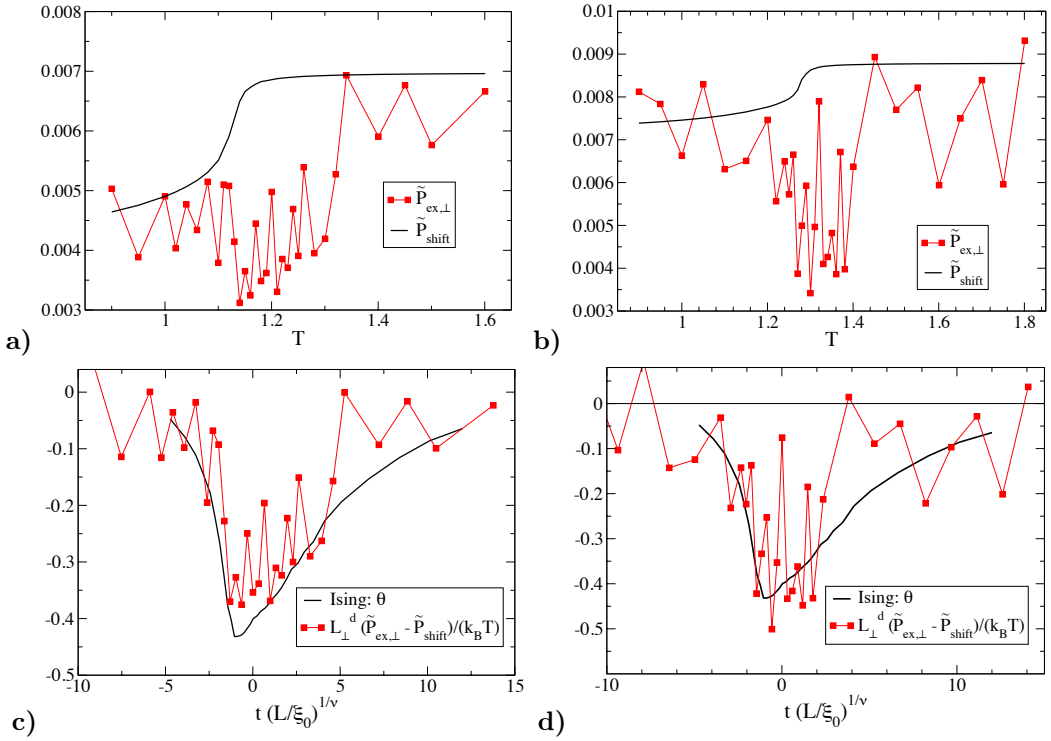

Figure 7.10: Excess part of the generalized pressure $\tilde{P}_{ex,\perp}$ (red squares) obtained in a Lennard-Jones binary mixture with $n = 0.6$ **(a)** and $n = 0.7$ **(b)**. In all cases, $L_\perp = 5, L_\parallel = 60$. Using the form of Eq.7.61, we estimate the non critical part of this excess generalized pressure (black lines). Then, we can test the scaling form of Eq.7.63 by comparing the critical part of the excess generalized pressure (red squares), for $n = 0.6$ **(c)** and $n = 0.7$ **(d)**, to the scaling function of the critical Casimir force θ obtained in the Ising mode (black line).

for $n = 0.6$. This result is only preliminary and we present the only configurations for which we reached at the moment of the redaction of the manuscript sufficient precision to obtain a first indication of a direct measurement of the critical Casimir force in a Lennard-Jones simulation. Although the level of noise on the signal is still high, the fact that the critical effect observed in both $P_{ex,\perp}$ and $n\mu_{ex}$ (Fig.7.9), ten times larger than the critical Casimir force, cancels exactly is already an extremely encouraging result. We believe that better statistics, with data further away from the critical temperature, will allow a better estimate of the non critical shifts and confirm this first signature of the critical Casimir force.

7.6.2 Excess chemical potential and excess internal energy

To define the scaling function of the excess chemical potential, we need to understand how the excess part of the free energy depends on the the total number of particles N. We know that the excess free energy density ω_{ex} takes a universal scaling form, see Eq.7.27 for the limit case $\rho \to 0$. Two quantities appearing in this scaling form depend on N, through the density n: $\xi_0^+(n)$ and T_c^n (see figures 7.3 and 7.4). The scaling function of Eq.7.27 being fully universal, we can assume that the dependency of ω_{ex} on density is entirely contained in $\xi_0^+(n)$ and T_c^n and we can make explicit this dependency

$$\omega_{ex}(t, L_\perp, n) = L_\perp^{-d} \bar{\Theta}\left(\left(\frac{T - T_c^n}{T_c^n}\right)\left(\frac{L_\perp}{\xi_0^+(n)}\right)^{1/\nu}\right) \ . \tag{7.64}$$

here still in the limit $\rho \to 0$. The excess chemical potential is defined as

$$\varkappa\mu_{ex} = \frac{\partial V \omega_{ex}}{\partial N}\Big|_{T,V} = V L_\perp^{-d} \frac{\partial \bar{\Theta}}{\partial N}\Big|_{T,V} \ . \tag{7.65}$$

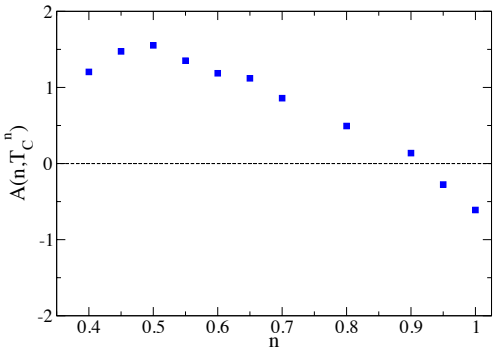

Figure 7.11: Evolution of $A(n, T_c^n) = \frac{1}{T_c^n}\frac{\partial T_c^n}{\partial n}$, the dominant part close to the critical temperature of the factor $A(n, T)$ relating excess internal energy and excess chemical potential.

Using the scaling variable $x_t = \left(\frac{T-T_c^n}{T_c^n}\right)\left(\frac{L_\perp}{\xi_0^+(n)}\right)^{1/\nu}$, we can relate the chemical potential to the internal energy

$$\varkappa\mu_{ex} = VL_\perp^{-d}\frac{\partial x_t}{\partial N}\Big|_{T,V}\frac{\partial\bar{\Theta}}{\partial x_t}\Big|_{T,V} = -V\frac{\partial x_t}{\partial N}\Big|_{T,V}\left(\frac{L_\perp}{\xi_0^+}\right)^{-1/\nu} u_{ex} = A(n,T)u_{ex}\ , \tag{7.66}$$

with

$$A(n,T) = -V\frac{\partial x_t}{\partial N}\Big|_{T,V}\left(\frac{L_\perp}{\xi_0^+}\right)^{-1/\nu} = \frac{1}{T_c^n}\frac{\partial T_c^n}{\partial n} + t\left[\frac{1}{T_c^n}\frac{\partial T_c^n}{\partial n} + \frac{1}{\xi_0^+\nu}\frac{\partial\xi_0^+}{\partial n}\right]\ . \tag{7.67}$$

Thus, at a given density and at $T = T_c^n$, the excess chemical potential and excess internal energy are expected to be simply proportional, by a factor $A(n,T_c^n) = \frac{1}{T_c^n}\frac{\partial T_c^n}{\partial n}$. An interesting feature of this factor is that, as it appears clearly from the evolution of T_c^n with density (see figure 7.3), it changes sign at a density close to $n = 0.9$, see figure 7.11. To test the validity of the relation between excess chemical potential and excess internal energy (Eq.7.66), in figure 7.12 we compare

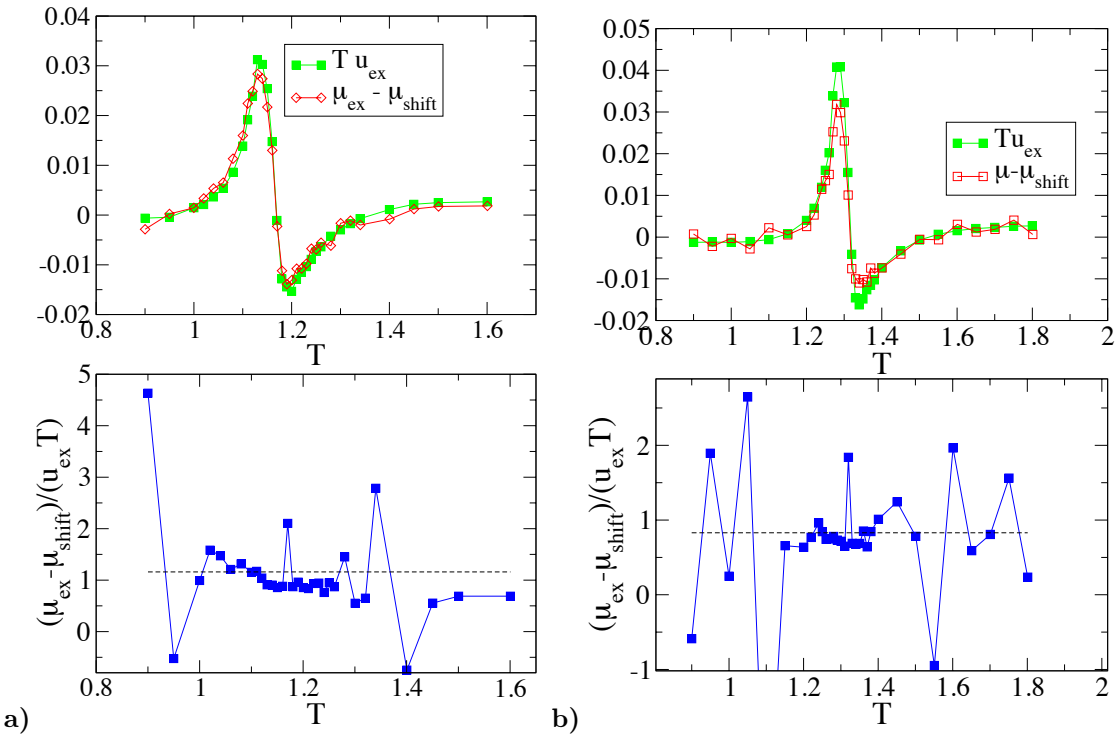

Figure 7.12: Comparison of the excess chemical potential $\mu_{ex} - \mu_{shift}$ (see main text) to the excess internal energy u_{ex} in a symmetrical Lannard-Jones binary mixture at density $n = 0.6$ **(a)** and $n = 0.7$ **(b)**. All data are obtained in systems of sizes $L_\perp = 5, L_\parallel = 60$. In the bottom figures, we compare the ratio $(\mu_{ex} - \mu_{shift})/(Tu_{ex})$ (blue squares) to its expected value at the critical point $A(n,T_c^n) = \frac{1}{T_c^n}\frac{\partial T_c^n}{\partial n}$ (black dashed lines).

$\mu_{ex} - \mu_{shift}$ to the excess internal energy $k_B T u_{ex}$ (we recall that in our simulation $k_B \equiv 1$) for $L_\perp = 5$ and $n = 0.6, 0.7$. The similarity of the two observables is striking. Moreover, computing the ratio $\varkappa(\mu_{ex} - \mu_{shift})/u_{ex}$, we find a good agreement with our estimate of $A(n, T_c^n)$, see figure 7.12, giving us confidence in the relations of Eq.7.66 and 7.67 between excess chemical potential and internal energy. The $A(n, T_c^n)$ factors are very close to unity but the precision of our date seems sufficient to extract the predicted trend around unity for these two density values. At the moment of the redaction of this manuscript, we have not yet produced the necessary data to present the same treatment as in figure 7.12 for other system sizes or densities. Typically, computing the chemical potential at densities $n \geq 0.8$ proved extremely challenging. However, we are confident that future data can confirm our findings as they are supported by qualitative observations in the pressure and internal energy measurements, more easily accessible than chemical potential ones.

As we have noticed, the excess pressure $P_\perp - P^{cubic}(T, n)$ is dominated by the term $n\mu_{ex}$, Eq.7.57, so that we can compare it to the excess internal energy to draw qualitative conclusions. In figure 7.13, we compare the excess pressure to the excess internal energy for $L_\perp \in [5, 6, 9, 12]$ and $n = 0.6, 0.7, 1.0$. We remark their great similarity in general, comforting the relation between chemical potential and internal energy (Eq.7.66). For densities $n = 0.6, 0.7$, we display the evolution of $P_\perp - P^{cubic}$ against u_{ex} but at higher density $n = 1.0$ we looked at the evolution of the excess part of $P^{averaged} = (1/d)(P_x + P_y + P_z)$. Measurements of the pressure at higher density requiring longer computation times than at $n = 0.6, 0.7$, we did not reach sufficient statistics for P_z alone for all system sizes at the moment of writing the present chapter. Thus, as a preliminary approach, we present data for $P^{averaged}$, which is also suited for a comparison with u_{ex} as it is also expected to be dominated by the excess chemical potential contribution. The first thing one can remark in figure 7.13e) is that the excess pressure $P^{averaged} - P^{cubic}$, at density $n = 1.0$, has undergone a sign change (also present in $P_\perp$) compared with lower densities $n = 0.6, 0.7$. The excess pressure is now positive above the critical temperature and negative below. This sign change is actually coherent with the sign change of $A(n, T_c^n)$ (Fig.7.11). In figures 7.13e) and f), we compare $P^{averaged} - P^{cubic}$ with $A(n, T_c^n)u_{ex}$ scaled by the factor $A(n, T_c^n) \approx -0.6$. Scaled in this way, it is clear that the two quantities main contribution remain proportional despite the change in sign of $P^{averaged} - P^{cubic}$, well captured by the factor $A(n, T_c^n)$.

7.7 Conclusion

Using Semi-Grand Canonical simulations of a symmetrical Lennard-Jones binary mixture, we have made contact with previous results obtained in the Ising model through measurements of the universal scaling functions of the excess internal energy but also the excess generalized pressure $\tilde{P} = P - n\mu$, which is the suitable quantity for a direct measurement of the critical Casimir force. The results presented here are preliminary, as the computation of the chemical

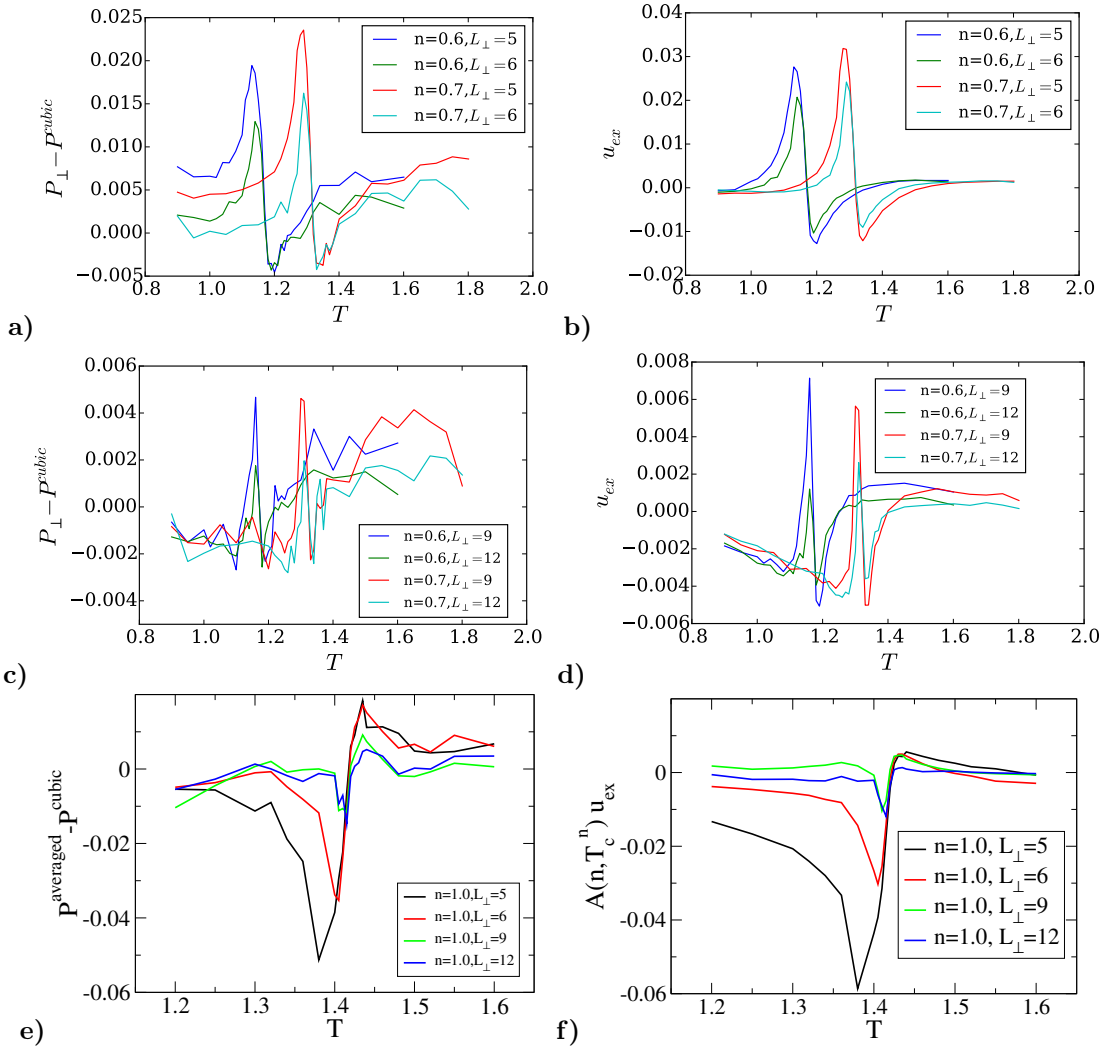

Figure 7.13: Evolution of the excess pressure $P_\perp - P^{cubic}$ in the confining z direction **(a,c)** against the the excess internal energy u_{ex} **(b,d)** for Lennard-Jones binary mixtures of density $n = \in [0.6, 0.7]$ in systems of size $L_\perp \in [5, 6, 9, 12]$ and $L_\parallel = 60$. For the highest density $n = 1.0$, we display the excess pressure averaged in the three directions $P^{averaged} - P^{cubic}$ **(e)** and, to emphasis the similarity, we do not display simply u_{ex} but $A(n, T_c^n)u_{ex}$ **(f)** as in this case, unlike the other densities, $A(n, T_c^n) \approx -0.6$ is negative.

potential proved quite challenging. Moreover, the analysis of scaling behavior is complicated by the presence of non critical confinement effects induced by the particularly small system sizes used. As the numerical effort required to reach sufficient precision increases rapidly with system size, we cannot yet produce results in large enough systems to make these effects negligible. However, we have been able to propose preliminary approaches to take these effects into account and obtain convincing agreement with data computed in the Ising model in the previous chapters.

We also obtained results that were not accessible directly to Ising model simulations. We proposed and successfully verified the universal finite size scaling form for the anisotropy of the excess part of the pressure. In slab geometry, the critical Casimir force is defined as the critical contribution to the confinement force in the confining direction z. However, a transverse effect in direction x and y also exists and the excess contribution to the transverse pressure $P_{\parallel}$ is different from the critical Casimir force in the confining direction [21]. The universal scaling function of the anisotropy $P_{\perp} - P_{\parallel}$ proved to be the sum $\theta + \Theta$ of the scaling functions of the critical Casimir force θ and the excess free energy Θ. Moreover, we have been able to distinguish the influence in the critical Casimir force of both the excess pressure and the excess chemical potential. As the chemical potential is intrinsically an isotropic quantity, the anisotropy of the Casimir effect is entirely contained in the excess pressure. A direct measure of the critical Casimir force however does necessarily pass through the computation of the excess chemical potential, which proved approximately an order of magnitude larger than the critical Casimir force. Computing the chemical potential proving rather difficult, we could in future works take advantage of the relation between excess chemical potential and excess internal energy $\mu_{ex} = A(n,T)u_{ex}$ that we identified.

We believe these preliminary results form a strong basis for future investigations and we are confident that the tendencies outlined in the present chapter, such as the direct measurement of the critical Casimir force (Fig.7.10), will be confirmed in the continuation of this work. Lennard-Jones simulations of binary mixtures open the way to a great variety of studies, closely related to experimental approaches, such as measurements of the fluctuations of the critical Casimir force [20, 21], dynamic effects when performing temperature quenches and out-of-equilibrium effects. The introduction of fixed boundary conditions is of course a natural future step. This will require the disentanglement of the critical Casimir force from non critical confinement forces, just as in the case of experimental approaches where the critical Casimir force has to be separated from contributions such as van der Waals forces [5, 6, 64, 73].

Conclusions and Perspectives

In this work we have studied the effect of the confinement of critical fluctuations using numerical simulations and the theoretical framework of finite-size scaling (see chapters 1, 2 and 3). At the heart of this work is one consequence of this confinement which has attracted much attention in the past decades: the critical Casimir force (see chapter 4). A motivation of this work was the observation that theoretical and numerical works have almost systematically been performed in magnetic model systems, while experimental approaches were all realized in fluid systems, such as binary mixtures or helium IV close to the superfluid transition. We have been interested in closing this gap by, firstly, proposing an experimental protocol for measuring the critical Casimir force in a magnetic layer (chapter 5) and, secondly, proposing a numerical approach in a Lennard-Jones binary mixture (chapter 7). We confined ourselves to the Ising universality class but the theoretical developments of this work can be easily extended to other universality classes, such as that of the XY model, which is of great experimental relevance.

We believe our magnetic protocol opens to the way to exploring the critical Casimir effect in magnetic systems, which would give access to a great variety of universality classes, including quantum phase transitions, a variety of geometries and boundary conditions, uniform or structured, and crossover phenomena, for example between 2D and 3D effects or between different universality classes. Such realizations require the fabrication of magnetic thin films of very well controlled thickness, sufficient resolution on the magnetization measurements to capture finite-size effects and materials with Curie temperature low enough so that finite-size effects can be completely suppressed by a magnetic field. The right material has still to be found but numerous systems show essentially perfect model magnetism and the fabrication of magnetic thin films is well advanced. This new perspective leads to further theoretical and experimental questions. Can we measure the critical Casimir force thanks to magneto-elastic coupling in a magnetic layer, or does magneto-elastic coupling systematically drives the transition first order [106] ? Can two objects close to a magnetic system at criticality feel a critical Casimir interactions mediated by the magnetic system [68] ?

Our results in Lennard-Jones binary mixtures have made contact with previous results, especially with finite-size scaling results obtained in the Ising model. The results we presented are still in part preliminary but already lead to quite new conclusions, such as the spectacular

cancellation of the critical finite-size effects in the excess confinement pressure $P_{ex,\perp}$ and the excess chemical potential multiplied by the density $n\mu_{ex}$. Their difference, the generalized pressure $P_{ex,\perp} - n\mu_{ex}$, amounts to the critical Casimir force, an order of magnitude smaller than the critical effects in $P_{ex,\perp}$ and $n\mu_{ex}$, and our results show a promising tendency in this direction. Quite surprisingly, the excess pressure undergoes a sign change above a threshold total density. We have been able to related this sign change to the reentrant miscibility observed in the phase diagram of our Lennard-Jones binary mixtures and the change in sign of the derivative of the critical temperature with respect to density. Some of our results are potentially of great experimental interest, such as the anisotropy of the excess pressure in slab geometry. Access to the critical Casimir effect in directions transverse to the confinement would give direct access to the scaling function of the excess free energy (see chapter 6). Due to lack of time, we have not yet studied the fluctuations of the critical Casimir force, or dynamic and out-of-equibrium effects, but molecular dynamics simulations give access to instantaneous values of the force and lend themselves to such approaches. We have also been restricted to the case of fully boundary conditions but the study of different boundary conditions is naturally accessible and of great experimental and theoretical interest. This leaves open some theoretical and numerical questions, as one would need to disentangle non-critical confinement forces from the critical Casimir forces in very small simulation boxes and perhaps develop a numerical approach allowing for the study of larger systems than in the present work, the numerical effort being quite demanding.

Bibliography

[1] Kurt Binder. Overcoming the Limitation of Finite Size in Simulations: From the Phase Transition of the Ising Model to Polymers, Spin Glasses, etc. In AIP Conference Proceedings, volume 690, pages 74–84. AIP Publishing, November 2003.

[2] M. E. J. Newman and G. T. Barkema. Monte Carlo Methods in Statistical Physics. OXFORD University Press.

[3] O. Vasilyev, A. Gambassi, A. Maciołek, and S. Dietrich. Universal scaling functions of critical Casimir forces obtained by Monte Carlo simulations. Physical Review E, 79(4):041142, April 2009.

[4] Andrea Pelissetto and Ettore Vicari. Critical phenomena and renormalization-group theory. Physics Reports, 368(6):549–727, October 2002.

[5] Masafumi Fukuto, Yohko F. Yano, and Peter S. Pershan. Critical Casimir Effect in Three-Dimensional Ising Systems: Measurements on Binary Wetting Films. Phys. Rev. Lett., 94(13):135702, April 2005.

[6] R. Garcia and M. H. W. Chan. Critical Fluctuation-Induced Thinning of 4he Films near the Superfluid Transition. Phys. Rev. Lett., 83(6):1187–1190, August 1999.

[7] Sarabjit Mehta, Mark O. Kimball, and Francis M. Gasparini. Superfluid Transition of ^{4}He for Two-Dimensional Crossover, Heat Capacity, and Finite-Size Scaling. Journal of Low Temperature Physics, 114(5-6):467–521, March 1999.

[8] M. O. Kimball, S. Mehta, and F. M. Gasparini. Specific Heat Near the Superfluid Transition of a 0.9869 μm 4he Film. Journal of Low Temperature Physics, 121(1-2):29–51, October 2000.

[9] Martin Hasenbusch. Specific heat, internal energy, and thermodynamic Casimir force in the neighborhood of the λ transition. Phys. Rev. B, 81(16):165412, April 2010.

[10] Jun Wang, Wei Wu, Fan Zhao, and Guo-meng Zhao. Finite-size scaling behavior and intrinsic critical exponents of nickel: Comparison with the three-dimensional Heisenberg model. Phys. Rev. B, 84(17):174440, November 2011.

[11] Yi Li and K. Baberschke. Dimensional crossover in ultrathin Ni(111) films on W(110). Phys. Rev. Lett., 68(8):1208–1211, February 1992.

[12] F. Huang, M. T. Kief, G. J. Mankey, and R. F. Willis. Magnetism in the few-monolayers limit: A surface magneto-optic Kerr-effect study of the magnetic behavior of ultrathin films of Co, Ni, and Co-Ni alloys on Cu(100) and Cu(111). Phys. Rev. B, 49(6):3962–3971, February 1994.

[13] Andrea Gambassi. The Casimir effect: From quantum to critical fluctuations. Journal of Physics: Conference Series, 161:012037, April 2009.

[14] Casimir, H.B.G. On the attraction between two perfectly conducting plates. Royal Netherlands Academy of Arts and Sciences, 51(7):793–795, 1948.

[15] P.-G. de Gennes M. E. Fisher. Phénomènes aux parois dans un mélange binaire critique. C. R. Acad. Sc. Paris, Ser. B 287, 207, October 1978.

[16] David Lopes Cardozo, Hugo Jacquin, and Peter C. W. Holdsworth. Critical Casimir forces in a magnetic system: An experimental protocol. Phys. Rev. B, 90(18):184413, November 2014.

[17] H. Eugene Stanley. Scaling, universality, and renormalization: Three pillars of modern critical phenomena. Rev. Mod. Phys., 71(2):S358–S366, March 1999.

[18] C. A. F. Vaz, J. A. C. Bland, and G. Lauhoff. Magnetism in ultrathin film structures. Rep. Prog. Phys., 71(5):056501, May 2008.

[19] L. J. De Jongh and A. R. Miedema. Experiments on simple magnetic model systems. Advances in Physics, 50(8):947–1170, 2001.

[20] Denis Bartolo. Fluctuations of Fluctuation-Induced Casimir-Like Forces. Phys. Rev. Lett., 89(23), 2002.

[21] Daniel Dantchev and Michael Krech. Critical Casimir force and its fluctuations in lattice spin models: Exact and Monte Carlo results. Phys. Rev. E, 69(4):046119, April 2004.

[22] PSMN: Pôle scientifique de modélisation numérique. http://www.ens-lyon.fr/PSMN/doku.php.

[23] Nigel Goldenfeld. Lectures on phase transitions and the renormalization group. Addison-Wesley, Advanced Book Program, Reading, Mass., 1992.

[24] P. M. Chaikin and T. C. Lubensky. Principles of Condensed Matter Physics. Cambridge University Press, September 2000.

[25] E. A. Guggenheim. The Principle of Corresponding States. The Journal of Chemical Physics, 13(7):253–261, July 1945.

[26] Michael Krech. The Casimir effect in critical systems. World Scientific, 1994.

[27] W. P. Wolf. The Ising model and real magnetic materials. Brazilian Journal of Physics, 30(4):794–810, December 2000.

[28] Hironobu Ikeda and Kinshiro Hirakawa. Neutron scattering study of two-dimensional Ising nature of K_2CoF_4. Solid State Communications, 14(7):529–532, April 1974.

[29] Lars Onsager. Crystal Statistics. I. A Two-Dimensional Model with an Order-Disorder Transition. Phys. Rev., 65(3-4):117–149, February 1944.

[30] David P. Landau and Kurt Binder. A Guide to Monte Carlo Simulations in Statistical Physics. Cambridge University Press, 2000.

[31] M. E. Fisher. The theory of equilibrium critical phenomena. Rep. Prog. Phys., 30(2):615, July 1967.

[32] H. Eugene Stanley. Introduction to Phase Transitions and Critical Phenomena. Oxford University Press, New York, July 1987.

[33] Cheng-Cher Huang and John T. Ho. Faraday rotation near the Curie point of EuO. Phys. Rev. B, 12(11):5255–5260, December 1975.

[34] Valdimir Privman and Michael E. Fisher. Universal critical amplitudes in finite-size scaling. Phys. Rev. B, 30(1):322–327, July 1984.

[35] Massimo Campostrini, Martin Hasenbusch, Andrea Pelissetto, Paolo Rossi, and Ettore Vicari. Critical behavior of the three-dimensional XY universality class. Phys. Rev. B, 63(21):214503, May 2001.

[36] C. Ruge, P. Zhu, and F. Wagner. Correlation function in Ising models. Physica A: Statistical Mechanics and its Applications, 209(3–4):431–443, September 1994.

[37] A. P. Gottlob and M. Hasenbusch. Critical Behaviour of the 3d XY-Model: A Monte Carlo Study. Physica A: Statistical Mechanics and its Applications, 201(4):593–613, December 1993. arXiv: cond-mat/9305020.

[38] H. R. Ott, G. Keller, W. Odoni, L. D. Woolf, M. B. Maple, D. C. Johnston, and H. A. Mook. $HoRh_4B_4$: A model mean-field ferromagnet. Phys. Rev. B, 25:477–480, Jan 1982.

[39] Nicholas Metropolis, Arianna W. Rosenbluth, Marshall N. Rosenbluth, Augusta H. Teller, and Edward Teller. Equation of State Calculations by Fast Computing Machines. The Journal of Chemical Physics, 21(6):1087–1092, June 1953.

[40] Ulli Wolff. Collective Monte Carlo Updating for Spin Systems. Phys. Rev. Lett., 62(4):361–364, January 1989.

[41] P.G. Lauwers and V. Rittenberg. The critical 2d Ising model in a magnetic field. A Monte Carlo study using a Swendesen-Wang algorithm. Physics Letters B, 233(1–2):197–200, December 1989.

[42] Jian-Sheng Wang. Clusters in the three-dimensional Ising model with a magnetic field. Physica A: Statistical Mechanics and its Applications, 161(2):249–268, November 1989.

[43] C. Destri, F. Di Renzo, E. Onofri, P. Rossi, and G.P. Tecchiolli. Swendsen-Wang Monte Carlo study of the Ising model with external field. Physics Letters B, 278(3):311–316, March 1992.

[44] K. Binder. Finite size effects at phase transitions. In H. Gausterer and C. B. Lang, editors, Computational Methods in Field Theory, number 409 in Lecture Notes in Physics, pages 59–125. Springer Berlin Heidelberg, 1992.

[45] M. Hasenbusch and K. Pinn. A_+/A_-,α,ν, and $f_s\xi^3$ from 3d Ising energy and specific heat. J. Phys. A: Math. Gen., 31(29):6157, July 1998.

[46] Martin Hasenbusch. Finite size scaling study of lattice models in the three-dimensional Ising universality class. Phys. Rev. B, 82(17):174433, November 2010.

[47] A. Gambassi, A. Maciołek, C. Hertlein, U. Nellen, L. Helden, C. Bechinger, and S. Dietrich. Critical Casimir effect in classical binary liquid mixtures. Phys. Rev. E, 80(6):061143, December 2009.

[48] Daniel J. Amit and Victor Martin-mayor. Field Theory; The Renormalization Group and Critical Phenomena. World Scientific Publishing Company, Singapore; New Jersey, 3 edition edition, June 2005.

[49] Maxime Clusel. Quelques aspects de physique statistique des systèmes corrélés. PhD thesis, Ecole normale supérieure de lyon - ENS LYON, July 2005.

[50] K. Binder. Finite size scaling analysis of ising model block distribution functions. Z. Physik B - Condensed Matter, 43(2):119–140, June 1981.

[51] E. Eisenriegler and R. Tomaschitz. Helmholtz free energy of finite spin systems near criticality. Phys. Rev. B, 35(10):4876–4887, April 1987.

[52] Baptiste Portelli. Fluctuations des grandeurs globales dans les systèmes corrélés. Ecole Normale Supérieure de Lyon, January 2002.

[53] B. Portelli, P. C. W. Holdsworth, M. Sellitto, and S. T. Bramwell. Universal magnetic fluctuations with a field-induced length scale. Phys. Rev. E, 64(3):036111, August 2001.

[54] Kazuhisa Kaneda, Yutaka Okabe, and Macoto Kikuchi. Shape Effects of Finite-Size Scaling Functions for Anisotropic Three-Dimensional Ising Models. Journal of Physics A: Mathematical and General, 32(42):7263–7271, October 1999. arXiv: cond-mat/9909262.

[55] Kurt Binder and Jian-Sheng Wang. Finite-size effects at critical points with anisotropic correlations: Phenomenological scaling theory and Monte Carlo simulations. J Stat Phys, 55(1-2):87–126, April 1989.

[56] M. E. J. Newman and G. T. Barkema. Monte Carlo study of the random-field Ising model. Phys. Rev. E, 53(1):393–404, January 1996.

[57] Martin Hasenbusch. Thermodynamic Casimir effect for films in the three-dimensional Ising universality class: Symmetry-breaking boundary conditions. Phys. Rev. B, 82(10):104425, September 2010.

[58] Martin Hasenbusch. Thermodynamic Casimir force: A Monte Carlo study of the crossover between the ordinary and the normal surface universality class. Phys. Rev. B, 83(13):134425, April 2011.

[59] Martin Hasenbusch. Thermodynamic Casimir effect in films: The exchange cluster algorithm. Phys. Rev. E, 91(2):022110, February 2015.

[60] M. M. Tsypin and H. W. J. Blöte. Probability distribution of the order parameter for the three-dimensional Ising-model universality class: A high-precision Monte Carlo study. Phys. Rev. E, 62(1):73–76, July 2000.

[61] Kurt Binder, David Landau, and Marcus Müller. Monte Carlo Studies of Wetting, Interface Localization and Capillary Condensation. Journal of Statistical Physics, 110(3-6):1411–1514, March 2003.

[62] Nigel B. Wilding and Michael Krech. Effect of criticality on wetting layers: A Monte Carlo simulation study. Phys. Rev. E, 57(5):5795–5801, May 1998.

[63] Caroline Crauste, Clemence Devailly, Audrey Steinberger, and Sergio Ciliberto. Characterization of PMMA–3-octanone binary by turbidity and light scattering measurements. arXiv:1310.6720 [cond-mat], October 2013. arXiv: 1310.6720.

[64] A. Ganshin, S. Scheidemantel, R. Garcia, and M. H. W. Chan. Critical Casimir Force in He4 Films: Confirmation of Finite-Size Scaling. Phys. Rev. Lett., 97(7):075301, August 2006.

[65] Van Duc Nguyen, Suzanne Faber, Zhibing Hu, Gerard H. Wegdam, and Peter Schall. Controlling colloidal phase transitions with critical Casimir forces. Nat Commun, 4:1584, March 2013.

[66] John R. Edison, Nikos Tasios, Simone Belli, Robert Evans, René van Roij, and Marjolein Dijkstra. Critical Casimir Forces and Colloidal Phase Transitions in a Near-Critical Solvent: A Simple Model Reveals a Rich Phase Diagram. Phys. Rev. Lett., 114(3):038301, January 2015.

[67] C. Hertlein, L. Helden, A. Gambassi, S. Dietrich, and C. Bechinger. Direct measurement of critical Casimir forces. Nature, 451(7175):172–175, January 2008.

[68] O. A. Vasilyev. Critical Casimir interactions between spherical particles in the presence of bulk ordering fields. Phys. Rev. E, 90(1):012138, July 2014.

[69] Martin Hasenbusch. Thermodynamic Casimir forces between a sphere and a plate: Monte Carlo simulation of a spin model. Phys. Rev. E, 87(2):022130, February 2013.

[70] Theodore W. Burkhardt and Erich Eisenriegler. Casimir Interaction of Spheres in a Fluid at the Critical Point. Phys. Rev. Lett., 74(16):3189–3192, April 1995.

[71] M. Krech. Fluctuation-induced forces in critical fluids. J. Phys.: Condens. Matter, 11(37):R391, September 1999.

[72] Jean-Louis Barrat and Jean-Pierre Hansen. Basic Concepts for Simple and Complex Liquids. Cambridge University Press, March 2003.

[73] R. Garcia and M. H. W. Chan. Critical Casimir Effect near the ^{3}He-^{4}He Tricritical Point. Phys. Rev. Lett., 88(8):086101, February 2002.

[74] Salima Rafaï, Daniel Bonn, and Jacques Meunier. Repulsive and attractive critical Casimir forces. Physica A: Statistical Mechanics and its Applications, 386(1):31–35, December 2007.

[75] Francesco Parisen Toldin and S. Dietrich. Critical Casimir forces and adsorption profiles in the presence of a chemically structured substrate. J. Stat. Mech., 2010(11):P11003, November 2010.

[76] Alfred Hucht, Daniel Grüneberg, and Felix M. Schmidt. Aspect-ratio dependence of thermodynamic Casimir forces. Phys. Rev. E, 83(5):051101, May 2011.

[77] Michael Krech. Casimir forces in binary liquid mixtures. Phys. Rev. E, 56(2):1642–1659, August 1997.

[78] O. A. Vasilyev and S. Dietrich. Critical Casimir forces for films with bulk ordering fields. EPL, 104(6):60002, December 2013.

[79] H. W. Diehl. The Theory of Boundary Critical Phenomena. Int. J. Mod. Phys. B, 11(30):3503–3523, December 1997.

[80] Francesco Parisen Toldin, Matthias Tröndle, and S. Dietrich. Critical Casimir forces between homogeneous and chemically striped surfaces. Phys. Rev. E, 88(5):052110, November 2013.

[81] M. Tröndle, L. Harnau, and S. Dietrich. Critical Casimir forces between planar and crenellated surfaces. arXiv:1408.6088 [cond-mat], August 2014. arXiv: 1408.6088.

[82] M. Tröndle, S. Kondrat, A. Gambassi, L. Harnau, and S. Dietrich. Critical Casimir effect for colloids close to chemically patterned substrates. The Journal of Chemical Physics, 133(7):074702, August 2010.

[83] M. Tröndle, S. Kondrat, A. Gambassi, L. Harnau, and S. Dietrich. Normal and lateral critical Casimir forces between colloids and patterned substrates. EPL, 88(4):40004, November 2009.

[84] M. Tröndle, L. Harnau, and S. Dietrich. Critical adsorption and critical Casimir forces for geometrically structured confinements. The Journal of Chemical Physics, 129(12):124716–124716–22, September 2008.

[85] Matthias Tröndle, Olga Zvyagolskaya, Andrea Gambassi, Dominik Vogt, Ludger Harnau, Clemens Bechinger, and Siegfried Dietrich. Trapping colloids near chemical stripes via critical Casimir forces. Molecular Physics, 109(7-10):1169–1185, 2011.

[86] Giuseppe Bimonte, Thorsten Emig, and Mehran Kardar. Reversing the critical Casimir force by shape deformation. Physics Letters B, 743:138–142, April 2015.

[87] O. Vasilyev, A. Maciołek, and S. Dietrich. Critical Casimir forces for Ising films with variable boundary fields. Phys. Rev. E, 84(4):041605, October 2011.

[88] Douglas B. Abraham and Anna Maciołek. Casimir Interactions in Ising Strips with Boundary Fields: Exact Results. Phys. Rev. Lett., 105(5):055701, July 2010.

[89] T. F. Mohry, A. Maciołek, and S. Dietrich. Crossover of critical Casimir forces between different surface universality classes. Phys. Rev. E, 81(6):061117, June 2010.

[90] Francesco Parisen Toldin, Matthias Tröndle, and S. Dietrich. Line contribution to the critical Casimir force between a homogeneous and a chemically stepped surface. arXiv:1409.5536 [cond-mat], September 2014. arXiv: 1409.5536.

[91] Andrea Gambassi and S. Dietrich. Critical Casimir forces steered by patterned substrates. Soft Matter, 7(4):1247, 2011. arXiv: 1011.1831.

[92] Monika Sprenger, Frank Schlesener, and S. Dietrich. Forces between chemically structured substrates mediated by critical fluids. The Journal of Chemical Physics, 124(13):134703–134703–19, April 2006.

[93] Florian Soyka, Olga Zvyagolskaya, Christopher Hertlein, Laurent Helden, and Clemens Bechinger. Critical Casimir Forces in Colloidal Suspensions on Chemically Patterned Surfaces. Phys. Rev. Lett., 101(20):208301, November 2008.

[94] Matthias Tröndle, Olga Zvyagolskaya, Andrea Gambassi, Dominik Vogt, Ludger Harnau, Clemens Bechinger, and Siegfried Dietrich. Trapping colloids near chemical stripes via critical Casimir forces. Molecular Physics, 109(7-10):1169–1185, March 2011.

[95] Francesco Parisen Toldin. Critical Casimir force in the presence of random local adsorption preference. Phys. Rev. E, 91(3):032105, March 2015.

[96] A. Maciołek, O. Vasilyev, V. Dotsenko, and S. Dietrich. Critical Casimir forces in the presence of random surface fields. arXiv:1502.02575 [cond-mat], February 2015. arXiv: 1502.02575.

[97] Z. Borjan and P. J. Upton. Off-Critical Casimir Effect in Ising Slabs with Symmetric Boundary Conditions in d=3. Phys. Rev. Lett., 101(12):125702, September 2008.

[98] K. K. Mon. Monte Carlo studies of critical free energies and the simple-cubic Ising model. Phys. Rev. B, 39(1):467–470, January 1989.

[99] K. K. Mon and K. Binder. Monte Carlo calculation of free energy for a fcc lattice-gas model. Phys. Rev. B, 42(1):675–679, July 1990.

[100] M. Krech and D. P. Landau. Casimir effect in critical systems: A Monte Carlo simulation. Phys. Rev. E, 53(5):4414–4423, May 1996.

[101] O. Vasilyev, A. Gambassi, A. Maciołek, and S. Dietrich. Monte Carlo simulation results for critical Casimir forces. Europhysics Letters (EPL), 80(6):60009, December 2007.

[102] Martin Hasenbusch. Thermodynamic Casimir Forces between a Sphere and a Plate: Monte Carlo Simulation of a Spin Model. arXiv:1210.3961, October 2012. Phys. Rev. E 87, 022130 (2013).

[103] Alfred Hucht. Thermodynamic Casimir Effect in ^{4}He Films near T_λ: Monte Carlo Results. Phys. Rev. Lett., 99(18):185301, November 2007.

[104] R. Evans and J. Stecki. Solvation force in two-dimensional Ising strips. Phys. Rev. B, 49(13):8842–8851, April 1994.

[105] Martin Hasenbusch. The thermodynamic Casimir effect in the neighbourhood of the λ-transition: a Monte Carlo study of an improved three-dimensional lattice model. Journal of Statistical Mechanics: Theory and Experiment, 2009(07):P07031, July 2009.

[106] D. J. Bergman and B. I. Halperin. Critical behavior of an Ising model on a cubic compressible lattice. Physical Review B, 13(5):2145–2175, March 1976.

[107] Martin Hasenbusch. Thermodynamic Casimir effect: Universality and corrections to scaling. Phys. Rev. B, 85(17):174421, May 2012.

[108] H. M. Ronnow, D. F. McMorrow, and A. Harrison. High-temperature magnetic correlations in the 2d $s = 1/2$ antiferromagnet copper formate tetradeuterate. Phys. Rev. Lett., 82:3152–3155, Apr 1999.

[109] J Als-Nielsen, S T Bramwell, M T Hutchings, G J McIntyre, and D Visser. Neutron scattering investigation of the static critical properties of Rb_2 $CrCl_4$. Journal of Physics: Condensed Matter, 5(42):7871, 1993.

[110] Vassilios Kapaklis, Unnar B Arnalds, Adam Harman-Clarke, Evangelos Th Papaioannou, Masoud Karimipour, Panagiotis Korelis, Andrea Taroni, Peter C W Holdsworth, Steven T Bramwell, and Björgvin Hjörvarsson. Melting artificial spin ice. New Journal of Physics, 14(3):035009, 2012.

[111] Vassilios Kapaklis, Unnar B. Arnalds, Alan Farhan, Rajesh V. Chopdekar, Ana Balan, Andreas Scholl, Laura J. Heyderman, and Björgvin Hjörvarsson. Thermal fluctuations in artificial spin ice. Nat Nano, 9(7):514–519, July 2014.

[112] Evangelos Th Papaioannou, Vassilios Kapaklis, Andrea Taroni, Moreno Marcellini, and Björgvin Hjörvarsson. Dimensionality and confinement effects in δ-doped Pd(Fe) layers. J. Phys.: Condens. Matter, 22(23):236004, June 2010.

[113] E. F. Shender and P. C. W. Holdsworth. Spin Structure in Magnetic Multilayers with Rough Interfaces. Phys. Rev. Lett., 76(14):2583–2586, April 1996.

[114] D. Bitko, T. F. Rosenbaum, and G. Aeppli. Quantum critical behavior for a model magnet. Phys. Rev. Lett., 77:940–943, Jul 1996.

[115] S. Sachdev. Quantum Phase Transitions. CUP, 2011.

[116] M. Mena, R. S. Perry, T. G. Perring, M. D. Le, S. Guerrero, M. Storni, D.T. Adroja, Ch. Rüegg, and D.F. McMorrow. Spin-Wave Spectrum of the Quantum Ferromagnet on the Pyrochlore Lattice $Lu_2V_2O_7$. Phys. Rev. Lett., 113(4):047202, July 2014.

[117] Y. Onose, T. Ideue, H. Katsura, Y. Shiomi, N. Nagaosa, and Y. Tokura. Observation of the Magnon Hall Effect. Science, 329(5989):297–299, July 2010.

[118] V. Dohm. Critical Casimir force in slab geometry with finite aspect ratio: Analytic calculation above and below Tc. EPL, 86(2):20001, April 2009.

[119] Volker Dohm. Critical free energy and Casimir forces in rectangular geometries. Phys. Rev. E, 84(2):021108, August 2011.

[120] Vladimir Privman and Michael E. Fisher. Finite-size effects at first-order transitions. J Stat Phys, 33(2):385–417, November 1983.

[121] H. W. Diehl, Daniel Grüneberg, Martin Hasenbusch, Alfred Hucht, Sergei B. Rutkevich, and Felix M. Schmidt. Large-n approach to thermodynamic Casimir effects in slabs with free surfaces. Phys. Rev. E, 89(6):062123, June 2014.

[122] Nigel B. Wilding. Critical end point behavior in a binary fluid mixture. Phys. Rev. E, 55(6):6624–6631, June 1997.

[123] Nigel B. Wilding. Continuous demixing at liquid-vapor coexistence in a symmetrical binary fluid mixture. Phys. Rev. E, 67(5):052503, May 2003.

[124] Subir K. Das, Jürgen Horbach, Kurt Binder, Michael E. Fisher, and Jan V. Sengers. Static and dynamic critical behavior of a symmetrical binary fluid: A computer simulation. The Journal of Chemical Physics, 125(2):024506, July 2006.

[125] S. Materniak, A. Patrykiejew, and S. Sokołowski. The phase behavior of two-dimensional symmetrical mixtures. The Journal of Chemical Physics, 133(24):244501, December 2010.

[126] Minerva González-Melchor, Pedro Orea, Jorge López-Lemus, Fernando Bresme, and José Alejandre. Stress anisotropy induced by periodic boundary conditions. The Journal of Chemical Physics, 122(9):094503, March 2005.

[127] Jiří Kolafa. Finite size effects for liquids in cyclic boundary conditions. Molecular Physics, 75(3):577–586, February 1992.

[128] LAMMPS Molecular Dynamics Simulator. http://lammps.sandia.gov.

[129] Daan Frenkel and Berend Smit. Understanding Molecular Simulation, Second Edition: From Algorithms to Applications. Academic Press, San Diego, 2 edition edition, November 2001.

[130] Enrique de Miguel and George Jackson. The nature of the calculation of the pressure in molecular simulations of continuous models from volume perturbations. The Journal of Chemical Physics, 125(16):164109, October 2006.

[131] B. Widom. Some Topics in the Theory of Fluids. The Journal of Chemical Physics, 39(11):2808–2812, December 1963.

[132] N. B. Wilding, F. Schmid, and P. Nielaba. Liquid-vapor phase behavior of a symmetrical binary fluid mixture. Phys. Rev. E, 58(2):2201–2212, August 1998.

[133] N. G. Almarza, E. Enciso, M. F. García, M. A. González, and F. J. Bermejo. Reentrant miscibility in fluids with spherical interactions. Phys. Rev. E, 64(1):012501, June 2001.

[134] S. Materniak, A. Patrykiejew, and W. Rżysko. Reentrant miscibility in two-dimensional symmetrical mixtures. Phys. Rev. E, 87(6):062306, June 2013.

[135] Subir K. Das, Jürgen Horbach, and Kurt Binder. Transport phenomena and microscopic structure in partially miscible binary fluids: A simulation study of the symmetrical Lennard-Jones mixture. The Journal of Chemical Physics, 119(3):1547–1558, July 2003.